Summer 2005

Modeling and Simulation of \Sub-Microsecond Electrical Breakdown in Liquids with Application to Water

Jun Qian
Old Dominion University

MODELING AND SIMULATION OF SUB-MICROSECOND ELECTRICAL BREAKDOWN IN LIQUIDS WITH APPLICATION TO WATER

by

Jun Qian
B. S. July 1997, Northeastern University, China
M. S. July 2000, University of Science & Technology of China, China

A Dissertation Submitted to the Faculty of
Old Dominion University in Partial Fulfillment of the
Requirement for the Degree of

DOCTOR OF PHILOSOPHY

ELECTRICAL ENGINEERING

OLD DOMINION UNIVERSITY
August 2005

Approved by:

Ravindra P. Joshi (Director)

Karl H. Schoenbach (Member)

Linda L. Vahala (Member)

Duc T. Nguyen (Member)

ABSTRACT

MODELING AND SIMULATION OF SUB-MICROSECOND ELECTRICAL BREAKDOWN IN LIQUIDS WITH APPLICATION TO WATER

Jun Qian
Old Dominion University, 2005
Director: Dr. Ravindra P. Joshi

Pulsed power technology is well suited for driving electrical loads at very large currents (kilo-Ampere range) in short (sub-microsecond range) bursts. Many of the applications require that these technological devices be deployed in very small spaces and operate under stressful and harsh environments. The use of switches, capacitive storage devices, and compact, portable pulse generation systems based on liquid water appear to have inherent advantages for pulsed power technology. However, at the present time, the fundamental physics of such liquid dielectrics, their breakdown behavior, inherent physical mechanisms and high electric field response are not well understood. In this dissertation, the inherent physics and sub-microsecond electrical breakdown of water stressed to high voltages is analyzed, and several relevant models are constructed for quantitative analysis. A bubble-based, drift-diffusion (DD) model proposed here includes almost all the important physical process of the system, and successfully explains many important features routinely observed in sub-microsecond water electrical breakdown.

Here many physical properties and response characteristics typical for high-field stressing of liquid water have been analyzed through numerical calculations. The internal temperature profile in the water system has been calculated by Finite Difference Time Domain (FDTD) method to probe possible heating and vaporization effects. Results show temperature increases of less than 7° Kelvin, precluding possibilities for localized

evaporation. Second, it is shown through Monte-Carlo simulations that electrons in liquid water cannot contribute to impact ionization and electron multiplication at normal liquid water densities. Instead, it is shown that electrons emitted within pre-existing micro-bubbles within the liquid could contribute to electron multiplication and initiate the electric breakdown process. Third, it is demonstrated here through microscopic Monte-Carlo calculations that the dielectric constant of water would be a monotonically decreasing function of the electrical field, with strong reductions beyond 3 MV/cm. It is also shown that this field-dependent behavior, coupled with electric field enhancements across dielectric discontinuities such as the water-bubble interface, can potentially contribute to electrical breakdown.

Two percolative models are also presented and discussed here to probe the random, stochastic and fractal nature of breakdown and streamer generation. The time-dependent results show tree-like shapes for streamers and yield streamer propagation velocities and circuit current in keeping with measured data.

Finally, the most important contribution of this dissertation is the development of a bubble-based, drift-diffusion (DD) model that includes the field-dependent effects. Simulation results based on this model show strong agreement with many features of experimentally observed features. The features include: (i) streamer branching for the positive polarity due to internal micro-bubbles; (ii) negative streamers normally having a higher breakdown voltage requirement; (iii) negative streamers having a thicker root and larger cross-sectional radii as compared to positive streamers; (iv) increasing hold-on voltage with system over-pressure; and (v) faster breakdown times for positive polarity, point-plane geometries. The model is quite general, and applicable to other liquids.

ACKNOWLEDGMENTS

I would like to thank my advisor, Dr. R. P. Joshi, for his valuable academic guidance, encouragement, and patience throughout the about five-year study. I could not have completed this project without his abundant help in every aspect. He set a great model for me in my future work. I would also like to thank Dr. Karl H. Schoenbach, Dr. Linda L. Vahala, and Dr. Duc T. Nguyen for their kind help as my dissertation committee members and their precious time.

Tons of thanks to the researchers within water-discharge group at the Center for Bioelectronics for their great experimental work and inspiring discussions, which were crucial to my dissertation. I also owe thanks to the Electrical and Computer Engineering department, for their support all these years. I really enjoyed the time studying at this department.

Great thanks to the great guys in our simulation group, Dr. Qin Hu, Guogang Zhao and to all the others for their help in all kinds of ways. Also, many thanks to the my friends, Fangsheng Meng, Feng Wu, Bing Xiao, Dr. Shangping Guo and many others, who make my life here more colorful.

Special appreciation goes to my mother. I can feel her warmth from heaven anytime, anywhere. Great appreciation to my father, who contributes all he can to our family and me.

TABLE OF CONTENTS

LIST OF FIGURES

Figure Page

LIST OF TABLES

CHAPTER I

INTRODUCTION

1.1 Overview

There is considerable interest [1-8] in the study of electrical breakdown in water (and other liquids) for pulsed power systems, for their use in ultra-short time power pulse generation, for energy storage systems, towards insulation of high-voltage devices, in acoustic devices, and as the medium in spark erosion machines. Liquids seem to have advantages over gases and solids for both energy storage and as switch media, particularly for nanosecond pulse generators. For example, liquids not only have a high dielectric constant, but also have higher breakdown strength than compressed gases [7]. Water has been used and found to hold off electrical fields of about 2 MV/cm for durations up to hundreds of ns [9, 10]. In comparison to solids, their ability to circulate leads to better thermal management and easier removal of debris after breakdown. Liquid dielectrics are also better suited for applications involving complex geometries. Also, they can "self-heal" following a breakdown event, or can be flushed for continued usage.

The electrical behavior of dielectric liquids (especially water) subjected to high electric fields has been intensively studied for many decades [11-20]. Despite the progress, there is as yet no final and complete understanding of issues relating to the initiation process, the physics of charge creation in liquids, and the subsequent plasma dynamics (e.g., the observed fast-moving streamers) on the sub-microsecond time scales.

The format followed: Physical Review E.

Part of the problem is that liquids lack the long-range order and periodicity that is inherent in solids. This makes it difficult to obtain exact repeatable results since the electrical behavior is inherently stochastic in nature. Examples include random treeing patterns [21-25], and surface discharges with Lichtenberg figures [21, 25]. Another complication is that conduction is strongly influenced by both the liquid-electrode interface and bulk properties that include a variety of electric-field and temperature-dependent processes [26-28]. Although experimental measurement techniques have substantially been improved, they still cannot meet the very high spatial and temporal resolution requirements necessary for completely unraveling the details of sub-microsecond water electrical breakdown phenomena. So, it is necessary to perform numerical modeling and theoretical simulations. The modeling can also help quantify the roles of various inherent processes, and gauge the relative importance of several on-going mechanisms.

1.2 Water Electrical Breakdown Experiments

A typical sub-microsecond water electrical breakdown experimental configuration [29] is shown in the figure 1-1. The experimental setup shown was assembled at the ODU Center for Bioelectrics. It is a point-plane electrode configuration, with sharp cathode radius (r = 0.85mm), and a variable water gap (ranging from 200μm to 400μm) between the two electrodes.

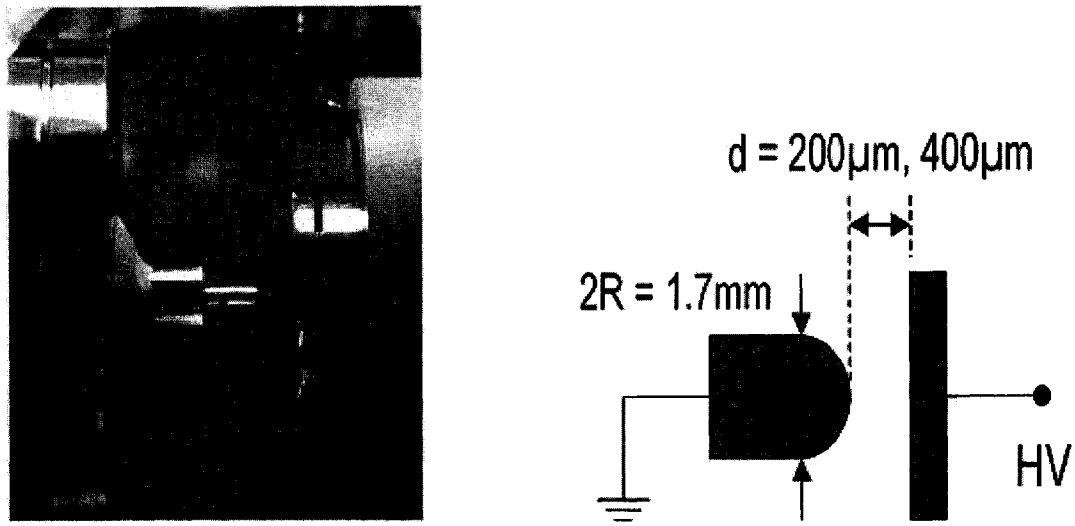

(a) (b)

Figure 1-1. Experimental setup picture and configuration of water electrical breakdown [29]. (a) The point-plane electrode, and (b) the configuration schematic.

The experimental results obtained [29] are shown in the figure 1-2. The voltage and current waveforms are given initially, followed by snapshots of the streamer dynamics. The figure shows streamer initiation at time t = 120ns, and that it reaches the other electrode at a time t = 230ns. This is a typical sequence in the sub-microsecond water electrical breakdown process. An initial streamer initiation is followed by propagation and a reach-over to the opposite electrode.

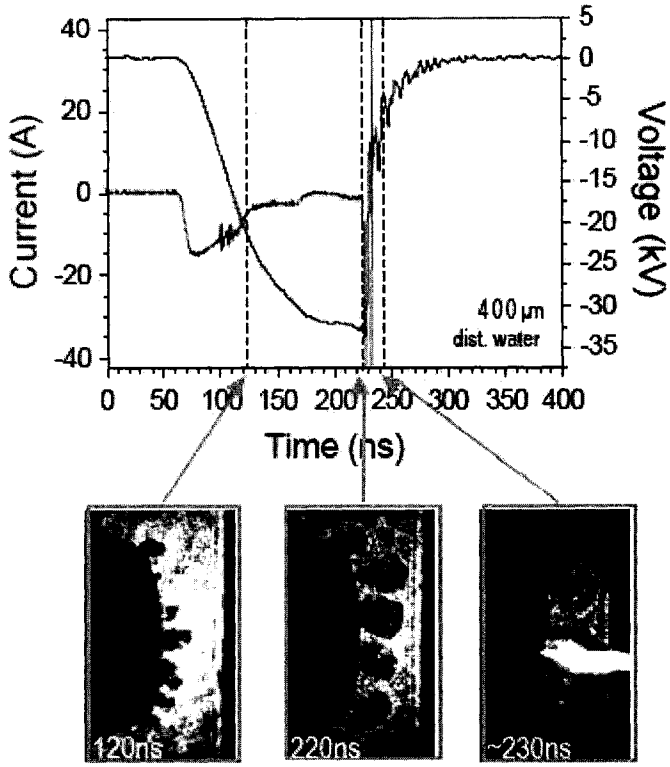

Figure 1-2. Experimental result for the configuration of Figure 1-1. Time-dependent waveforms for the voltage and current in the water are shown. Also, shown below are snapshots of the streamer dynamical processes [29].

1.3 Scope of the Present Dissertation Research

This work mainly focuses on the modeling and simulation of sub-microsecond water electrical breakdown process. The typical experimental set-up and measured data have been shown in figure 1-1 and figure 1-2. Through theoretical analysis and numerical simulation tools, the objective is to get a good understanding of the sub-microsecond electrical breakdown process in water (and polar liquids, in general). The subsequent and broader goal is to provide performance predictions and suggestions for the design and system enhancement for a given application.

In this dissertation, chapter 2 provides the relevant literature review, lists the major mechanisms proposed, and introduces models of liquid electrical breakdown. In

chapter 3, the detailed physics and aspects of potential model for sub-microsecond, electrical breakdown in water are presented. Discussions include the liquid-electrode interface, temperature effect, electronic behavior in low-density areas inside the liquid, and field-dependent liquid dielectric response. On the basis of these physical mechanisms, several numerical models are brought out and discussed. Next, chapter 4 shows the results obtained based on the models of chapter 3. The results are discussed, and include detail of the streamer random patterns, a possible mechanism for sub-microsecond water electrical breakdown, and polarity preferences. A summary and conclusion of the present research is given in chapter 5. This last chapter also includes suggestions for possible future work.

CHAPTER II

LITERATURE REVIEW AND BACKGROUND

2.1 Characteristics of Liquid Dielectric Electrical Breakdown

Electrical breakdown in water (or liquids in general) consists of two consecutive processes. (A) First, there is the initialization of an ionized streamer. Normally, the streamer initialization in point-plane electrode configurations is from the sharp "point electrode". The stronger curvature at this side increases the local electric field strengths. (B) Next, there is streamer propagation until it reaches the opposite electrode, after which electrical breakdown takes place.

A number of characteristic features have been observed during the overall liquid dielectric electrical breakdown process. These features appear to be quite general and common to all liquids, and include the following aspects:

1. A definite relationship between the applied pulse duration and the externally applied voltage [30-32]. For example, the field strength for breakdown in liquids increases as the duration of voltage application decreases to shorter time.

2. External pressure appears to affect the breakdown voltage. Increasing the over-pressure typically tends to enhance the breakdown voltage, while under-pressures have been observed to decrease the breakdown voltage.

3. A distinct polarity effect has been seen for point-plane (or similarly asymmetric) geometries [1, 10, 33, 34]. The breakdown voltage (= V_{br}) is universally observed to be *lower when the point electrode is biased positively, all other aspects being equal.* Based on gas discharge physics, one might expect liquid water breakdown to be initiated at the

cathode due to possible electronic injection. The experimental data, however, suggests otherwise, and indicates that mechanisms other than pure cathodic electron injection must be relevant to breakdown.

4. Streamer formation and dynamics, during the breakdown process, have been seen to have different geometric shapes and velocities depending on the polarity of the sharp ("pin") electrode. The streamers originating on the positive electrode form earlier in time, travel faster, and do not tend to exhibit velocity saturation with the electric field magnitude [35]. Also, for example, streamers formed from the anode tip typically have more branches. Cathode-tip streamers, on the other hand, usually have a prominently thicker "root". This, again, underscores the polarity dependent asymmetry.

5. Discrete optical luminosity spots have been seen on streamer branches [34, 36].

6. Pre-breakdown electrical current spikes of a random nature are usually observed during the pre-breakdown phase of liquid breakdown. Both polar solvents (such as water) and non-polar liquids (such as oils) have reportedly exhibited such behavior [34]. In figure 2-1, the pre-breakdown current spikes are shown in measured current curve. The times at which these current spikes have been observed to correlate well with the formation of the luminosity spots.

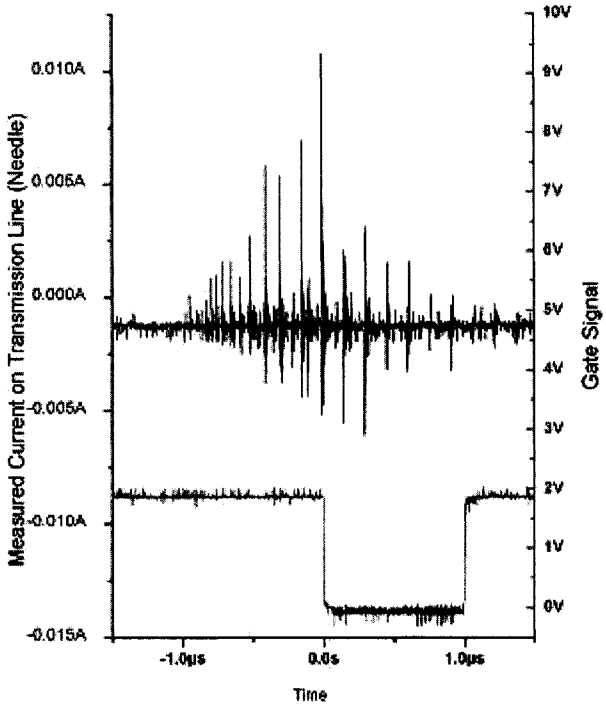

Figure 2-1.Time-dependent circuit current data in oil subject to a voltage pulse.

7. Polishing the electrodes (especially the anode) appears to help enhance the hold-off voltage. Management of asperities and the associated local electric field enhancements, therefore, appears to be very important [10]. In figure 2-2, it is shown that hold-on voltage for polished electrode can be much higher than that for an unpolished electrode.

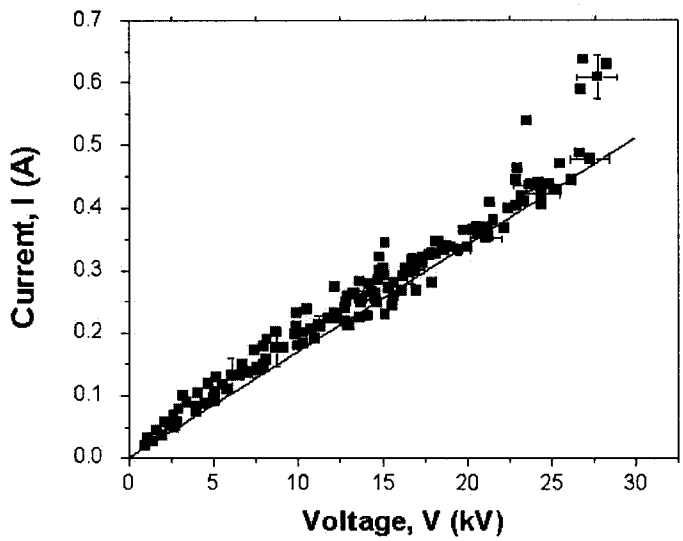

Figure 2-2. Measured current-voltage data points for water for a 200 μm point-plane geometry showing differences between unpolished (red) and polished (black) electrode surfaces (From private communication).

2.2 Mechanisms of Water Electrical Breakdown

Unlike the gas and solid electrical breakdown, there is no consensus at the present time regarding the mechanisms for pulsed breakdown in liquids (including water). Two major competing theories of liquid breakdown in water have emerged: (A) an electronic process through electron impact-ionization inside the liquid, and (B) a bubble initiated mechanism that leads to a propagated breakdown process.

2.2.1 Electron Process Based Mechanism of Water Electrical Breakdown

Electron impact ionization inside the liquid has been considered by some as one of the fundamental processes, which causes the liquid electrical breakdown and sudden increase of the current [37, 38]. The electron process based mechanism is similar to the discharge physics in gases. However, the fundamental issue regarding the electronic

mechanism is whether or not electron impact ionization can occur in liquid water at breakdown fields. Since the density in liquids is orders of magnitude higher than in gases, the internal scattering and collisional rates are correspondingly higher in liquids. It is therefore, not clear whether electrons in liquids can acquire the requisite energy from the external field, despite the increased collisions, for internal impact ionization.

2.2.2. Bubble Based Mechanism of Water Electrical Breakdown

It is postulated by many that liquid electrical breakdown proceeds through the creation and propagation of streamers over regions of low density [39, 40, 15, 41]. The low-density region is either pre-existing, or formed by localized heating near sharp electrodes where the electrical field is higher than the bulk area. The propagation of streamers during water breakdown is explained on the basis of continuous liquid water evaporation at the tip of the streamer due to substantial local heating [42]. There are a lot experimental data supporting the bubble mechanism: (A) The breakdown strength of liquids increases with increasing pressure [15]. This suggests that as the pressure is increased, the radii of internal bubbles shrink. It then becomes harder to maintain or grow the bubbles at the same external voltage. (B) Bubbles have physically been observed at sharp tips on electrodes [43, 44]. (C) The breakdown strength of liquids decrease with increasing temperature [42].

The fundamental issues and requirements relating to the bubble based mechanism are [15]: (A) the requisite existence of a low density region; (B) the low density region is big enough for impact ionization; (C) the power and energy density dumped into the streamer channel by the electrical circuit must be sufficient to heat the liquid at the

advancing end of the moving filamentary streamer. This would lead to a lowering of the liquid density and extend the streamer.

In summary, despite a large body of experimental observations, there is still no comprehensive understanding or agreement with regards to the inherent breakdown physics and the initiation process. Part of the problem is that liquids lack the long-range order and periodicity that is inherent in solids. This makes the analysis more complicated and less uniform. Also, in contrast to gases, the molecular density is much higher in liquids. This significantly enhances collective clustering effects. Thus, water breakdown presents a complex and dynamical, many-body problem. Another complication is that conduction is strongly influenced by both the liquid-electrode interface and bulk properties that include a variety of electric-field and temperature-dependent processes. A complete breakdown mechanism should include the polarity effect on the breakdown strength, streamer formation, streamer pattern, voltage strength, and streamer velocity. Finally, it may be mentioned, that 'thermal' processes are likely to be associated with microsecond breakdown of liquids, and that 'electronic' processes must play a more important role in breakdown associated with the shorter time scales [45].

2.3 Stochastic Model for Electrical Breakdown

Besides the continuum physical model for dielectric breakdown, another theoretical approach based on a stochastic model exists. Conceptually, the notion is to include the random nature of the streamer breakdown and account for the discrete streamer patterns. Dielectric breakdown in liquids, gases, and solid insulators is frequently characterized by the two following features: (A) The occurrence of narrow

discharge channels, and (B) a strong tendency of these channels to branch into complicated stochastic patterns.

Hence, the discrete, stochastic approach to liquid breakdown attempts to capture the above features. L. Niemeyer, etc. [25] were one of the first to develop such stochastic models. They simulated the fractal structure of dielectric electrical breakdown using the following basic rules for the growth of a discharge pattern:

(A) The pattern grows stepwise.

(B) At each step, one bond is added to the pattern, linking a point of the pattern to a new point.

(C) The addition of bonds occurs with a weighted probability "p" that is a function of the potential difference between the pattern dots and the potential dots. The Niemeyer idea is sketched in figure 2-3 below.

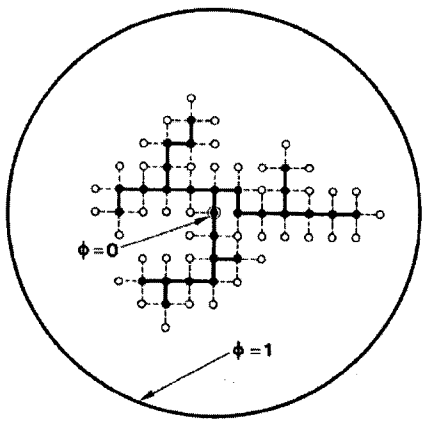

Figure 2-3. Illustration of the stochastic model to simulate dielectric breakdown on a lattice.

In figure 2-3, the central point represents one of the electrodes while the other electrode is modeled as circle at large enough distance. The discharge pattern is indicated by the

black dots connected with thick lines and it is considered equal-potential (ϕ=0). The dashed bonds indicate all the possible growth processed. The probability for each of these processed is proportional to the local electric field [25].

Based on the above simple model for fractal streamer structure, Beroual's group in France [19] recently reported a comprehensive treatment that combines the temporal evolution, a multi-dimensional spatial aspect and inclusion of the internal randomness. However, a major drawback of all the above stochastic approaches is that they lack the physics and inherent quantitative estimations of the various on-going processes. The probabilities, for example, are not derived from first-principles. The rules though logical, do not incorporate a variety of competing process, and the model system lacks memory effects.

CHAPTER III

MODELING AND SIMULATION DETAILS

3.1 Introduction to Liquid Breakdown System Analysis and Modeling

There are at least three different phases within the water electrical breakdown system: solid state (e.g., the electrode), liquid state (such as water), and gas phase (e.g., micro-bubbles inside the liquid). The liquid electrical breakdown is a very complex progress, so it is necessary to systematically analyze the physical properties in detail for the liquid electrical breakdown process. These include internal thermal profiles after nanosecond high voltage pulse, the double layer characteristic at each electrode that can produce possible electrical field enhancements as discussed later, and the electron dynamics within both the liquid and the micro-bubbles. This analysis and detailed properties of the nanosecond water electrical breakdown process are given in section 3.2. A macroscopic method for modeling the double-layer problem at the electrode-liquid interface based on a kinetic, hard-sphere approach utilizing computer-intensive Monte Carlo schemes in presented in section 3.3. Such analysis allows for the inclusion of field-dependent permittivity, and provides a self-consistent spatial distribution of the dipole structure, orientation, ionic concentrations and potentials.

Following these analyses, three liquid breakdown process models are then invoked and discussed. First, a primitive percolative model is given in section 3.4. The percolative model focuses on the heterogeneous conductance property of the liquid, and shows streamer tree-like shape and similar features through simulations based on this model. Second, a two-dimensional (2D) electrical network-based time-dependent model

is given in section 3.5. It improves upon the percolative model by allowing for both energy and electrical field thresholds for breakdown failure instead of simply looking at an electrical field threshold. In addition, this is a time-dependent model utilizing a parallel, random combination of capacitors and resistors in every segment. Finally and most importantly, a complete physically drift diffusion 2D-model is developed and discussed in section 3.6. That model is the most accurate and includes all the important physical processes that affect and influence the breakdown. These physical mechanics include: (a) field emission into bubble through the interface between bubble and liquid, (b) impact ionization in the bubbles, (c) field ionization in the liquid, (d) electric field enhancements at the electrodes, (e) field discontinuities at the micro-bubbles, and (f) time charge transport. Based on this model, many of the salient features seen in actual experimental data are predicted and can be adequately explained. These include: (a) explanations for streamer initiation, (b) streamer propagation and streamer shape, and (c) the observed polarity effect for water breakdown. Finally, in section 3.7, the important features of the model and physics-based mechanisms are summarized.

3.2 Analysis and Properties of Nanosecond Water Electrical Breakdown System.

Before discussions of the modeling details, we begin with some aspects and physical properties relevant to nanosecond electrical breakdown system for water. First, the possible temperature increase in the water system in response to a ~ 100 nanosecond high-voltage pulse is calculated using the finite difference time domain method (FDTD). The central goal is to gauge possible thermal effects, and ascertain whether possible localized evaporation might take place due to strong internal heating. Second, a

microscopic model of the double layer between electrode and liquid is developed and discussed based on a four-slice lattice model. The goal is to demonstrate a field enhancement effect due to the collective dipole orientation. This will later be used in the more comprehensive models. Third, the physics and other characteristic details of electron generation and movement in the liquid, both inside and outside the bubbles under the influence of a nanosecond high voltage pulse, are discussed.

3.2.1 Temperature Configuration After Nanosecond High Voltage (HV) Pulse

The main intent of the analysis in this section is to ascertain whether internal heating can possibly lead to bubble formation in response to a nanosecond-type, high voltage pulse. The high voltage pulse magnitude and duration was chosen in accordance with actual experiments conducted at the Old Dominion University Bio-Electrics Center. For a 200 μm point-plane geometry, a 200 ns, 0.98 MV/cm electric pulse is applied to a point-plane electrodes configuration. The final temperature profile is calculated by FDTD method based on the heat conduction equation:

$$\frac{\partial T}{\partial t} = \kappa \nabla^2 T + U^2 \cdot G(T)/C_P \ , \tag{3.1}$$

where T is temperature, t is time, κ is thermal conductance, U is voltage drop, $G(T)$ electrical conductance of water as a function of temperature T, C_P is water heat capacitance, $U^2 \cdot G(T)/C_P$ is the source term created by the electric energy. We suppose that all of the electric energy transforms into heat energy to obtain an upper limit on the

maximum water temperature. Figure 3-1 shows the electrical conductance of water as function of temperature and was used for the above calculations.

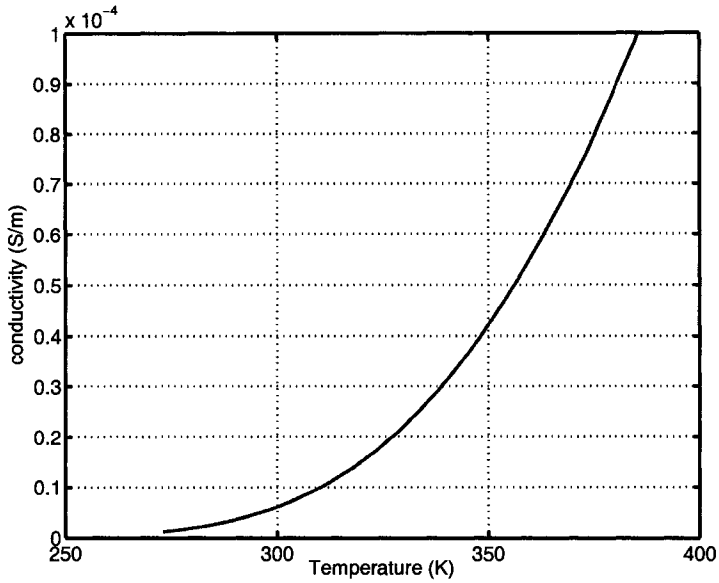

Figure 3-1. Electrical conductance of water versus temperature [46].

The temperature profile obtained is shown in Figure 3-2. The calculations predict that the maximum temperature rise would be on the order of 7 °C. This value is in very good agreement with the experimental measurement. It also clearly demonstrates that internal heating leading to bubble formation would not be possible for the nanosecond-type short pulsed experiments. The energy input from the external voltage is simply not sufficient due to the short pulse duration. Temperature rises on the order of ~ 100 would be needed to vaporize the water and create internal, localized bubbles. Hence, a separate mechanism for electric breakdown must be operative under these short pulse conditions.

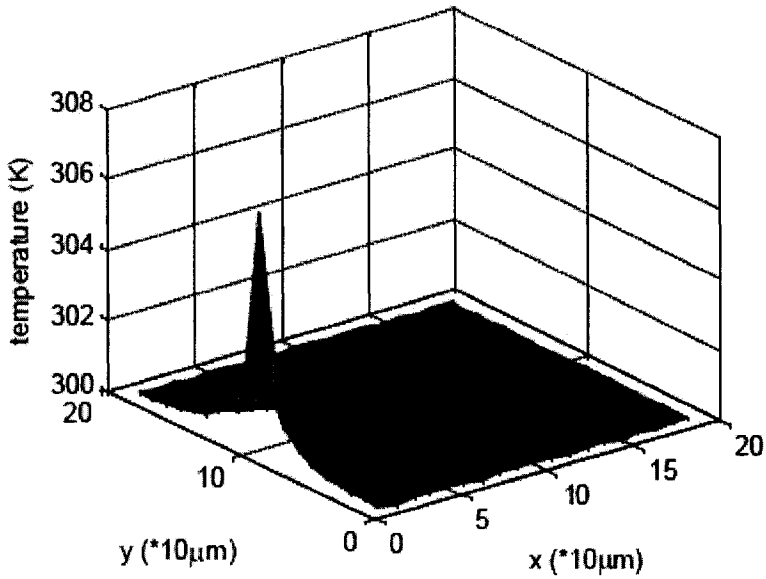

Figure 3-2 Temperature profile after a 200ns, 0.98MV/cm voltage pulse.

3.2.2 Electrical Field Enhancement in the Double Layer Near the Electrode

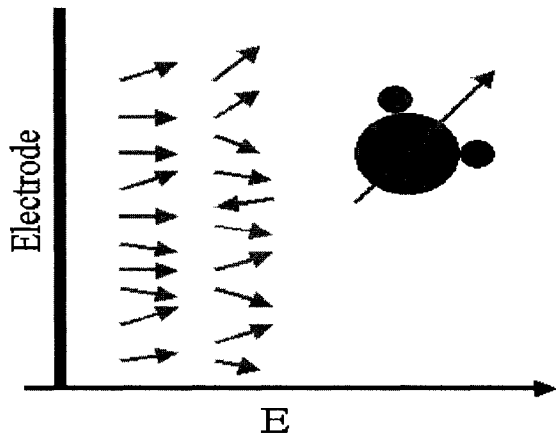

Figure 3-3. Schematic showing possible orientation of the water dipoles adjacent to the electrode due to high fields.

Microscopic treatment of the double layer adjacent to the electrodes, in our model, facilitated precise calculations of the surface electric field. Figure 3-3 shows a schematic

of the water dipoles near an anode. As suggested by the schematic, the applied electric field can potentially orient the dipoles depending on the local electric field. Consequently, the molecular layer closest to the electrode can be expected to have the strongest, collective orientation effect, with decreases into the bulk liquid. Thus, in particular, electric field enhancements due to the collective dipole orientation are included in this picture. As shown through our results later, such field enhancements strongly increase the possibility for electron injection from the cathode contact. This mechanism suggests that it is possibly the onset of such injection at the interface that modulates the device conductivity, and drives the device towards electrical breakdown. The usual Fowler-Nordheim mechanism of tunneling from the metal into the conduction band of water is assumed to hold.

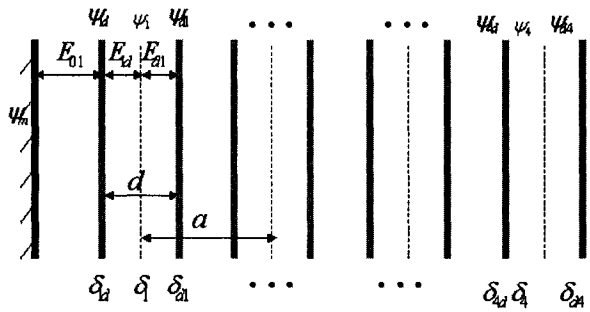

Figure 3-4. A four-slice lattice model of the double layer.

Our microscopic treatment of the double layer on either side was based on a four-slice lattice model as shown in Figure 3-4. The dotted lines represent ions in the form of line charges of density σ_i, while the associated dipole layer consisting of equal and opposite line charges σ_{id} and σ_{di}, are placed on either side of σ_i, at a separation "d", in keeping with the density of water at room temperature. This density d ~ 0.31 nm. The associated electric fields E_{id}, E_{di} and $E_{i-1,i}$ were computed for each layer starting from the

known value at the bulk side of the lattice region. A self-consistent analysis is necessary, since the polarization and charge densities at the layers depend on the electric field and potential values. Thus, for example, the relevant equations linking the electric field and potentials are:

$$\psi_{d,i-1} - \psi_{id} = bE_{i-1,i}, \tag{3.2a}$$

$$\psi_{i,d} - \psi_{i} = (d/2)E_{id}, \tag{3.2b}$$

$$\psi_{i} - \psi_{di} = (d/2)E_{d,i}, \tag{3.2c}$$

$$\psi_{di} - \psi_{i+1,d} = bE_{i,i+1}. \tag{3.2d}$$

The relationship between the field and various charge densities is:

$$E_{i,i-1} - E_{id} = -\delta_{id}/\varepsilon_a, \tag{3.3a}$$

$$E_{id} - E_{di} = -\delta_{i}/\varepsilon_a, \tag{3.3b}$$

$$E_{di} - E_{i,i+1} = -\delta_{di}/\varepsilon_a, \tag{3.3c}$$

$$E_i \equiv \frac{1}{2}(E_{id} + E_{di}). \tag{3.3d}$$

Finally, the polarization and ion densities are assumed to depend on the potentials through the usual equilibrium relations:

$$\delta_{di} = -\delta_{id} = P_i, \tag{3.4a}$$

$$\delta_m = -\sum_{i=1}^{\infty} \delta_i, \tag{3.4b}$$

$$\delta_i = -2qaN_v\delta\sinh(\phi_i)/Z_i, \tag{3.4c}$$

$$P_i = N_v(1-2\delta)p[y_i\cosh(y_i) - \sinh(y_i)/(y_i^2 Z_i), \tag{3.4d}$$

$$\text{and, } Z_i = 2\delta\cosh(\phi_i) + (1-2\delta)\sinh(y_i)/y_i. \tag{3.4e}$$

In the above, $\delta=10^{-4}, \phi_i = q\psi_i / kT$, $y_i = pE_i / kT$, "p" is the dipole moment equal to 6.2 × 10^{-30} Cm for water, "a" the molecular size ~ 0.31 nm, and d ~ 0.25 nm, in keeping with Ref. [47].

Results of the surface electric field at the electrode, based on the four-layer water lattice model, are shown in Fig. 3-5. The x-axis represents the field at the lattice-bulk interface, while the y-axis shows the enhancement factor of the field at the electrode-lattice interface. Values as large as 70 are seen, and imply that electric fields well in excess of 2 × 10^9 V/m can easily be reached at the metallic electrodes, despite much lower values in the bulk. The increased surface field arises from the orientation and alignment of the dipoles. This enhancement makes it possible for electron (or even hole) injections to occur from the contact into the water. The eventual breakdown initiation may partly be caused by strong electron injection and resulting conductivity modulation.

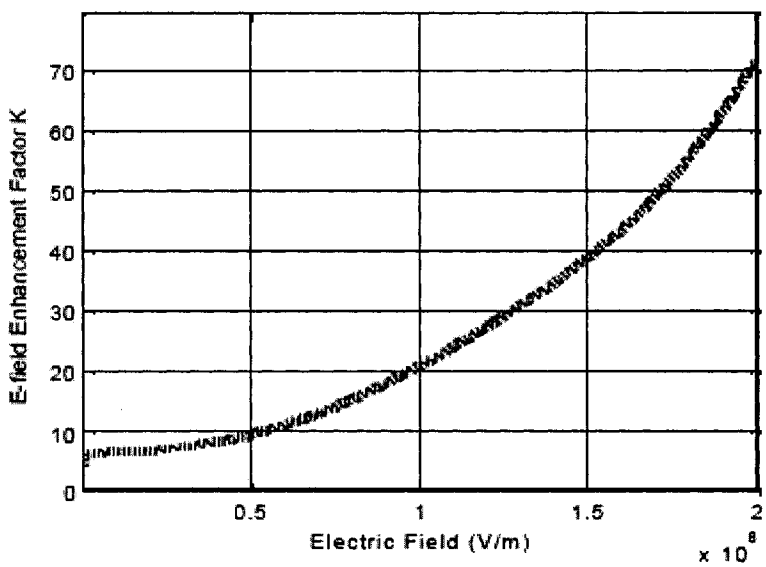

Figure 3-5. Electrical field enhancement factor in the double layer vs. electrical field within the bubble region.

3.2.3 Monte Carlo Analysis to Assess Possible Electron-Initiated Ionization in Liquid Water

The aim of our next analysis, based on the Monte Carlo numerical method, was to test whether free-electrons emitted from cathode could be a possible route for water electrical breakdown through impact ionization as can happen in gas electrical breakdown.

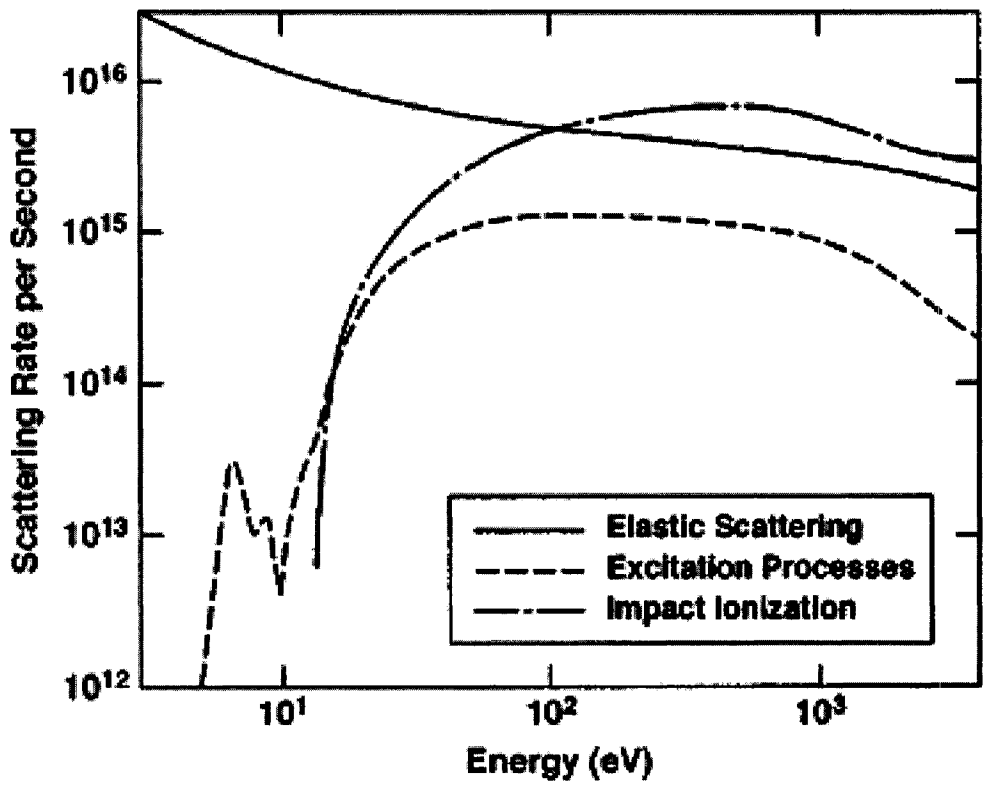

Figure 3-6. Energy-dependent elastic and inelastic scattering rates used for the electron Monte Carlo scattering [48].

Electrons in liquid water undergo energy-dependent scattering that can be either elastic, inelastic ionization, or inelastic excitation [48]. The latter includes transitions

towards the Rydberg or degenerate states, attachment leading to negative ion generation, vibrational and rotational excitation, and excitation of the OH^*, H^* and O^* radicals. In our analysis, the energy dependent cross-sections S(E), were parameterized based on a recent data report [48]. The energy-dependent scattering rates from the cross-sections for elastic scattering, ionization, and all the excitation processes are shown in Fig. 3-6. At low energies, elastic scattering dominates, and can thus be expected to lead to low mobilities and electron energies. This is particularly true under conditions of isotropic angular scattering.

The Monte Carlo scheme is a stochastic, kinetic approach that involves the space-time dynamical evolution of a swarm of simulation particles. The particles are taken to obey Newtonian mechanics, and their movements consist of a series of free-flights, peppered by random scattering events [49]. Based on the self-scattering (or the null scattering) technique, the stochastic free-flight time t_{FF} (or mean-time-to-collision) is obtained from the maximum scattering rate R_{max} as: $t_{FF} = - [Ln (r)]/ R_{max}$, where r is a random number, and "Ln" stands for the natural logarithm. The R_{max} value is obtained by taking the maximum of the various energy-dependent scattering rates $R_i (E)$ with all the elastic and inelastic processes taken into account. In general, the scattering rate R(E) is related to the corresponding cross-section S(E) for that process as: $R(E) = S(E) N v(E)$, where N is the density of water molecules, and v(E) the energy-dependent electron velocity.

Monte Carlo (MC) simulations were carried out by injecting a swarm of 6000 particles from the cathode at a given electric field. The electric field was not updated (as is usually done in "particle-in-cell" codes [50]) on the assumption of a low electronic

charge density. The initial energies were assigned based on a thermalized Boltmann distribution. A time step of 0.01 fs was used for the highest water density (i.e. 1 gm/cc) because of the high elastic scattering rate shown in Figure 3-6. The angular distribution was taken to be isotropic for the inelastic processes. For elastic scattering, a Rutherford-Moliere [48] differential cross-section S(θ) of the form:

$$S(\theta) = K_1 / [K_2 - \cos\theta], \tag{3.5}$$

was used, with K_1 and K_2 being angle independent constants based on the energy, atomic number, and screening parameter [48]. From equation 3.6, the angle selection for the final state after elastic scattering can be ascertained from the distribution S(θ), by invoking a random number "r' and using the following relation:

$$r = \left[\int_0^{\theta} S(\theta)\sin\theta d\theta\right] / \left[\int_0^{\pi} S(\theta)\sin\theta d\theta\right] \quad . \tag{3.6}$$

Carrying out the integration, leads to a closed form expression for the angle θ in terms of the random number "r". Figure 3-7 shows the angular distribution as a function of the random number for three electron energies. As evident from the curves, the scattering is almost isotropic for small energies, and shifts towards anisotropic, small forward angle behavior only at very large energies. This essentially implies that electrons injected from the cathode are likely to be *heavily scattered in a random fashion*, and that they would be unable to pick up much energy.

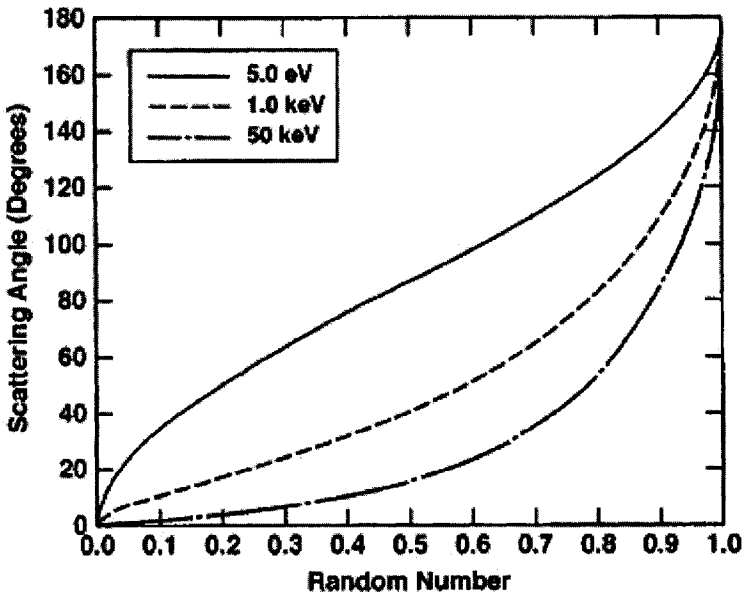

Figure 3-7. Angular distribution with random number for elastic scattering for three different electron energies.

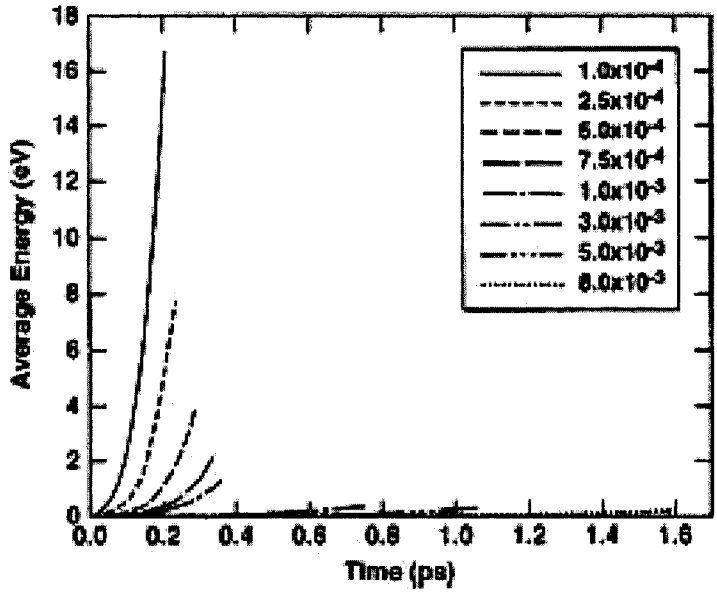

Figure 3-8. Time-dependent Monte Carlo results showing the swarm kinetic energies at a 108 V/m field for various density factors.

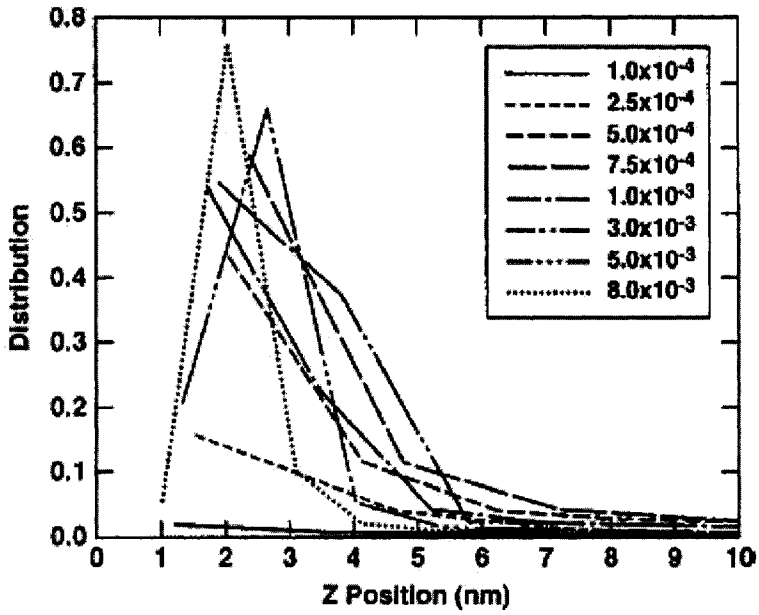

Figure 3-9. Spatial distribution of the electron swarm from the cathode (at z=0) after 1.6ps.

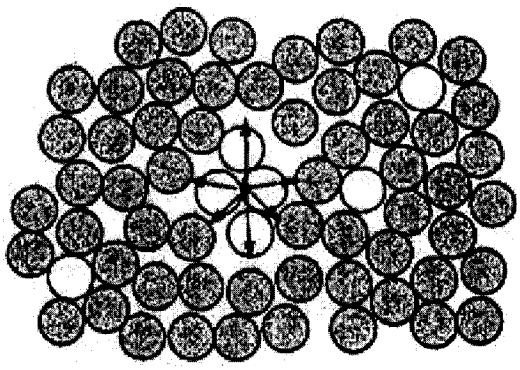

Figure 3-10. Schematic representation of the processes of electron trapping into liquid [51].

Clearly, the scattering rate depends on the liquid density N. The most favorable condition for energy gain and arguably a pathway to possible impact ionization occurs at low densities. This situation can occur for long voltage pulses that can cause internal heating and bubble formation, or under optical excitation. In order to ascertain the density dependence for possible impact ionization, we carried out MC runs for different water density values (hence, different scattering rates) by releasing 6000 electrons from

the cathode and following their trajectories for relatively short times. The distributions of the swarm in position and energy-space, as well as the production of secondary electrons due to ionization, were monitored. Figure 3-8 shows the time-dependent mean swarm energy at a field of 10^8 V/m and various fractional density factors F (here F = 1 indicates the normal water density). As the density is decreased, the scattering rates scale down to lower values, thereby increasing the velocity and energy of the particles. A snapshot of the spatial electron swarm distribution from the cathode (at z = 0) after 1.6×10^{-12} second is shown in Figure 3-9. Most electron particles are seen to still lie near the cathode. For the higher F values (corresponding to highest scattering and smallest mobility), the distribution is bunched more tightly, and shows a peak towards low z-values. Schematic representation of the processes of electron trapping into liquid is shown in figure 3-10.

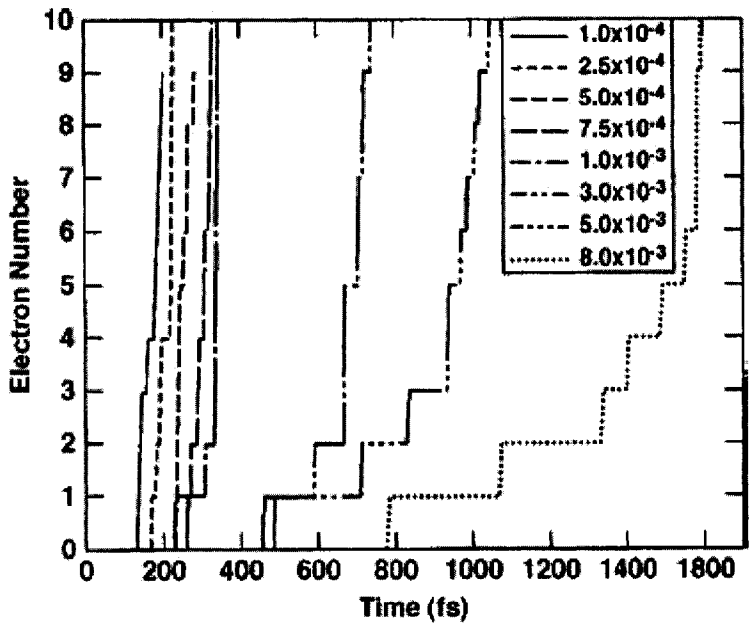

Figure 3-11. Time evolution of the number of ionization events for a 1×10^8 V/m field and various density factors.

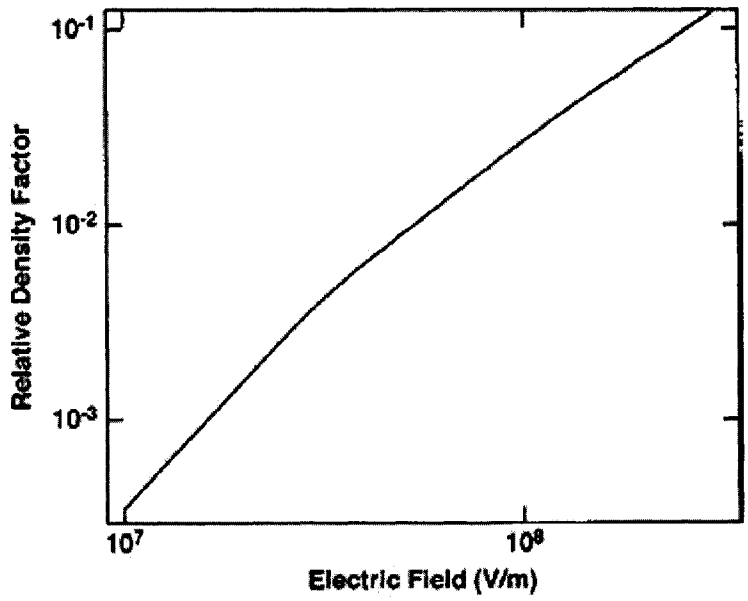

Figure 3-12. Monte Carlo calculation of the water density factor vs the maximum electric field required for ionizing multiplication.

The number of impact ionization events for the 10^8 V/m field are given in Figure 3-11. At the highest density factor of 0.006, substantial numbers of secondary charge carriers are predicted within a relatively short time. However, upon increasing the density factor to about 0.01 (not shown) resulted in almost no ionization event, and a very low drift velocity. In our simulations, higher electric fields were also used, and the corresponding upper bound on F required for initiating ionization events decreased. Figure 3-12 shows a plot of the electric field versus the maximum allowable density factor for ionization. For the peak breakdown fields of about 4×10^9 V/m for water observed experimentally [2,10], our results indicate that normal water densities would be too high to facilitate the ionizing avalanche necessary for triggering breakdown. This clearly demonstrates that electron injection at the cathode cannot play a dominant part in breakdown for the short-pulse conditions, and is only likely to produce slow moving negative ions (through trapping or attachment), or quasi-localized electron bubbles.

In summary, it has been shown here on the basis of Monte Carlo simulations that breakdown would not be the result of electron impact ionization from cathode injection. The results showed that strong elastic scattering, coupled with the highly isotropic angular deflections, prevent electrons from picking up the requisite energy. Consequently, the energy distributions were predicted to remain far below the threshold for impact ionization, despite the high external electric fields. It was also shown that only under low-density situations (as might exist due to bubble formation or partial vaporization), or upon external photo-excitation, might the electron impact ionization process be operative.

3.2.4 Monte Carlo Analysis for Electron Impact Ionization in a Bubble

In this subsection, we report and discuss a three-dimensional, time-dependent Monte Carlo analysis of electron transport in liquid water. The MC scheme is used here to furnish the relevant transport parameters for a continuum model based on the drift-diffusion scheme in section 3.6 using the same method as in section 3.2.4.

Monte Carlo simulations were carried out by injecting a swarm of 8000 particles into the micro-bubble at the gas-liquid interface for a given electric field. As a result, characteristics of the electron dynamics through the gas bubble, followed by their traversal in water, were obtained. Figure 3-13 shows the basic configuration. The concept is that electrons can be released from one side of the liquid-bubble interface through field-emission. The relatively high electric field created by the discontinuity in dielectric constant at the interface would facilitate such electron emission. These emitted particles can then undergo acceleration within the bubble and impact ionize the gas within the

bubble upon gaining kinetic energy. Electron scattering within the bubble was implemented based on cross-sections reported in the literature [52-54]. The initial energies were assigned based on a thermalized Boltmann distribution. A time step of 0.01 fs was used for the highest water density (i.e. 1 gm/cc) because of the high elastic scattering rate shown in Figure 3-6. The angular distribution was taken to be isotropic for the inelastic processes. For elastic scattering, a Rutherford-Moliere [48] differential cross-section was used.

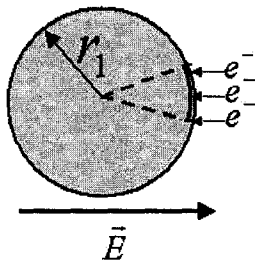

Figure 3-13. Monte Carlo simulation of electron impact ionization inside the bubble.

Figure 3-14 shows time dependent populations for swarms of 8000 electrons released simultaneously from one end of the bubble-water interface. Various cases for different bubble radii R, and applied electric fields F are shown. All the curves of Figure 3-14 exhibit a similar trend. An initial time delay is apparent in all case – this is the "dead time" during which the electrons are within the bubble region and are picking up the requisite energy for impact ionization. The swarm then begins to produce secondary particles through the impact ionization process, and the overall population increases. This time delay naturally depends on the electric field and the bubble radius.

Strong increases in electron population roughly begin to occur when the swarm reaches the opposite end of the bubble, and begins to enter the water. The high density within the liquid works to increase the scattering rate, and a sudden onset of ionization

follows. In our simulation, particles in the water with energies below the ionization thresholds are removed from consideration, as essentially having thermalized. The time-dependent ionization replicas seen in Figure 3-14 arise from a cyclical effect. First, low energy particles from the swarm continually pick up energy from the electric field, reach the ionization threshold, and then fall back into lower energy states upon impact ionization.

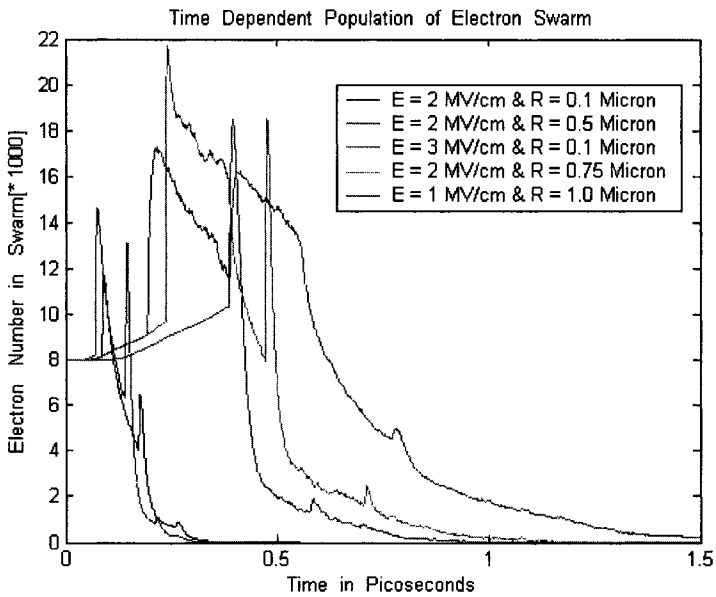

Figure 3-14. Monte Carlo results for the time-dependent swarm starting with an initial 8000-particle population.

Monte Carlo results for the time-dependent secondary particle production both inside and outside the bubble are given in Figure 3-15 and Figure 3-16. The values depend on the bubble radius and external electric field, with initial delay times in the sub-picosecond's regime. For the 8000 electron swarms, multiplicative gain factors of about 0.625 (=5000/8000) and 62.5 (=500,000/8000) are predicted inside and outside the bubble region, respectively. Furthermore, the number of electrons produced *outside the*

bubble is always more than the secondary particles created within the bubble. This arises from the higher density in the liquid phase and hence, the higher collision rate for the high-energy electrons.

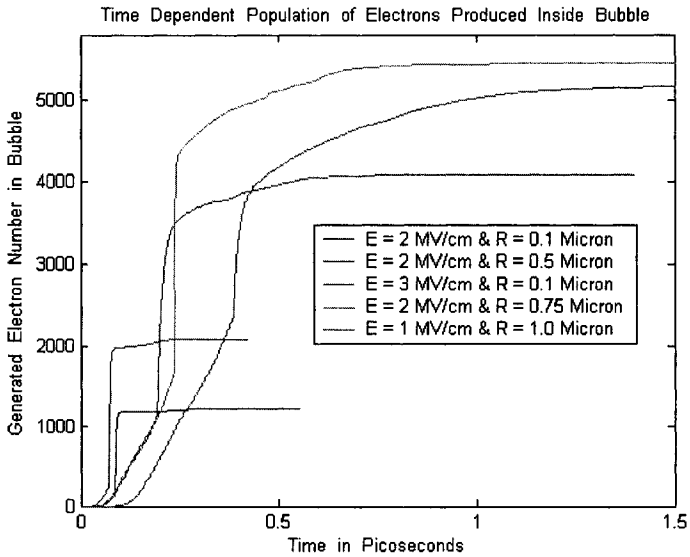

Figure 3-15. Monte Carlo results showing secondary particle generation inside a bubble as a function of time due to an initial 8000-particle swarm.

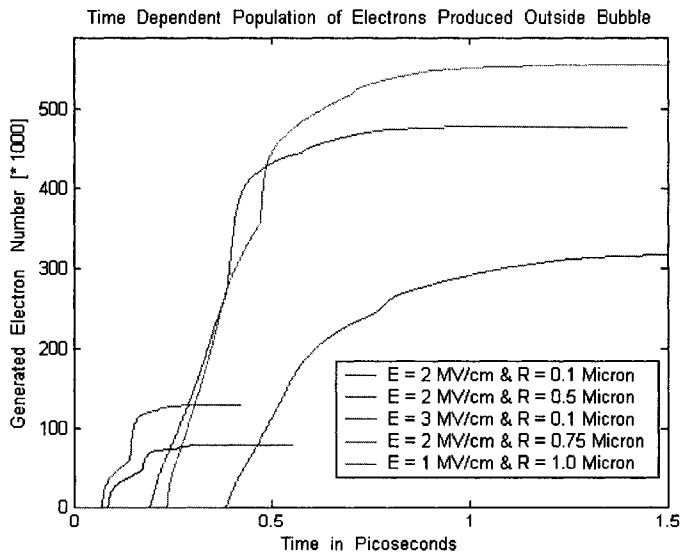

Figure 3-16. Monte Carlo results showing secondary particle generation outside a bubble as a function of time due to an initial 8000-particle swarm.

3.3 Field Dependent Liquid Water Permittivity Calculations Based on an Atomistic Method

3.3.1 Introduction

Though the electrical behavior of dielectric liquids (especially water) subjected to high electric fields has been intensively studied [11-20], there is still no comprehensive understanding of all the inherent physics. In section 3.2.2, the electrical field enhancement in double layer was calculated on the basis of the Gouy-Chapman theory [55, 56]. However, the effects of steric repulsion cannot be included directly in the Gouy-Chapman model. Here the most reliable and direct methods for modeling the double-layer problem at the electrode-liquid interface have been through the kinetic, hard-sphere approaches based on computer-intensive Monte Carlo and Molecular Dynamics schemes [57-61]. In these schemes, dipole re-alignment effects, ion-ion correlation, finite size effects are all comprehensively included. These numerical models capture many important features, such as the re-alignment of the strongly polar water molecules due to electrostatic interactions.

In the next subsection, details of a static, canonical Monte Carlo approach are discussed for addressing the problem of field-dependent permittivity. The MC technique was chosen and applied for the analysis of the double layer static properties near a metallic surface. Based on the water rigid SPC/E molecular model, energy minimization was used to update the water molecule position and angular distribution. Na^+ and Cl^- ions were also considered. Simulation results were shown following the modeling details.

3.3.2 Modeling detail

The ions (for a given user specified average density) were modeled as charged Lennard-Jones (LJ) spherical particles. Here, Na^+ and Cl^- ions were considered. Water molecules were treated in terms of the rigid SPC/E model, which consists of three partial charges located on the oxygen and hydrogen sites [62] as shown in figure 3-17 and parameters are shown in table 3-1.

Unlike most previous reports, the dipole-ion and dipole-dipole interactions were explicitly included in our calculations, in addition to the usual many-body, ion-ion interactions. The LJ parameters for the ion-ion and ion-water interactions were taken from reports in the literature [63, 64] as shown in table 3-2. The interaction of the electrolyte solution with the metal electrode was assumed to consist of a non-electrostatic due to the externally applied electric field, and an electrostatic image charge contribution. Surface corrugation effects and interactions between metal-oxygen and metal-hydrogen, as described by Spohr [65] were incorporated into the simulation model. The corrugation attempts to describe the surface inhomogeneity due to the discrete location of atomic cores. In this scheme, the metal-oxygen interaction is described by a Morse function, augmented by a corrugation term. The metal-hydrogen interaction is modeled by an exponentially repulsive potential [65]. The corrugation is felt only in the repulsive part of the Morse potential function, and was taken to have a periodicity of 3.6 μm in both directions parallel to the surface. The metallic nature of the electrode (perfect conductor) was modeled by the image charge method, with the image plane locate at the $z = 0$ boundary, and the solution lying in the $z > 0$ region. Each charge q_j in the system, whether a partial charge of the water molecule, or an ionic charge, was taken to interact

with all other real charges and also the image charges q_j^I (= - q_j.). Potential between water molecule and surface is:

$$U_\mu = \phi_O(x_O, y_O, z_O) + \phi_{H1}(x_{H1}, y_{H1}, z_{H1}) + \phi_{H2}(x_{H2}, y_{H2}, z_{H2}) \tag{3.7a}$$

$$\begin{aligned}\phi_O(x,y,z) &= \frac{12\times10^3}{6.02\times10^{23}} \times \left[e^{-2\left(z-3\times10^{-10}\right)} - 2\times e^{-\left(z-3\times10^{-10}\right)}\right] \\ &+ \frac{1.2\times10^3}{6.02\times10^{23}} \times e^{-2\left(z-3\times10^{-10}\right)} \times \left[\cos\left(\frac{10\pi x}{L_x}\right) + \cos\left(\frac{10\pi y}{L_y}\right)\right],\end{aligned} \tag{3.7b}$$

$$\text{and}, \quad \phi_H(x,y,z) = 2.4\times e^{-(z+4)}, \tag{3.7c}$$

where (x_O, y_O, z_O), (x_H, y_H, z_H) are the positions of oxygen and hydrogen in water molecule, $\phi_O(\cdot)$ is the potential of oxygen atom, and $\phi_H(\cdot)$ is the potential of hydrogen atom. The intermolecular interaction between molecules a and b consists of the Coulomb interactions between the charged sites and a single Lennard-Jones term between oxygen atoms:

$$U_{\mu\mu}\big|_{ab} = \sum_i^{on\ a} \sum_j^{on\ b} q_i q_j e^2 / r_{ij} + 4\varepsilon\left[\left(\frac{\delta}{r_{ij}}\right)^{12} - \left(\frac{\delta}{r_{ij}}\right)^{6}\right], \tag{3.8}$$

where r_{ij} is the distance between two molecules, δ, ε are the specific Lennard-Jones parameter, different for different interacting particles. For water molecules, $\varepsilon = 0.6501696 kJ/mol$, and $\delta = 0.3165555 \ \overset{o}{A}$.

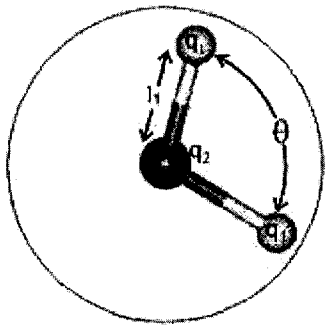

Figure 3-17. SPC/E model of single water molecule [66].

Table 3-1 SPC/E water molecule model parameters [66] for figure 3-17.

Model	δ (Å)	ε (kJ mol^{-1})	l_1 Å	q_1	q_2	θ
SPC/E	3.166	0.650	1.0000	+0.4238	-0.8476	109.47

Table 3-2. Anion and cation LJ parameter for NaCl [67].

		cation–cation		anion–anion		cation–anion		cation–oxygen		anion–oxygen	
Case	Name	σ/Å	(ε/k)/K	σ/Å	(ε/k)/K	σ/Å	(ε/k)/K	σ/Å	(ε/k)/K	σ/Å	(ε/k)/K
I	reference	3.169	78.2	3.169	78.2	3.169	78.2	3.169	78.2	3.169	78.2
II	small cation	2.730	78.2	3.169	78.2	2.950	78.2	2.950	78.2	3.169	78.2
III	large anion	3.169	78.2	4.860	78.2	4.015	78.2	3.169	78.2	4.015	78.2
IV	small cation–large anion	2.730	78.2	4.860	78.2	3.795	78.2	2.950	78.2	4.015	78.2
V	NaCl	2.730	43.0	4.860	20.2	3.870	20.5	2.876	62.7	3.250	62.7

In our simulation, electrode surface sit in the plane (z =0). With the size of each direction is $L \times L \times H$, where $L = H = 1.86392 \times 10^{-9} m$, The simulation volume (z > 0) consisted of a mixture of N_+ cations with charge q_+ of particle diameter d_+, and N_- anions of charge q_- with particle diameter d_-, in addition to N_μ dipoles of moment μ and diamater d_μ. The SPC/E model was used to assign partial charges to each water dipole cluster. The particles were confined in a rectangular simulation. Hard walls were assumed along the

boundaries normal to the z-axis, and periodic boundary condition were applied along the lateral directions.

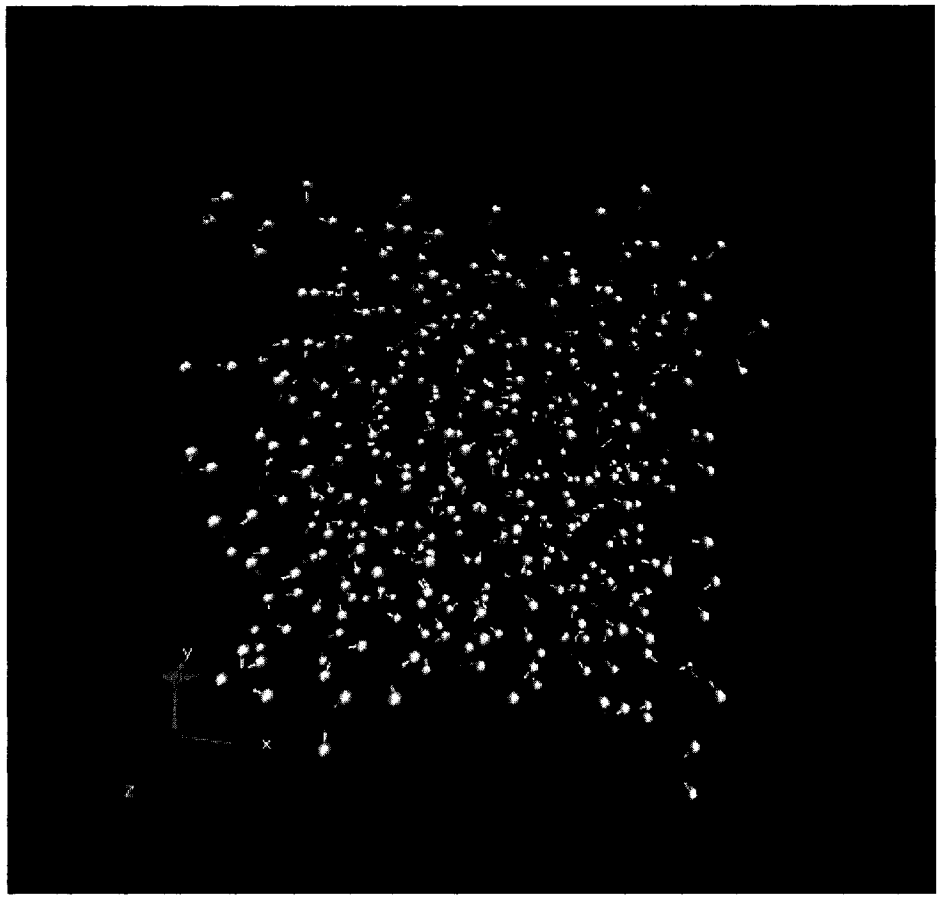

Figure 3-18. Total water molecules for Monte-Carlo model, with electrode sitting in z=0 plane.

The potential energy of the system was obtained by a pairwise summation of all the two-particle interactions, and the one-particle energies U_i , U_μ for ion and molecule respectively in the externally applied field. Long-range corrections for the Coulomb interactions were taken into account by a tabulated version of the Ewald sum for a slab system with infinite extent along the two transverse directions [68]. The pair interactions acting between the various species of molecules are the well-known multipole potentials with the corresponding hard sphere (HS) repulsive cores. The HS core potential U_{HS} (r_{ij},

d) had the usually form: $U_{HS}(r_{ij}, d) = 4$ for $r_{ij} < d$, and $U_{HS}(r_{ij}, d) = 0$ otherwise. The two-particle energies for the ion–ion (U_{ii}), the ion-dipole ($U_{i\mu}$) and the dipole–dipole ($U_{\mu\mu}$) terms were taken from the work of Boda et al. [69]. So the total system energy can be expressed as:

$$U_{total} = U_{\mu\mu} + U_{i\mu} + U_{ii} + U_i + U_{\mu}. \quad (3.9)$$

For the Monte Carlo simulations, the initial configuration set up by placing the N_+ cations, the N. anions, and N_μ water molecules randomly within the simulation volume. A random orientation of the hydrogen atoms with respect to the oxygen was assigned as the initial starting condition for all the water molecules. This yielded the total initial energy of the system. Subsequently, at each step, a randomly chosen particle was moved to a new location within the simulation box. This move was accepted only if it decreased the resulting energy of the system. As a result, the system configuration was made to evolve towards a lower energy state through such random assignments.

In our MC simulation, 216 water molecules (the over all view is shown in Figure 3-18) and 4 pairs of Na^+ and Cl^- ions were placed into a rectangular box of dimensions $L \times L \times H$, where $L = H = 1.86392 \times 10^{-9} m$. The entire simulation procedures was based on the following steps:

1. Choose six random variables for every water molecule: (x_μ, y_μ, z_μ), two Euler angles ϕ, θ, ψ, ($0 \le \theta < \pi$, $0 \le \phi < 2\pi$, $0 \le \psi < 2\pi$), and 3 random position variables (x_I, y_I, z_I) for every ion, such that there is no overlap of particles,

i.e. $r_{ij} > (d_i + d_j)/2$. $\forall i, j, i \neq j$, r_{ij} is the particle distance, d_i, d_j is the diameter of two particles respectively.

2. Next, calculate the system energy U_{total}
3. Randomly move one molecule dipole or one ion to a new position or direction, or both.
4. Recalculate the system energy U_{total}. If the system energy decreases, then accept the movement. Otherwise, give up the movement and re-set the system to its initial configuration.
5. Go back to step 3 and repeat this process a large number of times. Here typically, a millions steps were chosen. The water molecule dipoles states and ions positions were recorded during the last 1000 steps.

These configurational jumps were repeatedly well over a million times to evolve the system towards a stable, final-state configuration. The simulations were carried out for a constant global density of 10^3 Kg m^{-3}, and so no additions or deletion of particles was permitted. Values of the dipole moment yielded the relative permittivity (ε_r) based on the second central moment, as given by the following relation [70, 71]:

$$\varepsilon_r = 1 + \frac{4\pi}{3} \frac{\langle M^2 \rangle - \langle M \rangle^2}{\varepsilon_0 V k_B T} \quad , \tag{3.10a}$$

where <M> is the mean dipole moment of the water molecules, ε_0 the free-space permittivity, V the volume, k_B the Boltzmann constant, and T the temperature in Kelvin. In order to eliminate the influence of the choice of coordinate axes on the calculated

fluctuation, the total dipole moment fluctuation $\left(M-\langle M\rangle\right)^2$ was calculated from the components of M along each axis:

$$\left(M-\langle M\rangle\right)^2=\langle M^2\rangle-\langle M\rangle^2=\langle M_x^2\rangle-\langle M_x\rangle^2+\langle M_y^2\rangle-\langle M_y\rangle^2+\langle M_z^2\rangle-\langle M_z\rangle^2. \quad (3.10b)$$

3.3.3 Results and Discussion

The Monte Carlo (MC) scheme was applied to analyze the electric double layer at the electrode-water interface with consideration of both the ions and water-dipoles. Results are first presented for pure water without any ions for simple model validation. Figure 3-19 shows the radial distribution function (RDF) between oxygen atoms, $g_{oo}(r)$, obtained from the present MC simulations. The RDF represents the probability of finding a second particle at a separation r from the first, and so provides information on the local structure of a molecular system. Our result for $g_{oo}(r)$ matches previous experimental reports obtained from neutron diffraction and X-ray scattering measurements [72, 73], and is also in keeping with other calculations [66]. The hydrogen-hydrogen and hydrogen-oxygen RDFs (not shown), were also in good agreement with published reports. Results of the dielectric function for pure water in the absence of any ions or impurities, or external electrode potential, from the dipole moments (as given in eqn.3.10), are shown in Figure 3-20. The values were obtained as a function of the MC simulation steps. The overall magnitude is seen to fluctuate in a range close to the accepted value of ~ 80 for water, and stabilizes at about 77.01 after 30 million Monte Carlo steps. The curve of Figure 3-20 represents the global average for the entire simulation region. The spatial variation, obtained from the MC code is shown

in Figure 3-21 along a direction (z-axis) normal to the metal electrodes. An average over the last 1000 time steps was used for smoothening the data of Figure 3-21. The main feature, once again, is the nearly uniform value of about 77.01 with some fluctuating behavior.

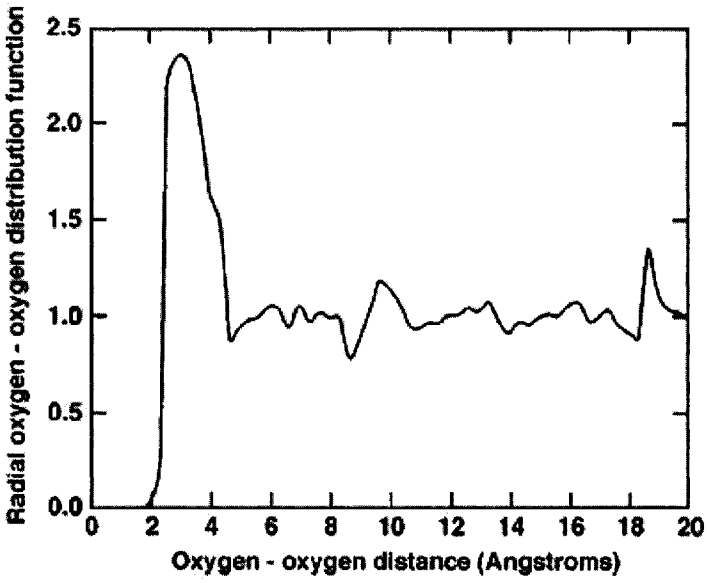

Figure 3-19. Simulations results showing the radial distribution function $g_{oo}(r)$ for pure water.

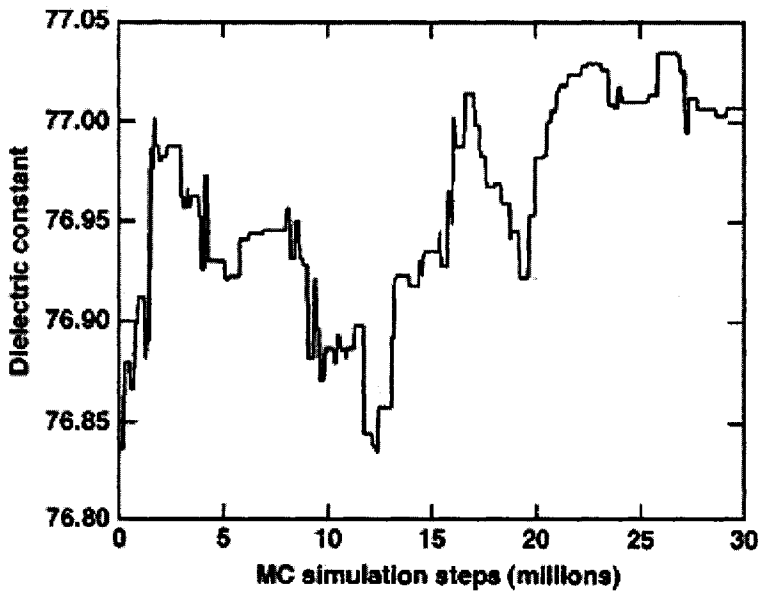

Figure 3-20. Calculations of the global dielectric function for pure water in the absence of any ions or impurities, or external electrode potential, as a function of simulation steps.

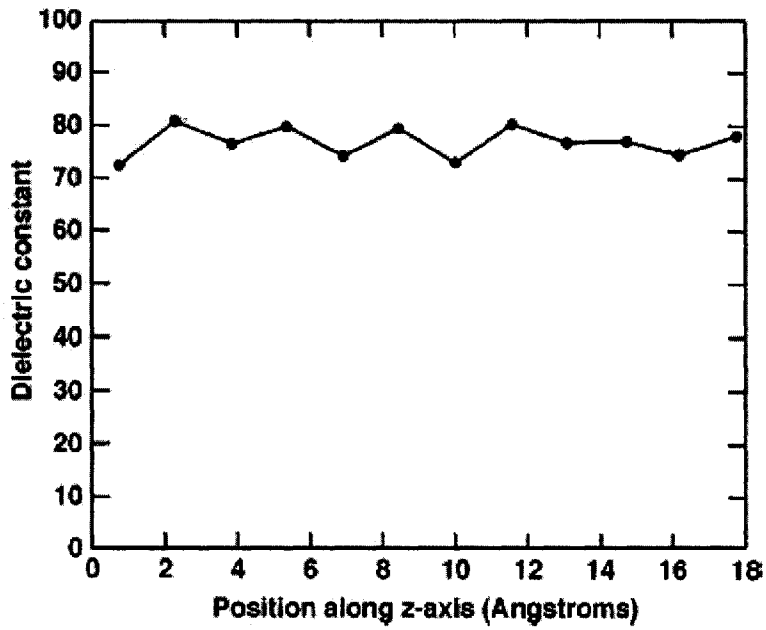

Figure 3-21. Spatial variation obtained in a direction (z-axis) normal to the metal electrodes for pure water without an external field.

The field dependence of the dielectric function was next probed by running the MC simulations for pure water, but with a uniform potential at the electrodes. A negative charge density of 0.5 C m^{-2} was assigned at the left wall (the cathode), taken to lie in the z = 0 plane. Due to the presence of this high electric field at the surface, strong orientation of the water dipoles can be expected, that should lead to a decrease in the value of the dielectric function. Results of ε_r from the simulation close (within 20 angstrom) to the electrode surface are shown in Figure 3-22 as a function of the MC steps. A final value of roughly 5.0 is obtained, and is indicative of the strong alignment effect produced by the electric field that significantly lowers the local permittivity. As might be expected, the molecular orientation effect is the strongest near the electrode boundary (at z = 0), and gradually weaken with distance. Figure 3-23, which shows the spatial

dependence of the dielectric function, provides a quantitative picture. Within about 18 angstrom, the value is predicted to roughly double, starting from about 5 at the electrode interface. Such a transition from a very ordered layer near the surface to a more disoriented region further from the electrode surface have been predicted by lattice models [47]. This dipole ordering and its spatial dependence normal to the electrode surface, is better reflected in the angular distribution of Figure 3-24. The dipole angle θ, with respect to the z-axis, is a variable between 0 and π. Due to dipole orientation, the values of θ are closer to π as seen in Figure 3-24, with a gradual trend towards randomization with increasing distance z from the metal surface.

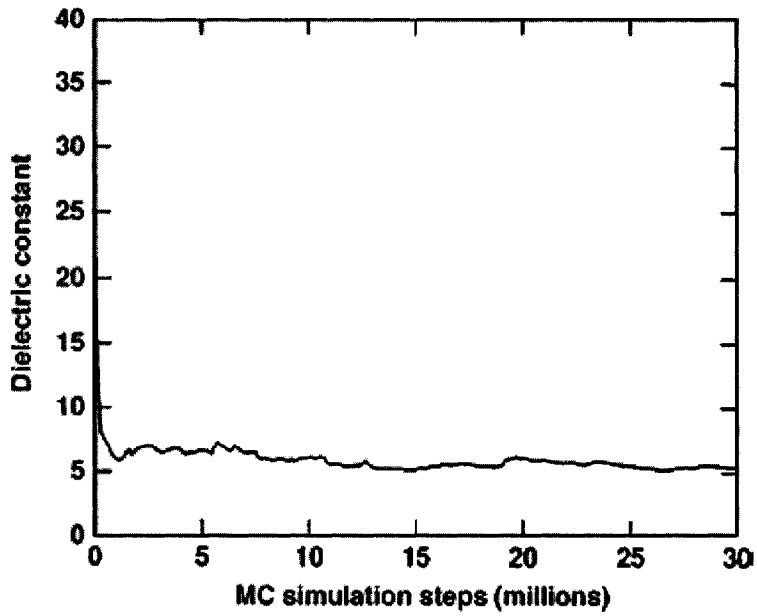

Figure 3-22. Calculations of the relative permittivity close to the electrode (within 20 angstrom) as a function of the MC steps for pure water. A charge density of 0.5 C m^{-2} was assigned to the left wall at z = 0.

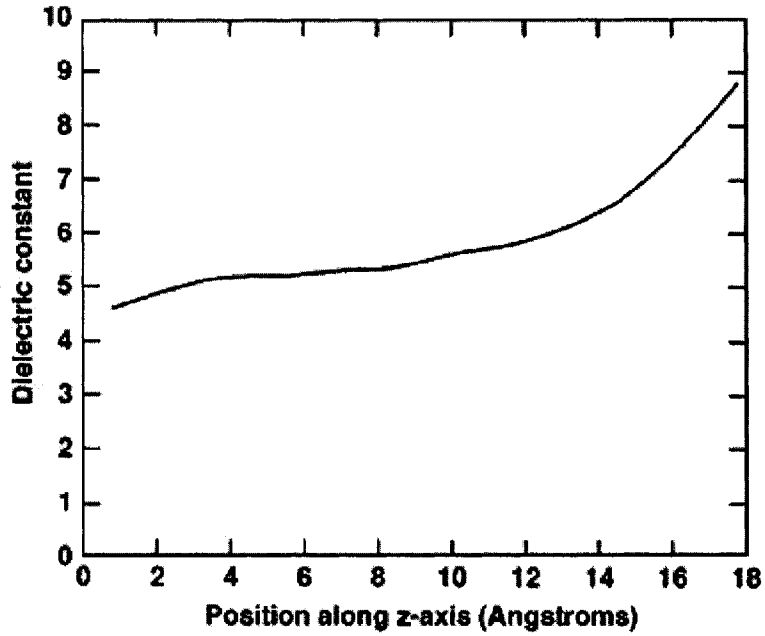

Figure 3-23. The spatial dependence of the dielectric function for the case of Figure 3-22.

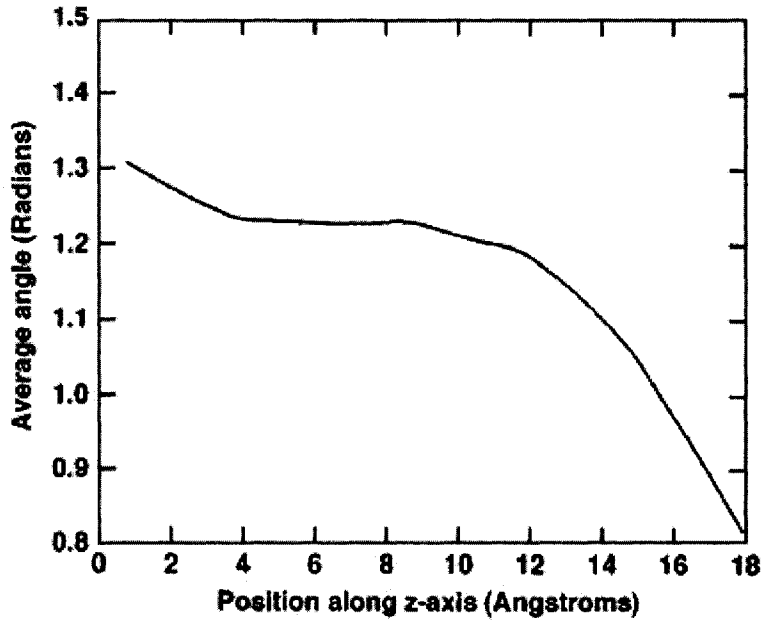

Figure 3-24. The corresponding angular distribution of the water dipoles as a function of the normal distance.

Based on position dependent evaluations of both the electric field (E) and relative permittivity from the MC simulations, the relation between ε_r and E was next obtained.

Varying the initial charge density on the metallic electrode allowed for changes in the peak electric field. Monte Carlo data for the relative permittivity thus obtained is shown in Figure 3-25, along with a recent theoretical prediction [74]. The MC calculations were limited to a finite electric field range due to the computational burden. In any case, Figure 3-25 reveals very good agreement with a previous analytical calculation, and clearly demonstrates the monotonically decreasing trend in permittivity with electric field. Position dependent data (along the z-axis) for both the electric field and permittivity was then used for calculations of the internal pressure based on the Maxwell stress tensor. The internal pressure due to the electric field stress as a function of position is shown in Figure 3-26. Combining the pressure P(z) along the z-distance with the electric field variation along z, yielded the pressure versus electric field curve. This is indirectly indicative of the electrostrictive effect at high electric fields in water. Figure 3-27 shows the simulation data for electric fields in the 2×10^{9} Vm^{-1} to 6.5×10^{9} Vm^{-1} range. A recent analytical prediction [74] is also shown for comparison. The figure demonstrates that very large pressures on the order of GPa can be created at the high electric fields.

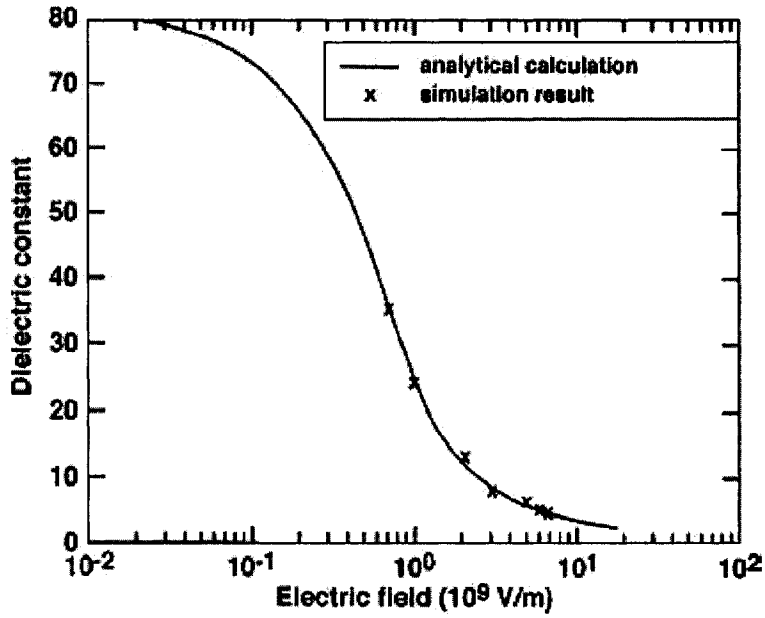

Figure 3-25. Data points for the field dependent relative permittivity obtained and a theoretical curve of Ref. [74].

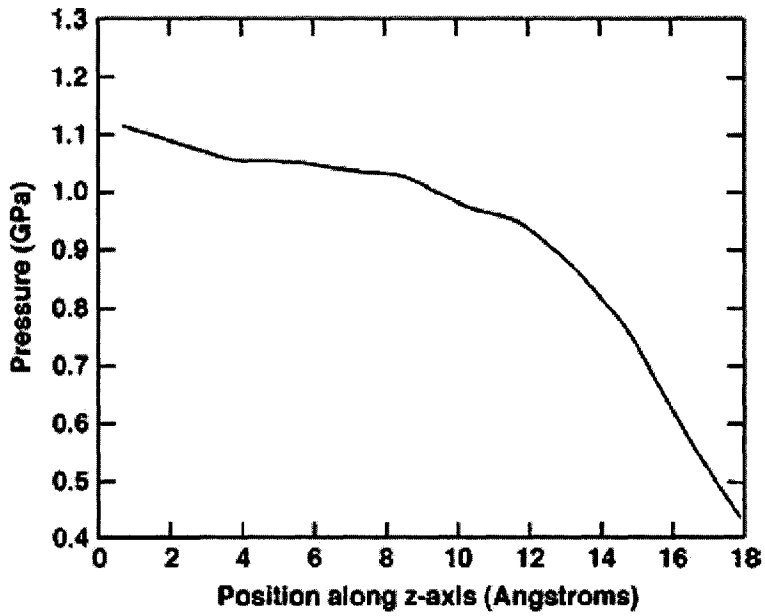

Figure 3-26. Internal pressure due to the applied potential, as a function of the z-distance. A0.5 Cm^{-2} charge density was assumed at the z = 0 electrode.

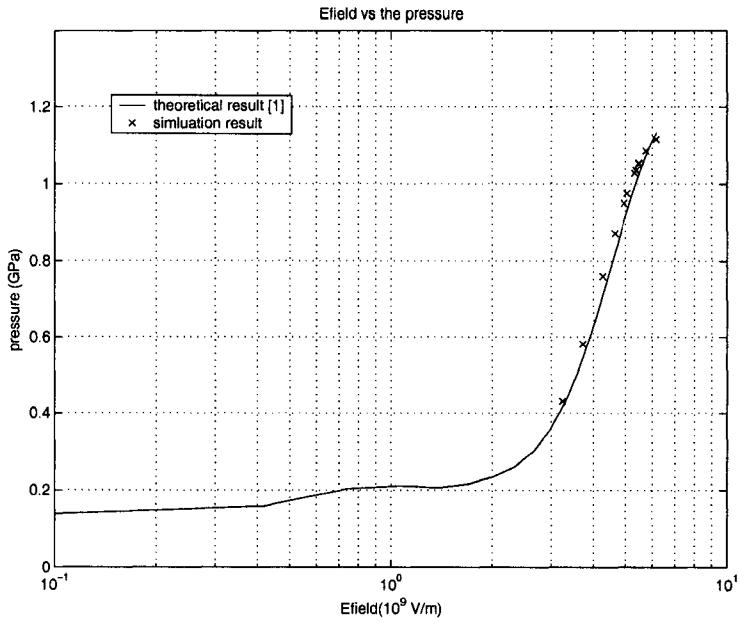

Figure 3-27. Data points for the pressure versus electric field obtained from the simulations, and a theoretical curve from Ref. [74].

Having discussed the role of the electric field on the polarizability and dipole orientation in pure water, simulation results that include Na^+ and Cl^- ions are presented next. Three ion pairs were used for the cubical simulation box. As previously stated, the initial condition for all water molecules consisted of a random orientation of the two hydrogen atoms at a fixed distance from each oxygen site. The z-dependent dielectric constant, near the negative electrode, obtained from MC simulations, is shown in Figure 3-28. A quick comparison between the previous calculation for pure water (given in Figure 3-23) and the present result reveals two very important features. (i) First, a fairly pronounced local maxima in ε_r is evident near the 4 angstrom. Physically, this behavior can be understood in terms of the field perturbation caused by the Na^+ ions. The region close to the electrode surface has a random distribution of Na^+ ions, each with a finite radius of about 1.9 angstrom. The first layer of ions is, on an average, at a distance of

about 2 angstrom from z = 0. Due to the inter-atomic, core-repulsion, the next set of ions is separated by roughly 4 angstrom. Thus, near the z ~ 4 angstrom plane lies approximately midway between two adjacent sheets of ions, and has a lowest resulting electric field. Consequently, the magnitude of ε_r is predicted to be the highest at around this location. At large distances (i.e., z > 12 angstrom) the density of ions is no longer as high, and so the ionic perturbative effects to the overall electric field distribution become less pronounced. A gradual, monotonic increase in ε_r is predicted, as orientational effects on the water dipoles get weaker. An interesting feature of Figure 3-28 is that the slope $d\varepsilon_r/dz$ can take on both negative and positive values depending on the location. (ii) A second feature of Figure 3-28, relative to the previous curve of Figure 3-23, is the much higher value of ε_r near the z = 0 electrode surface. This again arises from the perturbative effects of the ions near the boundary. Strong Coulomb forces produced by the ions disturb the near-perfect orientation of water dipoles that could be set up by the external field. Consequently, the average dipole moment <M> is not quite as large, and based on equation 3.10, the resulting permittivity is not as small. Obviously, variations in the ion density can be expected to influence the degree of perturbation. As a result, magnitudes of the surface fields, permittivity, and eventually the breakdown strength can all be expected to be density dependent. Such an ion-density dependence of the breakdown voltage has recently been observed by our group. Finally, calculations of internal pressure for the water-ion system are shown in Figure 3-29.

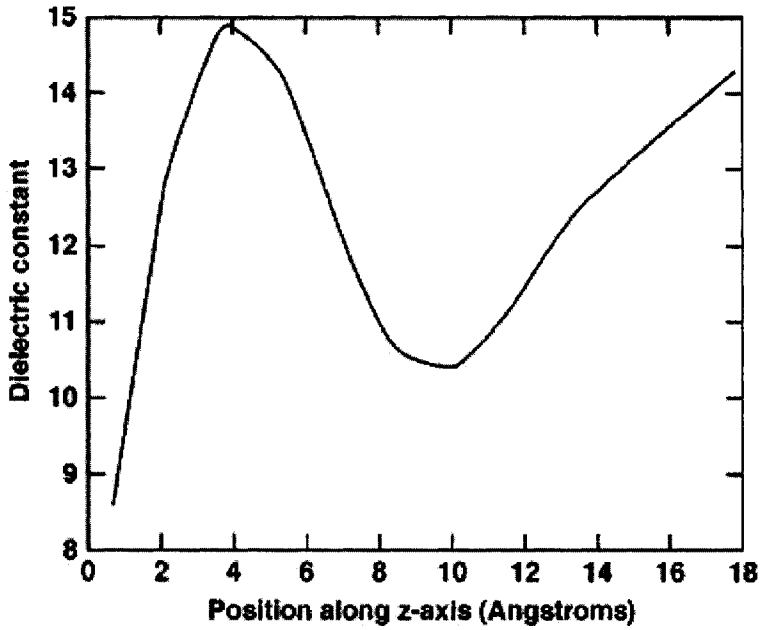

Figure 3-28. Spatial dependence of the dielectric function with Na^+ ions in water.

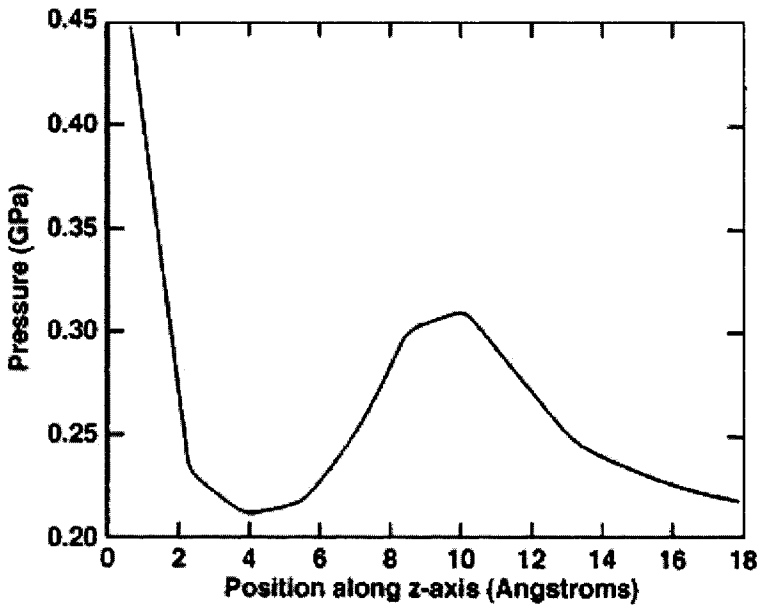

Figure 3-29. Results for the internal pressure with normal distance from the negative electrode for water containing Na^+ ions.

3.3.4 Summary and Conclusions

In conclusion, we analyzed the electrical double layer at the electrode-water interface for high voltage devices close to the breakdown point, based on a static, Monte Carlo approach. The primary goal was to attempt a better understanding of the inherent physics at the water-electrode interface, and its affects on high-voltage, electrical operation. The MC calculations carried out here attempt to address some of the open questions. These include the potential mechanism for breakdown initiation, assessing the fundamental limits on electric field stressing. While these issues remain to be studied in detail, our results demonstrate the possibility of strongly non-linear field-induced effects near the electrodes. This is a particularly important region, since a variety of features have been observed at high applied voltages near the electrodes.

It was shown that strong dipole re-alignment, ion-ion correlation, and finite size effects can greatly modify the electric fields and local permittivity at the electrode interface. The sharp increase in the surface electric fields with concomitant lowering of the dielectric constant, could lead to dramatic enhancements in Schottky injection at the contacts. This process could, therefore, be a source for initiating electronic controlled breakdown, and provide for carrier multiplication through impact ionization close to the metal surfaces. Due to electrode corrugation, as well as the finite-size effects of ions and molecules, a transverse dependence on the Schottky enhancement should exist. This would then be responsible for localized charge creation and streamer growth and propagation.

The Monte Carlo based calculations presented here also showed that large pressures associated with the Maxwell stress tensor would be created at the electrode boundaries. The pressure dependence on the electric field obtained here matched a

previous report that had been based on analytical, thermodynamic calculations [74]. It was demonstrated that the enhancement would depend on the background conductivity of liquid water, and is in keeping with observations of breakdown voltages that depend on bulk conductivity. The MC results also demonstrated that the Coulomb forces due to ions near the interface modify the dipole arrangement to produce local structure and striations in local permittivity. Though the lateral structure was not studied, it is implicit that some degree of transverse variations is also to be expected.

3.4 Percolative Model of Liquid Electrical Breakdown Process

3.4.1 Introduction

Percolation theory since its inception [75] has become a major statistical tool for interpreting and predicting morphological [76-78] and transport properties [79-82] of disordered media. Liquid electrical breakdown system is heterogeneous, consisting of dissolved gases, solutes and the existence of asperities at the contacts, and density fluctuations. This is known to affect injection at metal-liquid interfaces, and lead to the nucleation of streamers and "tree-like structures" at high-applied voltages [16]. The thermal expansion may also potentially lead to density gradients and form localized "bubbles"[83], growth and transport of internal bubbles that make the system characteristics dynamic, and result in instabilities at the vapor-liquid interfaces [18].

The electrical model here uses the stochastic concepts proposed by Niemeyer et al. [25]. Conduction is treated in terms of current flows through a network of resistors having random values and breakdown characteristics based on a specified statistical distribution. Failure of a constituent resistor element occurs if the local fields exceed a

critical threshold. Breakdown of the overall structure occurs if a "failure channel" percolates all the way from one electrode to the other.

3.4.2 Modeling Details

The simulation model is developed and implemented by considering a two-dimensional (2D) rectangular lattice in which the two sides (left and right) represent the electrodes. A 2D representation has been used for simplicity, but the approach can easily be extended for three-dimensional analysis as well. The approach relies on initially generating an array of random seed points within a rectangular simulation lattice.

Resistors, having random values are placed between every pair of seed points. Physically, the resistor values depend on the resistivity and geometric characteristics of each 2D polygon. The attributes of each resistive element can, in principle, be assigned based on material physics to include all details to the level desired. Hence, it becomes possible to include effects such as local density fluctuations arising from variable solute concentrations, the presence of bubbles, and fractional compositions of each component in case of mixtures such as oils, thermal effects, etc.

Here, the resistor magnitudes at the start of the simulation were assigned randomly based on a specified distribution function. For concreteness, a Gaussian DF has been used here with the mean $<R>$ and variance σ_R being user specified input parameters for the simulation. Thus, each resistor between pairs of seed points can be made identical to or different from the other, depending of the variance value specified (i.e. $\sigma_R \geq 0$.) The model configuration is shown in Figure 3-30.

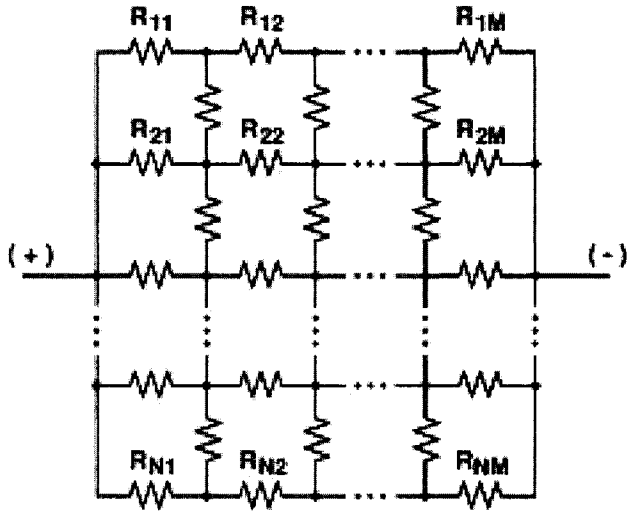

Figure 3-30. A simple rectangular lattice of resistors for uniformly distributed seed points.

Figure 3-30 depicts a simple rectangular lattice with uniformly distributed seed points. For an N × M rectangular geometry (M longitudinal and N transverse segments), the total number of resistors would be: 2*N*M – M – N +1. Dirichlet boundary conditions are applied to all nodes on each side. The Kirchhoff current equation (KCE) at each of the internal nodes (i.e. seed points) yields a set of coupled simultaneous equations that can be solved if the current-voltage (I-V) characteristic of each resistive element is specified. Here the following simple, non-linear I-V relationship was chosen to test the percolative model:

$$R(E) = R_{oi}, \quad \text{for } E < E_{crit}, \tag{3.11a}$$

$$\text{and,} \quad R(E) = R_{of}, \quad \text{for } E \geq E_{crit}, \tag{3.11b}$$

where, E is the local electric field within each resistor segment, E_{crit} the critical threshold electric field for breakdown, R_{oi} the initial random value assigned to the i^{th} resistive

segment based on the distributive function, and R_{of} the final value upon i^{th} local breakdown. Here, the magnitude of R_{of} was chosen to be 1 percent of the initial value. Thus, a relatively simple I-V nonlinearity was implemented to model a transition between a high resistance "current blocking" state to a low resistance "conducting" for $E \geq E_{crit}$. In principle, though, other more complicated non-linear I-V characteristics could easily be implemented.

In the present model, the following procedure has been implemented for determining the breakdown voltage (V_{br}) for a given network size. A relatively low trial voltage is used as the external biasing value. The internal node voltages and branch currents are then computed by solving the KCE. If the local electric field exceeds the critical value E_{crit} (assigned as an input parameter), the resistor values change in accordance to equation 3.11. Using the updated resistance network, a KCE solution is recomputed. The procedure repeats until a percolative path is established between the two electrodes, or no further transitions in the resistance occur at any of the elements for the applied bias. The value of the applied voltage sets V_{br} in the former case. In the latter situation, with an absence of a complete percolation channel, the biasing voltage is increased, and the above procedure repeated until an eventual a complete percolative path is achieved. It must be mentioned that the V_{br} value thus obtained for a given network array is not unique since it depends on the initial random selection of the R_{oi} value set. The uncertainty and statistical variation can be eliminated by repeating the full procedure numerous times, with different random-number seeds. This effectively yields multiple networks, each of which yields a breakdown value. Upon averaging, the mean $<V_{br}>$ value can be determined.

3.5 Improved 2D, Time-Dependent Network Model Based on Non-linear Conductance and Energy Thresholds

3.5.1 Introduction

In section 3.4, a simple percolative model was introduced. The local electrical conductance depends only on the electrical field in that primitive percolative model. Also, the primitive model does not include capacitive effects on the liquid electrical breakdown system. These two shortcomings were subsequently resolved in the current two-dimensional, time-dependent network model by incorporating an energy criteria for local breakdown, and using parallel capacitor to resistor to model the time-dependent properties in the liquid breakdown process. The modeling details are given in subsection 3.4.2.

3.5.2 Modeling Details

The simulation model is developed and implemented by considering a two-dimensional (2D) regular network in which the two sides (left and right) represent the electrodes. Each unit of this electrical network consists of a parallel resistor-capacitor combination whose attributes are based on the geometry and local parameters as shown in figure 3-31. The values can either be uniformly constant or assigned a random variation to account for local fluctuations. The use of a Gaussian distribution function with user specified mean values <R> and <C>, and variances σ_R, σ_C can provide for randomness.

Here, a point-plane electrode geometry that is commonly used in experimental work has been chosen for concreteness. Such an arrangement can create a large,

localized electric field at the tip for initiating the breakdown. This geometric arrangement can be modeled by dividing the region into $n \times m$ elements as shown in Figure 3-31. The narrow rectangles on the two sides of the model donate the positive and negative electrodes. Every line segment of the network shown in Figure 3-31 donates a single electrical elemental unit consisting of a parallel resistor-capacitor combination as shown in Figure 3-32. The total number of electrical units, N_T, in such a n × m network is: $N_T = 4 \times m \times n$. Assuming each element as a cubic unit of conductivity Φ, length L and area S, its resistance R per unit will be: $R = L/[\Phi S]$. This resistance R can vary in sections, and thus, be dissimilar for the various elements. The voltage assigned to each node is the unknown variable that can be obtained by solving the entire electrical network based on Kirchhoff's law.

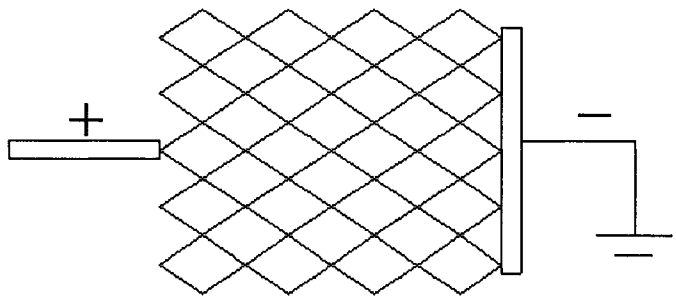

Figure 3-31. A 4 × 5 network representation for a point-plane geometry.

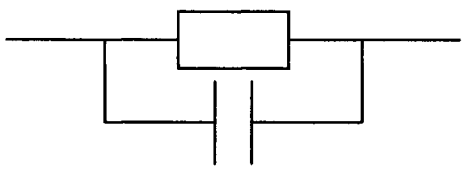

Figure 3-32. The elemental electrical unit representing the network in Figure 3-31.

Initially, R_{oi} the initial random value assigned to the i^{th} resistive segment based on the Gaussian distribution. A Gaussian distribution with mean value $\langle R \rangle = L/[\Phi S]$ and standard variation $*_R = c \langle R \rangle$, with $0 \leq c < 1$, has been used here. The following simple, non-linear I-V relationship has been chosen:

$$R(E) = R_{oi} , \quad \text{for } E < E_{threshold} , \tag{3.12a}$$

$$\text{and,} \quad R(E) = R_{of} , \quad \text{for } E \geq E_{threshold} , \tag{3.12b}$$

where E is the local electric field within each resistor segment, R_{of} the resistance prior to breakdown, and R_{of} the final value upon breakdown. Physically in this simple nonlinear model, the resistance drops dramatically upon breakdown from R_{oi} to R_{of}.

In the present case, two parallel criteria have been used for the water breakdown. The first criteria for breakdown is that the electric (E) field across the electrical element be higher than a threshold value $E_{threshold}$ (i.e., $E_{element} > E_{threshold}$). This E-field across each element can be computed since the simulation procedure continually provides the node voltages at each time step by simultaneously solving Kirchchoff equations (KCE). A second criteria is that the energy supplied by the local electrical element W_{sup} be higher than the latent heat W_{lat} of vaporization for the liquid. This condition is expressed as: $W_{sup} = [U_{element}^2/R_{element}])t$, where $U_{element}$ is the voltage drop across the element and t the simulation time step. The latent power W_{lat} necessary to vaporize the water can be obtained directly from the equation [84]:

$$W_{lat} = \Delta_o V [c(T_2 - T_1) + r] , \tag{3.13}$$

with $\Delta_o = 998$ kg m^{-3}, $c = 4.18 \times 10^3$ J kg^{-1} K^{-1}, $T_2 = 373$ ^{E}K, $T_1 = 293$ ^{E}K, and $r = 2256$ kJ kg^{-1}. If at any time step, an elemental segment meets both the above criteria for breakdown, then that corresponding element is set to a "breakdown state". Thus, in the present model, the following procedure has been implemented for determining the breakdown voltage (V_{br}) for a network of given size. Since the breakdown voltage is not known *a priori*, a relatively low trial voltage is used as the external bias to start the calculations. The resistor and capacitor values are initialized with a Gaussian distribution. The internal node voltages and branch currents are then computed by solving the KCE. If the local electric field exceeds the critical threshold and the energy dissipation is above the latent heat of vaporization, the elemental resistor and capacitor values change due to a breakdown event. Here, the magnitude of R_{of} has been chosen to be at least 10^{-3} percent of the initial value. In addition, elemental breakdown results in an alteration of the capacitance value. Physically, this is necessary since the vaporization-based streamer development causes the local dielectric constant to decrease from the liquid value.

Using the updated impedance network at each time step (with or without elemental breakdown), a Kirchhoff solution is recomputed. The procedure repeats until a percolative path is established between the two electrodes, or no further transitions in the elemental impedances occur with time anywhere for the applied bias. The value of the applied voltage sets V_{br} in the former case. In the latter situation, with an absence of a complete percolation channel, the biasing voltage is increased, and the above procedure repeated until an eventual a complete percolative path is achieved. As in the last section 3.4.2, it must be mentioned that the V_{br} value thus obtained for a given network array is

not unique due to the fluctuations in initial random selected R_{oi} value set. Repeating the full procedure numerous times, with different random-number seeds, eliminates the statistical variation. It might also be mentioned that due to the presence of a chosen electrical network, the streamer propagation in the present approach proceeds along pre-determined segments, and does not have completely random orientation.

3.6 Drift Diffusion Time-Dependent Physical Continuum Model

3.6.1 Introduction

The two models in section 3.4 and 3.5 gives a percolative approach to simulate the electrical breakdown process. And the random pattern of streamer is reflected in the percolative model. However, those two models didn't physically, quantitively explain the streamer process, such as polarity effect, conductance-related electron density distribution, positive ions distribution, and the role of bubble in the system.

In section 3.6.2, the qualitative features in liquid electrical breakdown were discussed, including the polarity effect, an important feature in the liquid electrical breakdown experiments. And the numerical implementation was carried out in the section 3.6.3 based on the qualitative features.

3.6.2 Qualitative features

3.6.2.1 General model discussion

Here a general model of liquid breakdown is developed that incorporates two important features and overcomes the short-comings of the percolative models. The percolative models essentially invoke energy and/or electric field thresholds that are

qualitative at best, and lack any rigorous quantitative determination. Hence, though the percolative model captures the essential physical trend, it lacks rigor and is not a first-principles calculation. The continuum, fluid model presented here attempts to overcome this drawback, and includes a few additional features. The continuum model implicitly assumes the *pre-existence of spatially localized micro-bubbles*, in equilibrium with the liquid phase. As a result, no strong internal heating or vaporization is necessary for the creation of local low-density regions. Such bubbles are assumed to be filled with dissolved gas. Next, in keeping with experimental reports (as discussed for example, in the case of water [84]), it is assumed that free electrons are generally absent in liquids. Instead, more realistically, the experimental observations indicate that free electrons have a short and finite lifetime before an attachment or recombination event takes place. Consequently, the likelihood of electrons survival can be expected to progressively decrease with increasing distance from their generation sites.

In this model, liquid breakdown is initiated via the field-emission process within localized, low-density regions (i.e., micro-bubbles) upon being subjected to high electric fields. The possible existence of stable microscopic gas bubbles within liquids was first proposed by Bunkin et al. [85]. They referred to such entities as "bubbstons". Bunkin et al. [85] studied the formation and stabilization dynamics, and concluded that bubbstons could exist in the presence of trace impurities (including ionogenic surface-active agents) and localized ions. Such micro-bubbles are likely to be randomly scattered throughout the bulk of the liquid volume, and also be present at electrode surfaces.

Discontinuity in the dielectric constant between the surrounding liquid and the interior of the bubble helps create electric field enhancements on the gaseous side of the

micro-bubble interface. Electrons are then injected into the gas bubble via the field-emission process at the bubble-liquid interface. Subsequent acceleration by the electric field within the bubble leads to strong energy gain and impact ionization of the bubble gas. Thus, *micro-bubbles act as localized micro-sources of charge*, and contribute to plasma creation and multiplication within the liquid. The sudden and discrete increases in the external current observed experimentally are then the result of individual bubbles that develop into active micro-centers of charge creation.

The following effects should then arise due to the collective influences of a large electrostatic driving force on the electrons, the inherent scattering with gas molecules and subsequent impact ionization events.

(i) Sudden and discrete increases in the external current as individual bubbles develop into active micro-centers of charge creation. Such current spikes, as predicted by the present model, have actually been observed experimentally. In time, however, the electric field within each micro-bubble would be expected to diminish as the result of charge-induced, intra-bubble polarization. This would partially quench the current contribution from an individual "electrically activated" micro-bubble. The net result would be multiple, but sporadic, current spikes.

(ii) A second effect is the possible emission of radiation encompassing the micro-bubbles. A combination of processes, such as field-induced acceleration, Coulomb scattering of the charges, and radiative recombination would collectively contribute. Such localized pockets of radiation and optical

emission have been observed, with the results of Figure 3-33 being an illustrative example. Apart from frequency dependent Bremsstrahlung, the emission spectra can also be expected to contain lines characteristic of gaseous excitation and absorption. In addition, radiative recombination of electrons (moving downstream towards the anode), with ions generated originally from a neighboring micro-bubble would also be present.

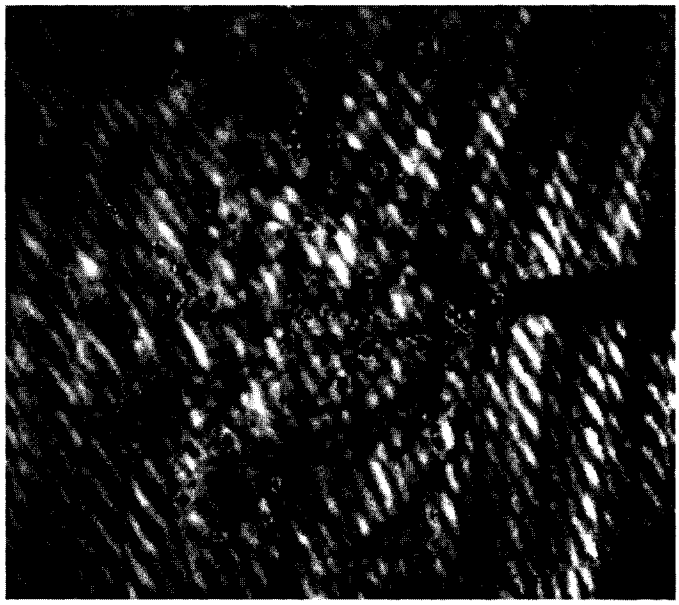

Figure 3-33. Experimentally obtained luminosity spots at discrete locations on the streamer branches during a pre-breakdown snapshot for oil. (Figure from private communication).

(iii) The present model predicts an effect of both the external pressure and operating temperature, on the breakdown voltage magnitude. With increasing external operating pressure, for example, the micro-bubble size would decrease. This would lead to a larger field requirement for producing a given amount of charge multiplication within the confined space. Similarly, increases in temperature could reduce the micro-bubble density due to their evaporation from the liquid phase. Consequently, the probability of a micro-

bubble lying within a localized high-field region would diminish. This would lead to an overall increase in the requisite field, or a longer delay time for breakdown. Such changes with pressure have been observed in our group, for example, as shown in Figure 3-34. If, however, the bubble population remained stable despite temperature variations (for example, due to large fluid viscosity that prevented bubble movement and evaporation), then their size would change. This would alter the charge multiplication factor within the micro-bubble volume, and again impact the breakdown field. However, for most liquids of practical interest, this is unlikely.

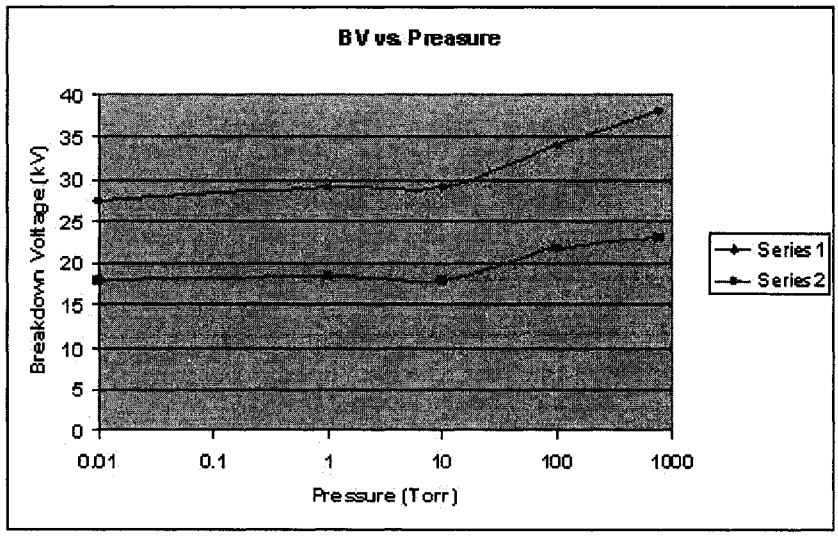

Figure 3-34. Experimental data showing a pressure dependence of the breakdown voltage for oil. (Figure is from private communication).

(iv) In the scenario described here, the breakdown process would likely initiate in a region of high electric field that promotes electron emission. This would most likely be on the gaseous side of a micro-bubble-liquid interface, and occur close to an electrode. Surface asperities and sharp curvatures would

strongly facilitate this initiation. Hence, smoothening the electrodes should enhance the hold-off voltage capability. Furthermore, the presence of a strong ion density would work to mitigate the electric field magnitude, and arrest its penetrating into the micro-bubble areas. As a result, an influence of ionic concentration on the breakdown threshold voltage can be expected.

(v) In this setting, micro-bubbles would continue to play a role in the temporal development of the breakdown process. For example, if multiple micro-bubbles were to be located along a straight-line path between the initial triggering point and the electrodes, then bifurcation of the plasma channel can be expected. Through the process of successive and sequential breakdown of micro-bubbles, the breakdown path might be expected to zigzag, hopping from one bubble to the next. Such branching or "treeing" structures, have experimentally been observed by numerous groups. Another physical basis for the branching might arise from mutual electrostatic repulsion between high-density pockets of spatially non-uniform electrons within the moving streamer. Such a mechanism has recently been proposed in gases [86], but remains to be investigated in liquids.

In our proposed model, streamer (or plasma) growth and propagation within the liquid primarily depends on the three following factors. (i) The ionization rate within micro-bubbles, which is governed by the bubble radius and local electric field. This rate dictates plasma generation, that then controls the dynamical collapse of the local electric field due to internal polarization effects. We propose that the collapse would trigger field

increases across neighboring regions and micro-bubbles that, in turn, would initiate new, localized plasma generation events. Thus, higher the ionization rate within micro-bubbles, the faster would be the conductive turn-on of localized segments within the overall liquid. (ii) The growth of the streamers would also depend on the magnitude and rate of energy dissipation by hot electrons emerging from the micro-bubbles. Electronic kinetic energies and effective temperatures are expected to be quite large due to strong electric field acceleration within the micro-bubbles. For example, a ballistic electron under a 10^8 V/m field (the typical value close to the breakdown regime) within a 1-micron diameter bubble would emerge with a 100 eV energy, as shown in subsection 3.2.4. Upon expulsion from the micro-bubble, such energetic electrons would convert their kinetic energy into heat through inelastic collisions with the water molecules, and thus impact-ionize localized regions. The net result could be large increases in local temperature and possible vaporization of small volumes adjacent to the micro-bubbles. The latter would cause a growth and elongation of the micro-bubble along the field direction. Exact analysis of streamer growth based on such thermal conversion of electron energy requires Monte Carlo calculations in subsection 3.2.4. (iii) A secondary effect is that of possible electron injection from the cathode after filamentary structures have developed from the anode. For breakdown initiation from the anode side, the electric field in the anodic vicinity would gradually decrease, giving rise to field enhancements at the cathode neighborhood. Electronic field emission from the cathode could then lead to the origination and growth of *secondary steamers* from the negative electrode. This effect should squeeze out the high resistivity region lying between the two opposing filaments, and increase the electric fields dynamically across this

"unbroken" segment. Such dual filamentary structures, with time-dependent propagation velocities have recently been reported at Sandia National Laboratory [35]. Also, in such dual filament structures (with the initial breakdown occurring at the anode), the streamer propagation velocities would be high, and increase dramatically in time after the development of the second streamer. The schematic process of liquid electrical breakdown model is shown in Figure 3-35.

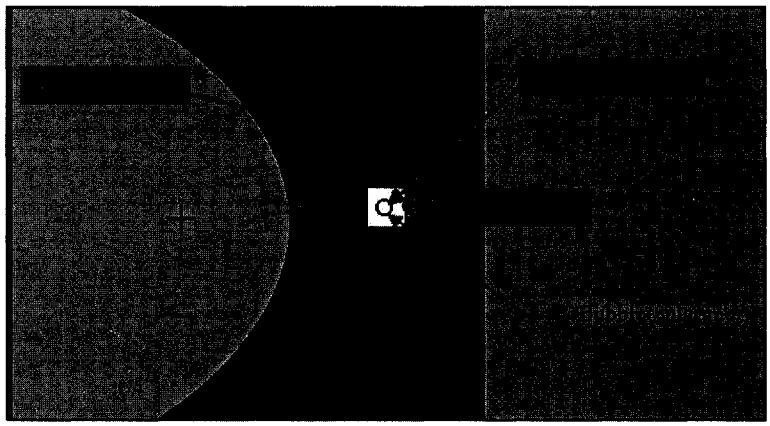

Figure 3-35. Schematic figure of liquid electrical breakdown model.

3.6.2.2 Discussion of Polarity Disparity in Point-Plane Liquid Electrical Breakdown

Given the random location of the micro-bubbles one might expect breakdown to be triggered at either the cathode-end or the anode-end with equal probability. For asymmetric point-plane geometries, the initiation might be expected to have a greater likelihood at the sharper electrode. *Yet, experimental data is universally indicative of a strong anode-side preference.* This, and the other features listed in the previous section, can be understood based on differences in the dynamics following initial charge creation. For initiation within a micro-bubble close to the anode, electrons quickly move towards

the anode for collection. In the process, the local resistivity of the bubble-anode path is obviously reduced. The slow ions, moving in the opposite direction, do not exhibit appreciable displacement and cluster close to their formation volume. Their excursion into the bulk liquid is slow and minimal. The associated charge polarization produces a net electric field collapse at the micro-bubble site, while enhancing the field intensity in the bulk. The induced field enhancement over the bubble-to-cathode segment, (especially the micro-bubble neighborhood), is relatively strong due to the high density of the tightly bunched, slow-moving ions.

On the other hand, for initiation close to the cathode, electrons begin to spread out more easily into the bulk liquid. Both mutual electrostatic repulsion and a higher diffusion and mobility contribute to a strong movement of the lighter mass electronic swarm. The net effect is that the locally created charge density becomes somewhat more dilute in the bulk region. The spatial electric field pattern further assists in the dilution. External electric fields near a micro-bubble located near a sharply curved cathode (e.g., needle geometry), are highly divergent looking into the liquid bulk. This non-uniform field pattern accentuates the electron density dilution as their population emerges from the micro-bubble and begins diverging into the bulk. Though a similar divergent field pattern would exist at micro-bubble sites near a sharply curved anode, it's effect in driving the heavy and slow ions would be minimal. In summary then, the charge density magnitude in the immediate vicinity of a micro-bubble, following an initial triggering event can be expected to be quite disparate. Anode-side triggering would produce a much larger charge density in the bulk neighborhood close to the initiation point. The induced electric field, created by the presence of this generated carrier density, would

therefore, be *larger for anode-side triggering.*

In our model of liquid breakdown, field emission (i.e., field-assisted electron tunneling) from the water molecules is an important non-linear process that contributes to charge creation and plasma generation. This leads to two important consequences: (i) A natural positive feedback mechanism between charge creation and the locally induced electric field can be created fairly quickly. For example, perturbative increases in the local field can cause large enhancements in ionization rates due to the exponential inter-relationship. This, in turn, leads to strong localized increases in the density of generated charge pairs. Thus, a localized "breakdown" event can quickly occur. Upon subsequent charge movement and separation, the electric field induced by the generated charge is further increased downstream, close to the micro-source. (ii) As already discussed, disparities in mobility between electrons and ions cause the induced electric fields to be somewhat different for anode-side and cathode-side triggered events. The above positive feedback mechanism accentuates this difference. The net result is that perturbative fluctuations or localized triggering is more likely to develop into an ionization wave for micro-bubbles located near a sharply curved anode given the higher spatial accumulation of the sluggish ions.

A number of interesting features naturally follow from the above discussion. (i) The critical electric field necessary for generating an ionization wave or streamer will be relatively lower for an anode-side triggering event. This difference in breakdown threshold voltage has been observed experimentally, and gives rise to a cathode-directed streamer. (ii) Such a cathode-directed streamer would tend to have lower transverse dimensions as the spreading (due to both drift and diffusion) of generated charge would

be less. This agrees with experiments that show streamers originating from the cathode (i.e. anode-directed formations) have a thicker root and larger radial size. (iii) The positive (i.e., cathode-directed) streamer should have a higher velocity of propagation, since the local electric fields at the advancing wave front would be higher. The higher electric fields facilitate faster ionization due to both the exponential nature of the field-emission processes, and a higher carrier drift velocity. The former is more important due to its non-linearity. The larger charge creation leads to greater localized field quenching in time, and a higher field enhancement downstream. In this scenario, the streamer propagation is not dictated by the drift of the charges, but rather by the speed of field-assisted ionization of successive elements. (iv) The charge dilution effect already discussed in the context of cathode-side breakdown, not only leads to a higher threshold electric field, but also requires more time for the breakdown development. This feature is in keeping with experiments [87]. *In cases where both anode-side and cathode-side filaments have been seen [35], the latter was always to form later in time.* (v) Finally, it follows that the luminescence signal characteristics should also be different between cathode- and anode-directed streamers. For example, in positive (cathode-directed) streamers, electrons are continually being generated at the streamer tip (i.e., the highest electric field region). These electrons travel back into the filamentary segment. This segment has an ion density, since ions created at earlier times have not been able to exit the streamer body. This failure to completely be flushed out of the streamer body arises from the low ion mobility, and the localized collapse of the electric field within the filamentary region. This availability of ions facilitates radiative recombination of the inward-moving, newly-generated electrons. Thus, the luminosity of the positive streamer

tends to be higher. For negative (anode-directed) streamers, on the other hand, the newly generated electrons are continually driven into the bulk and away from the streamer head. The availability of positive ions is much lower in this region. Hence, a much weaker radiative recombination intensity will result. Their spectral component should have a stronger component from the Bremsstrahlung process. Such optical disparities have been observed.

3.6.3 Numerical Implementation

The flux corrected transport (FCT) approach [88-90] developed by Boris and Book, and later generalized by Zalesak [91], was used for numerical implementations of our liquid breakdown model. This is a continuum model based on fluid equations and was coupled to a Poisson solver. FCT schemes have been successfully used in the past for breakdown analysis since they accurately treat the sharp gradients and large dynamic range encountered at streamer surfaces [92-95]. In most situations for which the mass/charge density gradient and the velocity variations are smooth and small, conventional approaches such as the Lax-Wendroff [96] or the leap-frog [97] schemes treat the continuity equations quite adequately. However, for problems involving streamers, ionizing waves [98, 99], shock waves, or regions of strong sources and sinks, the conventional techniques can generate substantial short-wavelength errors. Numerical errors due to sharp gradients can artificially distort the induced electric field predictions. The non-linear relationship between the electric field and ionization can then further exacerbate the errors in time. In our model, the 2D FCT algorithm is used. The basic steps of a one-dimensional (1D) FCT algorithm are as follows, taken from the original paper by Steven T. Zalesak [91].

Step 1: The basic equation connecting the carrier density ρ and its velocity v is :

$$\frac{\partial \rho}{\partial t} = \frac{\partial(\rho \cdot v)}{\partial x}, \tag{3.14a}$$

where t is time, and x is the distance.

Step2: 1st order flux approximation $F^L_{i+(1/2)}$ with $v_{i+(1/2)}$, as shown in figure 3-36 is:

$$F^L_{i+(1/2)} = \begin{cases} v_{i+(1/2)} \cdot \rho_i & if \quad v_{i+(1/2)} \geq 0 \\ v_{i+(1/2)} \cdot \rho_{i+1} & if \quad v_{i+(1/2)} < 0 \end{cases} . \tag{3.14b}$$

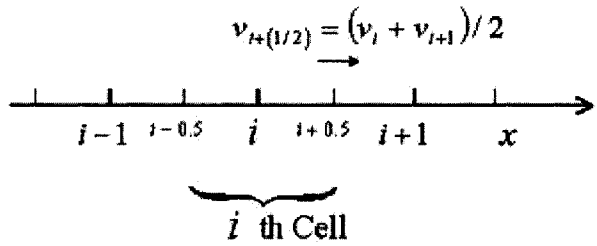

Figure 3-36. Description of $v_{i+(1/2)}$ in 1D case.

Step3: Higher order flux approximation: Leapfrog-trapezoidal method is used to calculate higher order flux, for example, here it is the 4th order flux calculation:

Step3.1:

$$F^t_{i+1/2} = \frac{7}{12}\left(v_i \rho^t_i + v_{i+1}\rho^t_{i+1}\right) - \frac{1}{12}\left(v_{i+2}\rho^t_{i+2} + v_{i-1}\rho^t_{i-1}\right) . \tag{3.14c}$$

Step 3.2 (Leap-frog algorithm):

$$\rho_i' = \rho_i^{t-\Delta t} - 2\Delta t \cdot \Delta x_i^{-1} \cdot \left[F^t_{i+1/2} - F^t_{i-1/2}\right] . \tag{3.14d}$$

Step 3.3: (the trapezoidal algorithm)

$$\rho_i^* = \left(\rho_i^t + \rho_i'\right)/2 \quad . \tag{3.14e}$$

Step 3.4:

$$F_{i+1/2}^H = \frac{7}{12}\left(v_i\rho_i^* + v_{i+1}\rho_{i+1}^*\right) - \frac{1}{12}\left(v_{i+2}\rho_{i+2}^* + v_{i-1}\rho_{i-1}^*\right) \quad . \tag{3.14f}$$

Step 4: After finishing the low and high order flux calculations, the solution is obtained as:

Step 4.1:

$$\rho_i^{td} = \rho_i^t - \Delta t \cdot \Delta x^{-1} \cdot \left(F_{i+1/2}^L - F_{i-1/2}^L\right) \quad . \tag{3.14g}$$

Step 3.2:

$$A_{i+1/2}^C = C_{i+1/2} \cdot \left(F_{i+1/2}^H - F_{i+1/2}^L\right),\ 0 \le C_{i+1/2} \le 1 \quad . \tag{3.14h}$$

Next, one picks up the $C_{i+1/2}$, so that no new minimum and maximum is created. The details are given in reference [91].

Step 3.3:

$$\rho_i^{t+\Delta t} = \rho_i^{td} - \Delta t \cdot \Delta x^{-1} \cdot \left(A_{i+1/2}^C - A_{i-1/2}^C\right) \quad . \tag{3.14i}$$

Here a time-dependent, two-dimensional fluid model based on the continuity equations for negative ions, positive ions, and electrons, has been used. The Poisson solver was included for self-consistency. An external circuit was included by taking account of a 50 Ohm external resistor and a time dependent supply voltage $V_{app}(t)$. A uniform mesh was used to divide the entire device simulation region into equal sized

boxes. Transport was characterized on the drift-diffusion (DD) theory, and the ion densities updated within each box. Changes due to charge inflows and outflows, bulk recombination and generation, charge creation due to field emission and impact ionization within micro-bubbles, negative ion generation at the cathode due to electron tunneling into the liquid, positive ion decay at the anode due to electron capture via the tunneling process, and positive ion annihilation at the cathode via electron transfer, were all taken into account. The liquid was assumed to be free of impurities, and to contain only the H^+ and OH^- ions. The ionic mobilities, taken from Light and Licht [46], were $3.5 \times 10^{-7}\ m^2 V^{-1}s^{-1}$ for H^+ and $2x10^{-7}\ m^2 V^{-1}s^{-1}$ for OH^-. Free electrons generated within the micro-bubble were considered, and assigned a field dependent drift velocity v(E) given by: $v(F) = v_s \{E/[E+E_s]\}$, with E the electric field, v_s a saturation velocity taken to be 3×10^5 m/s, and $E_s = 3 \times 10^5$ V/m. Free electrons in liquid water were taken to have a lifetime of 200 ns. Current continuity was used to update the internal electric field E(x,t) and the potential at grid points within the center of each box, through the relation: $J_{cct}(t) = [V_{app}(t)–V_{Dev}(t)]/R = d[\varepsilon(E)\ E(x,t)]/dt+\sigma E(x,t)$, with V_{Dev} being the device voltage, and $\varepsilon(E)$ the field-dependent permittivity.

The following mathematical equations characterize the dynamical evolution of the system. For electrons, negative ions, positive ions in the bulk liquid, the continuity relations are:

$$\frac{\partial n_e}{\partial t} + \nabla \cdot (n_e \cdot v_e) - D_e \nabla^2 n_e = G_I - k_{c1} n_e n_p - \frac{n_e}{\tau_e}, \tag{3.15a}$$

$$\frac{\partial n_n}{\partial t} + \nabla \cdot (n_n \cdot v_n) - D_n \nabla^2 n_n = -k_{c2} n_n n_p + \frac{n_e}{\tau_e}, \tag{3.15b}$$

$$\frac{\partial n_p}{\partial t} + \nabla \cdot \left(n_p \cdot v_p\right) - D_p \nabla^2 n_p = G_I - k_{c1} n_e n_p - k_{c2} n_n n_p, \qquad (3.15c)$$

where n_e, n_n, n_p are the densities of electrons, negative ions and positive ions, while v_e, v_n, v_p are the corresponding drift velocities. The diffusion coefficients for the electrons, negative ions and positive ions are denoted by D_e, D_n, D_p. In the above equation 3.15, k_{c1}, k_{c2} are the recombination coefficients for the electron-ion and ion-ion processes. Finally, τ_e is the electron lifetime for attachment with a neutral water molecule, and G_I is the field ionization rate inside the liquid. This field ionization rate G_I is strongly field-dependent, and given as [100, 101]:

$$G_I = [(q\ E\ a) / h] \exp[-(m\ a\ \pi^2\ \Delta^2)/ (q\ E\ h^2)] \ , \qquad (3.15d)$$

where h is Planck's constant, "a" is the molecular separation (~0.31 nm for water at normal densities), q the electronic charge magnitude, and Δ the ionization energy barrier for water taken to be 4 eV [102]. The electron lifetime (ι_e) was taken to be 200 ns based on experimental reports [103, 104]. The recombination coefficients k_{c1}, k_{c2} were taken to be 10^{-19} $m^3 s^{-1}$ based on literature [14].

The relevant continuity equation for electrons inside the micro-bubble is:

$$\frac{\partial n_e}{\partial t} + \nabla \cdot \left(n_e \cdot v_e\right) - D_e \nabla^2 n_e = \alpha n_e |v_e| - k_c n_e n_p - \frac{n_e}{\tau_e} \ , \qquad (3.16a)$$

where α is the a field-dependent impact ionization coefficient. The above equation can be simplified for a variety of reasons. First, the micro-bubble size is fairly small (~ 1 μm radius) with high electric fields inside. This imparts high electronic drift velocities, and dramatically curtails the electron durations inside a micro-bubble. Consequently, the recombinative decay process can be ignored. Furthermore, based on the dielectric discontinuity at the bubble-liquid interface and resulting image configuration [105], charges cannot enter the bubble from the liquid. This eliminates some of the fluxes, and the following simplified equation results for electrons:

$$\frac{\partial n_e}{\partial t} = -n_e \cdot |v_e| + \alpha n_e |v_e| \quad . \tag{3.16b}$$

Similar considerations apply to the ions within the bubble. Here, the impact ionization coefficient α(E) was taken to equal:

$$\alpha(E) = \alpha_0 \times \exp\left(\frac{-b_n}{E}\right) \quad , \tag{3.16c}$$

with $\alpha_0 = 5 \times 10^6 m^{-1}$ and $b_n = 2 \times 10^7 V/m$. The values arise from curve fits to raw Monte Carlo data, as explained in subsection 3.2.4. Finally, the space-charge field E_{ep} is controlled by the Poisson equation, and given as:

$$\nabla E_{sp} = \frac{q}{\varepsilon}\left(n_p - n_e - n_n\right) \quad . \tag{3.16d}$$

The total electric field was obtained by adding the E_{ep} above to the external field created by the applied voltage $V_{app}(t)$. Gauss's law was used to evaluate the external field by taking account of the charges at the two electrodes. Charge variations at the metal electrode at each time step were determined from the conduction current. Account was taken of the electronic transitions from liquid to the metallic anode, and the field-dependent injection. The transition probabilities were computed based on the Wigner-Kramers-Brillouin (WKB) approximation [106]. The details have been reported by our group elsewhere [107].

In the present calculations, an effective field dependent permittivity was used based on a detailed atomic-level analysis of the electrical response of water dipoles at the metal-liquid interface in section 3.3. This effectively leads to electric field enhancements arising from a positive feedback mechanism, since permittivity decreases with increasing electric field. The cross-sectional geometry was assumed to be rectangular, with a 200 μm distance between the point and plane electrodes in keeping with the experimental setup within our group [107].

3.7 Summary of the Important Modeling Features

Systematically, the nanosecond liquid electrical breakdown system properties were studied based on our modeling and calculation, including the temperature profile (subsection 3.2.2), double layer electrical field enhancement formed between electrode and liquid (subsection 3.2.3), electron behavior in liquid and inside micrometer gas bubble (subsection 3.2.4 and 3.2.5), liquid water physical properties under the high electrical field (section 3.3).

The analyses basically answered the following questions and aspects: (A) Electrical energy in the nanosecond electrical breakdown system was shown not to be sufficient to vaporize the normal liquids (e.g. water in the present case). Hence, thermally stimulated electrical breakdown seems quite unlikely (subsection 3.2.1). (B) A strong electrical field enhancement was shown to be possible due to collective dipole alignment effects. This is likely to occur close to the electrodes, and even at the interface between the liquid and a possible micro-bubble (subsection 3.2.2). (C) It was shown that electrons could not easily impact ionize liquid water molecule under the typical electrical field applied. The strong isotropic scattering at the lower energies was responsible for this outcome. Instead, it was shown that electron impact ionization inside micron-sized bubbles would contribute to electrical breakdown (subsection 3.2.2 and 3.2.3). (D) It was also shown that dielectric constant of liquid water is strongly field dependent, and that its value would be a monotonic decreasing function of the electrical field (section 3.3). This trend has been borne out in experiments, and would help accentuate the liquid electrical breakdown. (E) Two percolative models were also discussed and used to simulate the streamer random pattern and other properties in liquid electrical breakdown (section 3.4 and 3.5).

Following the various analyses mentioned above, the physical drift-diffusion micro-bubble based model was introduced (section 3.6). This is the most important model of this dissertation research. It is proposed that breakdown is initiated by field emission at the interface of pre-existing micro-bubbles. Impact ionization within the micro-bubble gas then contributes to plasma streamer development. Based on the drift-diffusion model, the entire breakdown process and its initiation can be adequately explained. Many of the

observed experimental details (such as the polarity effect) are predicted by this model. Simulation results, detailed discussion and relevant analyses are comprehensively presented in the next chapter.

CHAPTER IV

SIMULATION RESULTS AND DISCUSSION

4.1 Introduction

Some relevant and selected simulations results, together with analysis and discussion, are given in this chapter. The modeling was carried out on the basis of the three liquid electrical breakdown models discussed in the last chapter (section 3.4, 3.5, and 3.6). The simulation results and discussion relating to the primitive percolative 2D model of section 3.4 are presented in section 4.2. Simulation results of the improved percolative 2D network-based model discussed in section 3.5 have been given in Section 4.3. Finally, based on the drift-diffusion physical model, the most important model in this dissertation, simulation results for positive streamer generation and propagation are given in section 4.4. Here, a positive streamer is defined as a filamentary plasma channel that forms at the sharp, positively biased electrode in a point-plane configuration. Results for the negative streamer case and discussions concerning polarity effects (i.e., differences between positive and negative streamers) are presented in the section 4.5. This is followed by a summary in section 4.6.

4.2 Simulation Results and Discussion of Primitive Percolative Model

4.2.1 Simulation Results of the Liquid Electrical Breakdown Process

Simulations for liquid electrical breakdown were carried out based on the model outlined in the section 3.4. The value of E_{crit} for local piece failure was set to 2×10^5 Vcm^{-1} in keeping with experimental reports on breakdown in some liquids, while σ_R

(standard variation in Gaussian distribution) was retained as an adjustable parameter. Simulation results showing the evolution of breakdown and the systematic development of a percolation cluster are shown in Figure 4-1 for a 40 × 40 network with <R> = 5000 Ohms. The total physical dimension for the network on each side was taken to be 3 centimeters. Thus, under ideal conditions (i.e. identical segments), a breakdown voltage of $3 \times 2 \times 10^5 = 0.6$ MV is expected. However, in the presence of internal inhomogeneities, one expects the overall breakdown voltage to be lower since percolation via a connected path of least resistance can conceivably form. A similar logic lies behind the well-known reductions in overall "strength of chains" containing non-uniform elements, based on the weakest internal links. Here, two σ_R values of 50 Ohms and 250 Ohms were used to probe the impact of non-uniformities within the constituent resistors on the overall breakdown strength. The results yielded a breakdown voltage of 0.545 MV for σ_R = 250 Ohms, and 0.588 MV for the σ_R = 50 case. For the σ_R = 250 Ohms simulation, shown in Figures 4-1(a)-(d), the initial segment with co-ordinates around (5,30) is the first to breakdown. This is followed by a solitary increase to the left, a branching around this section, the development of other scattered breakdown sections, and finally a percolation with many failures on the right side. Results for the σ_R = 50 Ohms case, shown in Figures. 4-1(e)-(f), exhibit a similar breakdown pattern and the occurrence of random trees. Thus, these simulations demonstrate two important aspects. First, breakdown involves the development of filamentary trees with associated random structure, followed by an eventual percolative path. Second, there is an inherent reduction in breakdown strength with increases in the internal non-uniformity, as manifested through a σ_R higher value.

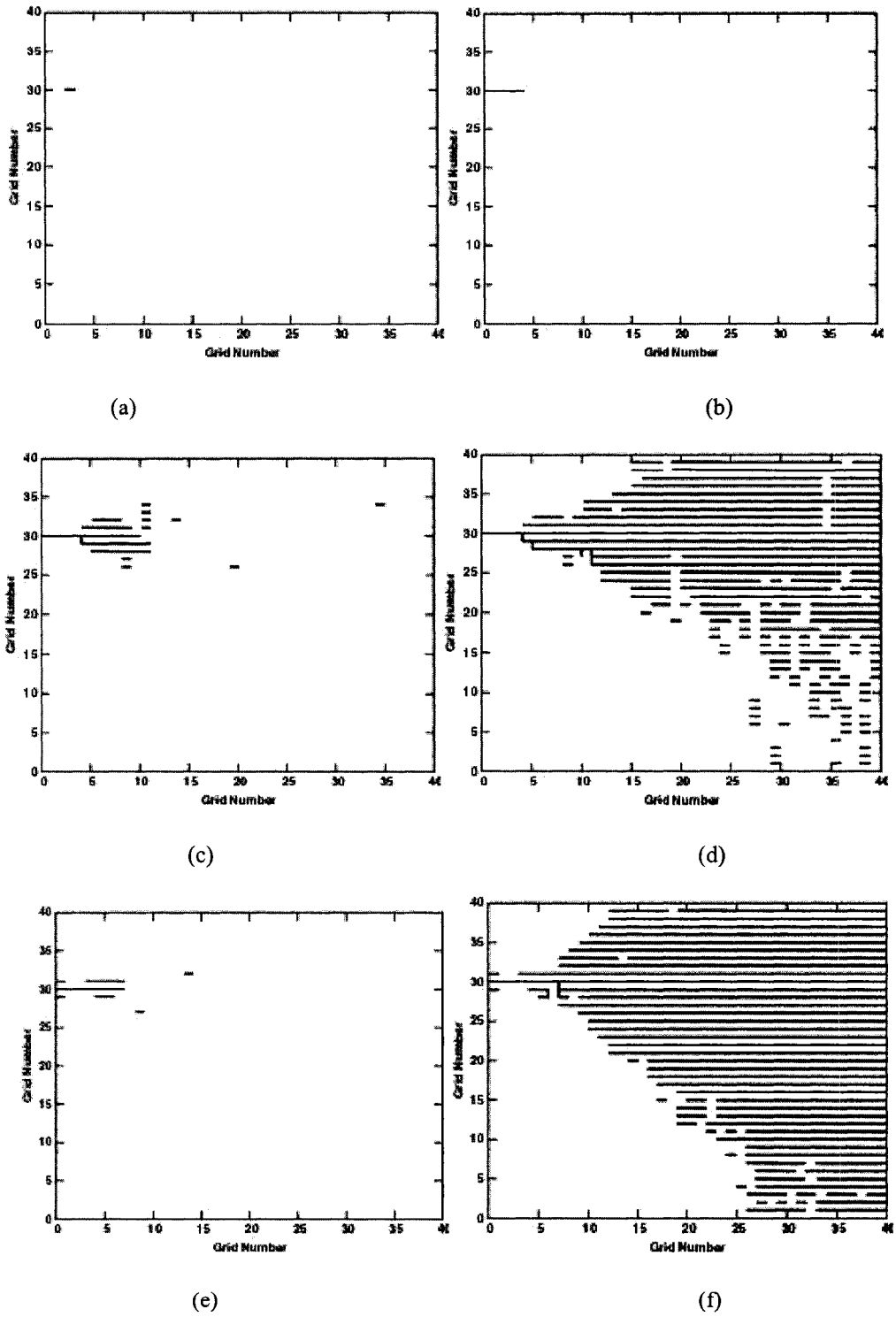

Figure 4-1. Breakdown evolution examples for a 40 × 40 network with <R> = 5k Ohms. (a)-(d) Different network states from intact to percolative breakdown for σ_R = 250 Ohms, and (e)-(f) the various network states for σ_R = 50 Ohms.

4.2.2 Analysis of the Effect of the Resistor Variance and Scaling

The dependence of breakdown voltage on the variance of resistor elements was simulated. The results obtained for a 40 × 40 network are given in Figure 4-2. Three points are evident from the figure. (i) First, the breakdown voltage decreases monotonically as the internal non-uniformity (i.e. σ_R) is increased. (ii) The variation and error range increases with σ_R. This is expected since the variability in possible resistances associated with the electrical network increases, and so do the inherent fluctuations. (iii) An extrapolation of the mean V_{br} values tends to the maximum theoretical value of 0.6 MV in the σ_R –> 0 limit. The plot clearly demonstrates that in practical situations, the presence of strong local inhomogeneity (such as a bubble, the presence of localized laser excitation, or solute/solvent clusters) would work to dramatically lower the overall breakdown capability of the liquid dielectric. This is in keeping with experimental observations.

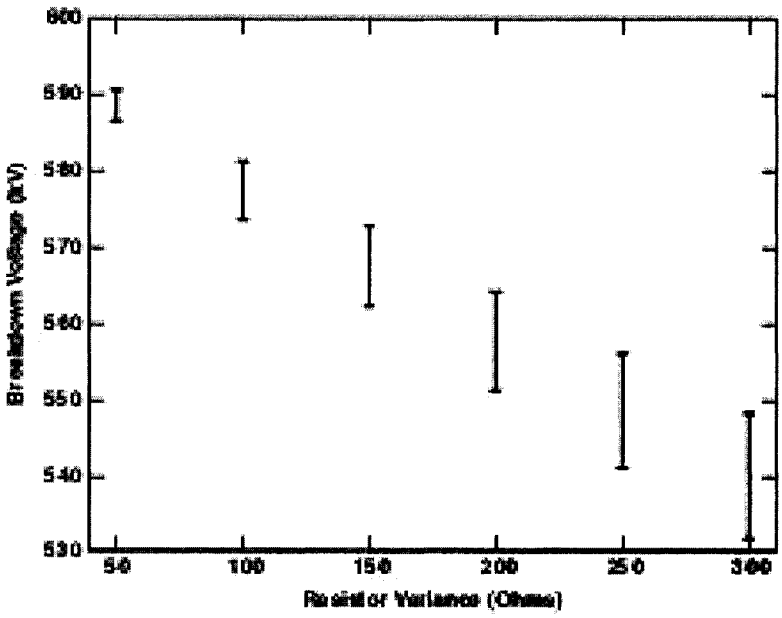

Figure 4-2. Dependence of the breakdown voltage on the resistor variance.

Another practical feature of interest in systems containing internal non-uniform segments is its scaling behavior. For a given mean resistance, σ_R value, and E_{crit} , the network is most likely to fail or breakdown when the distance between electrodes is the shortest. This is expected under such conditions, because of a higher probability of forming a percolation path connecting elements of least resistance. With increasing physical separation, the likelihood of a continuous connected channel at a given external bias decreases, and so the hold-off voltage can be expected to increase. The results of Figure 4-3 bring out this feature more quantitatively. Shown in Figure 4-3 are the mean V_{br} values obtained from the simulation for different network lengths and σ_R = 100. Network sizes ranging from 10x10 to 40x40 were used, with a fixed primitive unit of 0.1 cm. Numerous random seeds were used for each N × N network to obtain the average V_{br} value. A nearly linear scaling (for constant σ_R) of the hold-off voltage with the distance between electrodes is apparent. This trend is in keeping with the known behavior for σ_R = 0, and clearly validates the current approach. It must be mentioned, however, that the linearity obtained here is partly a result of the simplified I-V characteristics chosen. Physically though, variability in E_{crit} is not generally expected, except is cases of heterogeneous mixtures. Another scaling characteristic, in this context, is the behavior of V_{br} on the feature size of the constituent elemental resistances. In the simulations of Figure 4-3, an elemental unit length of 0.1 cm was used, while the earlier simulations for the 40 × 40 networks of total length 3 cm had equal segments of 0.075 cm (=3 cm/40) each. Physically, this elemental unit, Δ, represents the characteristic length scale over which the resistor values (or conduction characteristics of the liquid) fluctuate. From a practical standpoint, actual values of Δ would depend on such factors as the size

of air bubbles, the extent of internal inhomogeneities etc. In the limiting case of very large Δ (i.e. only one segment between the two opposite electrodes), the mean V_{br} value would be at its highest level of 0.6 MV. With increasing number of fragments (i.e. smaller Δ parameter), the breakdown voltage is expected to decrease as the probability for a completed path via an inter-connection of low resistance segments increases. Figure 4-4 shows the variation in mean hold-off voltage with elemental length for a fixed 3 cm electrode separation and a σ_R of 100. Networks ranging from 10×10 to 40×40 were used to vary the number of elements placed along the 3 cm distance. The highest value is for the 10 × 10 network, with a monotonic decrease as expected.

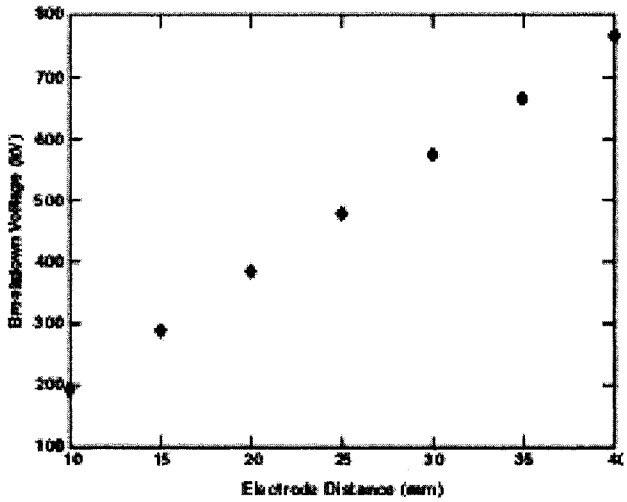

Figure 4-3. Scaling behavior of hold-off voltage with separation for a fixed σ_R = 100.

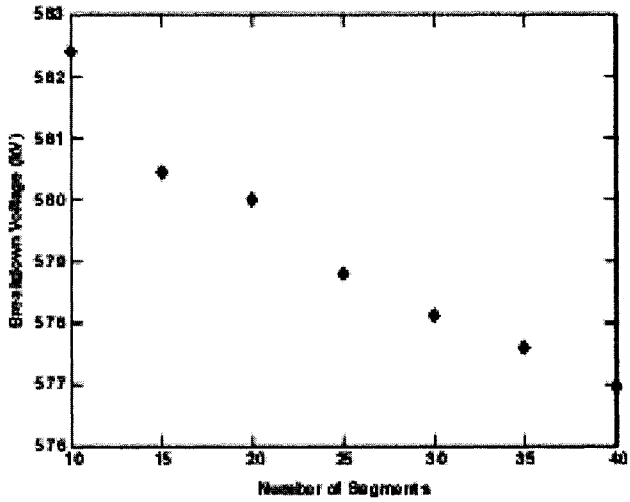

Figure 4-4. Variation in the mean hold-off voltage for a fixed 3 cm electrode separation and σ_R = 100 with the number of elements along each side. Networks ranging from 10x10 to 40x40 were used.

Finally, the relationship between the number of "broken" resistors and the total resistive elements in the network, at the breakdown threshold, was examined for possible fractal structure of these networks. As is well known for fractal structures, the total number of branches N(R) within a circle of radius "R" follows a power law [108]: $N(R) \sim R^D$, with D being a non-integer exponent. Alternatively, the power law can also be applied by varying the network size N × N, and plotting the relationship between the numbers of broken resistors (N_B) to N_T the total network elements [109]. Following this procedure based a number of different initial random seeds, the curve shown in Figure 4-5 was obtained. The values of <R> and σ_R were chosen to be 5000 and 100 Ohms, respectively. For convenience the numbers have been plotted on a log-log scale to the base 2. A curve fitting procedure to the points yielded the following least-square error relationship: $N_B = 0.25\ N_T^{0.96} \equiv k\ N_T^{\eta}$. Following Mandelbrot's area (A)-length (L) relation [108] of: $A^{0.5} \alpha L^{1/D}$, leads to $D = 2\eta$. Here, $\eta = 0.96$ which yields: D = 1.92. This value is very close to the fractal dimension of 1.89 for randomly diluted percolation

clusters on a two-dimensional (2D) lattice [110]. The close agreement between our calculation and the theoretical 1.89 value for a 2D geometry is very encouraging, and underscores the inherent fractal structure.

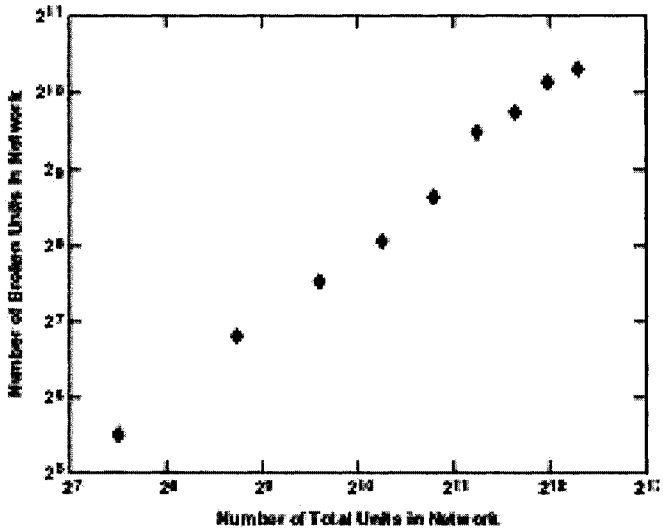

Figure 4-5. Relationship between number of "broken" resistors (N_B) versus the total number of resistor elements in network (N_T) to probe fractal properties.

4.3 Simulation Results and Discussion of 2D-Network Based Time-Dependent Percolative Model

4.3.1 Simulation Results of the Breakdown Process

Simulations for breakdown in a dielectric (such as purified/de-ionized water which is of interest to the pulsed-power community) were carried out for the point-plane electrode configuration based on the model outlined in the section 3.5. The value of $E_{threshold}$ was set to 6×10^7 Vm^{-1} in keeping with experimental reports on breakdown in water [15,111]. A small σ_R of 50 Ohms was taken to mimic the internal non-uniformities in conductance. These values were chosen to match the available experimental data, as discussed later. For simplicity, the results obtained here were for n = m (i.e. same size in 2 dimensions). Simulation results showing the final breakdown condition for a 40 × 40

network with an applied voltage of 7 kV are provided in Figure 4-6. A filamentary-type breakdown structure with a complete percolative path is obvious. The total physical dimensions for the network along each direction were taken to be 10^{-4} m. Thus, under ideal conditions (i.e. identical segments), a breakdown voltage of 6 kV is expected. In the presence of internal inhomogeneities and the sharp anode geometry, one expects the overall breakdown voltage to be lower. Here, however, a much higher applied voltage of 7 kV was taken to ensure breakdown would occur and that the duration would not be excessively large. The total time taken to achieve this final breakdown state was 1.85×10^{-7} s. This simulation demonstrates that breakdown involves the development of filamentary branches with associated random structure, followed by a complete percolative path. This is in keeping with experimental observations. Due to the slight variation σ_R in the initial resistor assignment, the breakdown is not completely symmetric.

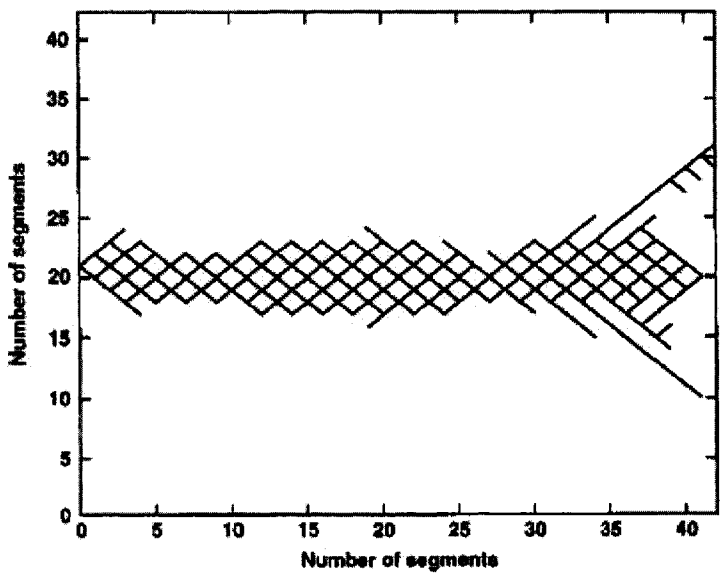

Figure 4-6. Numerical results of a breakdown percolative path a 40 × 40 network σ_R = 250 Ohms. A filamentary-type structure is predicted.

Simulation result of the breakdown structure during the transient phase, for the network of Figure 4-6 at different time instants is shown in Figs. 4-7(a)-(d). The times were 0.1356 μs, 0.1587 μs, 0.1655 μs, and 0.1723 μs, respectively. Propagating breakdown segments and progressive percolation are obvious. Also, the breakdown is predicted to initiate at the left electrode because of the higher electric field associated with the sharper geometry. Given the temporal nature of the present simulations, it was possible to compute the time-to-breakdown for a range of electric fields. The breakdown delay times thus obtained are plotted in Figure 4-8 as a function of the applied field. Experimental data on water breakdown obtained in our ODU experimental group are also shown for comparison. The experimental data was obtained by using pulsed voltages and the test circuit shown schematically in Figure 4-9. The test switch had a compact size and allowed its integration it into a two-stage pulse generator system. The gap spacing between the electrodes could be adjusted to an accuracy of 10 microns. A water outlet and inlet were also included to enable operation under "flow" conditions. The stored energy was in a 200 nF charging capacitor, which could be discharged via a primary switch triggered through a semiconductor (TTL) signal. The second stage energy store was in a 5 ns, 100 Ω, 93 mm length of a serpentine strip line having a total capacitance of 100 pF. The stripline was resonantly charged through a large choking inductance so as to reduce the charging current and protect the semiconductor switch. During the charging phase, the test switch acts as a simple load.

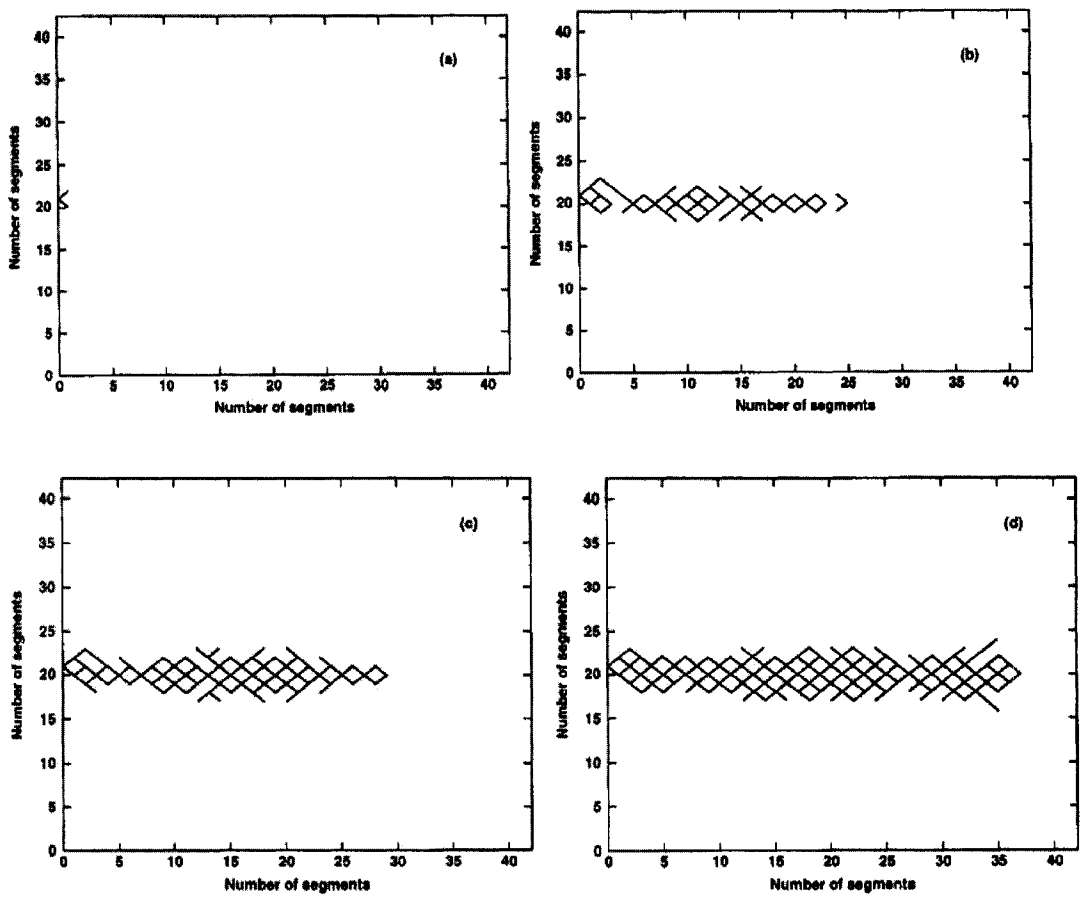

Figure 4-7. Simulation result showing the breakdown structure for the network of Fig. 3 during the transient phase at time instants of: (a) 0.1356 μs, (b) 0.1587 μs, (c) 0.1655 μs, and (d) 0.1723 μs. Propagation and incomplete percolation are obvious.

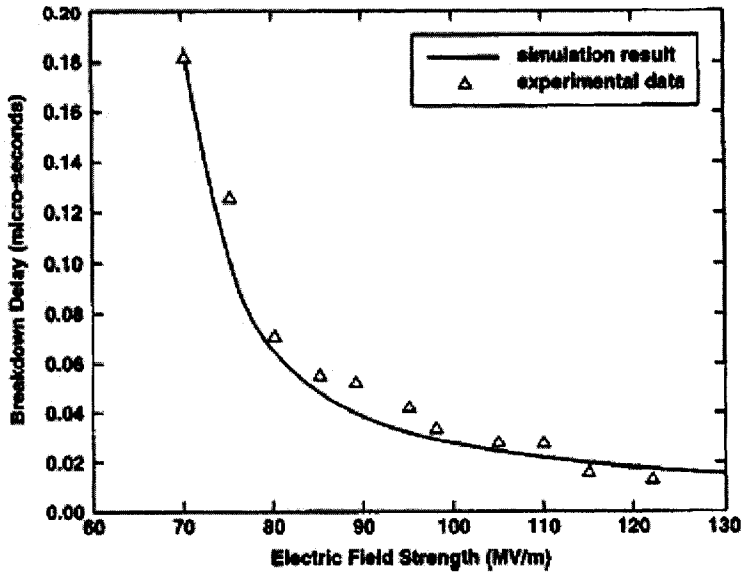

Figure 4-8. Plot of breakdown delay times versus the applied electric field strength for water in a 100 μm electrode gap. Available experimental data and simulation results are both shown, and reveal good quantitative agreement.

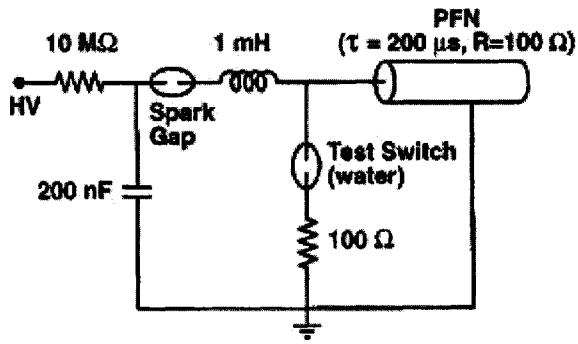

Figure 4-9. Schematic of the water switch and electrical circuit used in experiments. (Figure from private communication.)

The plot of Figure 4-8 for breakdown times versus applied electric field, were for a 100 μm electrode gap. A comparison between the available experimental data and simulation results reveal very good quantitative agreement. The durations of the pre-breakdown phase ranged from 15 ns to about 185 ns. A threshold electric field (E_{Br}) for breakdown is evident, and for values close to E_{Br} inordinately long times are predicted for

total failure. This trend is in keeping with the universal trends in breakdown durations of dielectrics under electric stress.

4.3.2 Dynamic Properties Analysis from Simulation Results

Based on the time-dependent, percolative model developed here, it becomes possible to monitor the successive movement of the elemental units as they break down sequentially. This, in essence, yields the propagation speed of the streamer tip as a function of time. Calculation results for the temporal development of the streamer speed are plotted in Figure 4-10 for an applied voltage of 7 kV. The plot shows that a finite, nonzero time-duration is required for the streamer to form. Hence, initially the streamer velocity is zero, and remains small as the streamer tip slowly advances towards the opposite side. Once the streamer has reached about 50% of the anode-cathode distance, the velocity begins to increase. Towards the end of this process, the velocity is predicted to reach high values in the 10^4 - 3×10^4 ms^{-1} range, with a peak just prior to the completion of a percolative path. The streamer speeds obtained here compare very well with the experimental report of a 1.2×10^4 ms^{-1} average value by Lisitsyn et al. [27]. The existence of a slow initial growth phase, followed by more rapid streamer propagation as obtained in the simulations here, has also been reported [112]. More importantly, the temporal development of streamer velocity matches Akiyama's experimental data on water breakdown [1]. The measured values were roughly 2×10^2 ms^{-1} during the initial initiation phase. This were followed by streamers velocities around 4×10^3 ms^{-1}, with final speeds of 4×10^4 ms^{-1} [1].

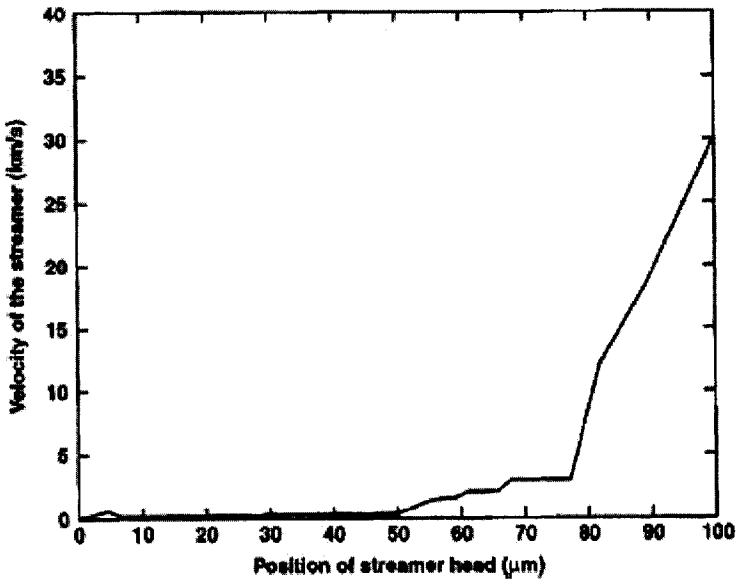

Figure 4-10. Calculated streamer velocity under a 7 kV external electric field condition for the 100 μm electrode gap.

Finally, simulation results for the temporal development of current in water, are shown in Figure 4-11. Prior to breakdown, the current is negligible, but stable. Transient behavior is seen to appear at around 1.15×10^{-7} s. The following features of the pre-breakdown phase are evident from Figure 4-11. (i) First, fluctuations in current appear beyond 1.15×10^{-7} s that are accompanied by large swings in magnitude. *Both positive and negative values are predicted.* Such multiple reversals in the current flow direction, have been reported in recent experiments by our experimental group [10]. Hence, the predicted current excursions of Figure 4-11, into both the positive and negative domain, are in agreement with measured data. (ii) The absolute magnitudes of the peak currents in Figure 4-11, are seen to be around 150 Amperes. These values match reported experimental data [10] very well. Hence, a rough quantitative concurrence is also seen to emerge. (iii) Despite the multiple excursions into the negative domain, the current

eventually tends to approach a relatively large positive value. This implies that eventually, as the final breakdown state approaches, the system settles down into a low resistance stable mode. This breakdown state, as already indicated in Figure 4-6, is filamentary in nature.

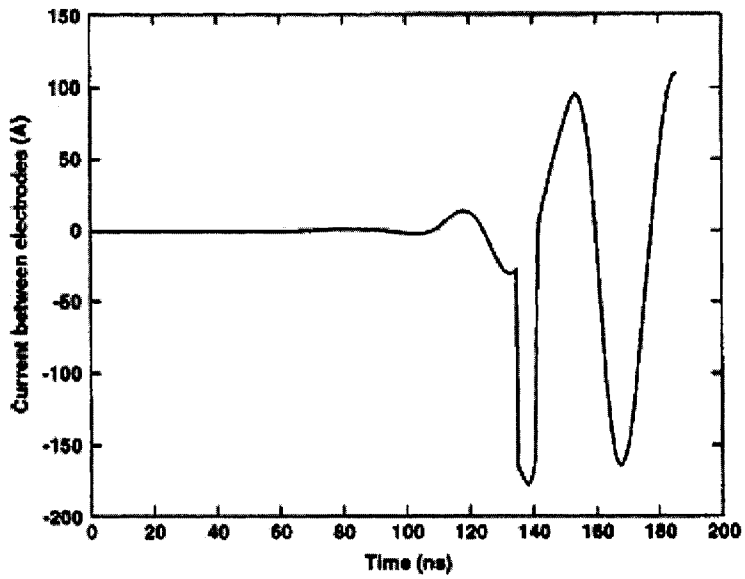

Figure 4-11. Calculated circuit current as a function of time prior to and immediately following liquid breakdown.

Direction reversal of circuit current and the occurrence of negative values in Figure 4-11 during the breakdown phase are of interest, and deserve some discussion. Though the details are complex and fashioned collective by the time-dependent behavior of all the resistor-capacitor elements, a simple physical understanding is provided, by considering the breakdown of a single unit as shown in Fig. 3-32. The total current I(t) across the resistor-capacitor combination of Fig. 3-32 is given as:

$$I(t) = d[C(t)*V(t)]/dt + V(t)/R(t) \ , \qquad (4.1)$$

where the capacitance C(t), the resistance R(t) and elemental voltage drop V(t) can all be time dependent. Physically, as the breakdown process starts, the elemental resistance is expected to reduce for two reasons. First, the localized vaporization leads to a creation (or growth) of a low-density region, in which scattering and inelastic scattering losses are lowered. This would effectively enhance the mobility and local electrical conductance. Second, the impact ionization and electron initiated generation would increase within the localized region, also leading to a decrease in the resistance R(t). Hence, the final resistance R_f following breakdown would be less than the R_{ini} value prior to the breakdown process. A capacitive change would also be associated with localized vaporization, or bubble formation or increase in a low-density localized region. This would arise since the relative dielectric constant would change from about 81 (the value for water), to a low value near unity (the value for air/gas.) The exact value though, would be dependent on the physical dimensions of the rarefied zone. In any case, the final value C_f in the breakdown state would be less than the pre-breakdown value of C_{ini} (i.e. $C_f < C_{ini}$.) Letting the following simple temporal relation model the time evolution of R(t) and C(t):

$$R(t) = [R_{ini} - R_f] * \exp[-K_1 * t] + R_f \,, \tag{4.2a}$$

$$\text{and,}\quad C(t) = [C_{ini} - C_f] * \exp[-K_2 * t] + C_f, \tag{4.2b}$$

where $K_{1,2}$ are the characteristic time constants for processes that lead to changes in the resistance and capacitance, respectively. Assuming that prior to the initiation of

breakdown at time t_0, the voltage V(t) and current I(t) are both roughly at a steady state (as corroborated by the curve of Figure 4-11 just before 1.15×10^{-7} s), one can obtain the temporal evolution of the circuit current $I(t > t_0)$ from Equations (4.2). This leads to the following expression for I(t) valid for times close to t_0 :

$$I(t) \sim V(t_0) [-K_2 (C_{ini} - C_f) * \exp(-K_2 * t) + \{(R_{ini} - R_f) * \exp(-K_1 * t) + R_f\}^{-1}] . \quad (4.3)$$

In the above, the voltage V(t) at times close to t_0 has been assumed to be nearly constant at $V(t_0)$. Though the above will deviate from the above for longer times, the crude model serves to demonstrate that the presence of the first term on the right side of Equation (4.3) can produce a net negative current. Physically, the formation and/or growth of a bubble (or low density region) leads to the collapse of the local capacitance. Consequently, the stored energy in the capacitor has to be released, and this process serves as a local source of energy that can drive a current. From an electrical circuit standpoint, the release of capacitive energy is akin to the introduction of a local active battery. The precise magnitude of the current evolution is obviously governed by the rate constant K_2 , which controls the speed of capacitive collapse. Hence, conceivably if K_2 were large, then the currents, at least at short times immediately following the breakdown initiation, could be negative. At later times, this trend would be overcome by decreases in the resistance, and by changes in the voltage across an elemental unit.

4.4 Positive Streamer (Pin Positive Electrode in Point-Plane Configuration) Simulation Results and Discussion of Drift Diffusion Time-Dependent Physical Continuum Model

4.4.1 Simulation Result of Electrical Breakdown Process with One Bubble

A time-dependent, two-dimensional simulation model discussed in section 3.6 was used for numerical studies of the water breakdown process. The external circuit was included via a 50 Ohm external resistor and a time dependent supply voltage $V_{app}(t)$. A uniform mesh was used to divide the entire device simulation region into equal sized boxes. Transport was characterized on the basis of drift-diffusion (DD) theory. The DD approach was used to update both the negative and position ion densities within each box taking account of inflows and outflows, bulk recombination and generation, charge creation due to field emission and impact ionization within micro-bubbles, negative ion generation at the cathode due to electron tunneling into the liquid, positive ion decay at the anode due to electron capture via the tunneling process, and positive ion annihilation at the cathode via electron transfer. Monte Carlo results (in section 3.2.3 and 3.2.4) were incorporated to yield the microscopic generation rates and spatial distributions. The liquid was assumed to be free of impurities, and to contain only the H^+ and OH^- ions. The ionic mobilities, taken from Light and Licht [46], were 3.5×10^{-7} $m^2 V^{-1}s^{-1}$ for H^+ and $2x10^{-7}$ $m^2 V^{-1}s^{-1}$ for OH^-. Free electrons generated within the micro-bubble were considered, and assigned a field dependent drift velocity v(E) given by: $v(E) = v_s \{E/[E+E_s]\}$, with F the electric field, v_s a saturation velocity taken to be 3×10^5 m/s, and $E_s = 3 \times 10^5$ V/m. Free electrons in liquid water were taken to have a lifetime of 200 ns. Current continuity was used to update the internal electric field E(x,y,t) and the potential

at grid points within the center of each box, through the relation: $J_{cct}(t) = [V_{app}(t) - V_{Dev}(t)]/R = d[\varepsilon(E)\, E(x, t)]/dt + \sigma E(x, t)$, with V_{Dev} being the device voltage, and $\varepsilon(E)$ the field-dependent permittivity.

An effective field dependent permittivity (in section 3.3) was used based on a detailed atomic-level analysis of the electrical response of water dipoles at the metal-liquid interface. This effectively leads to electric field enhancements arising from a positive feedback mechanism, since permittivity decreases with increasing electric field. The cross-sections were assumed to be rectangular, with a 200 μm distance between the point and plane electrodes in keeping with the experimental setup within our group. The impact ionization process was modeled in terms of the spatial multiplicative gain factor G{E(radius, t)} taken from the Monte Carlo simulations, as discussed in section 3.2.4. The rate of electron (and ion) production dn/dt at the bubble-liquid interface was proportional to the field-dependent emission rate G{E(t-mΔt)} from all previous applicable time steps. Thus, the cumulative effect was included, and time-delays in charge production from various locations downstream from the bubble taken into account.

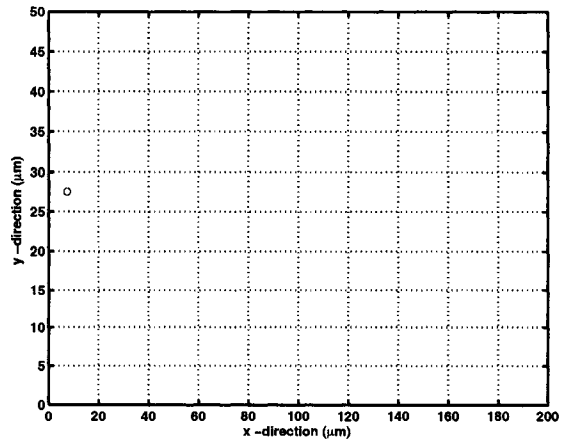

Figure 4-12. A positive polarity geometry and micro-bubble placement for the time-dependent breakdown simulations

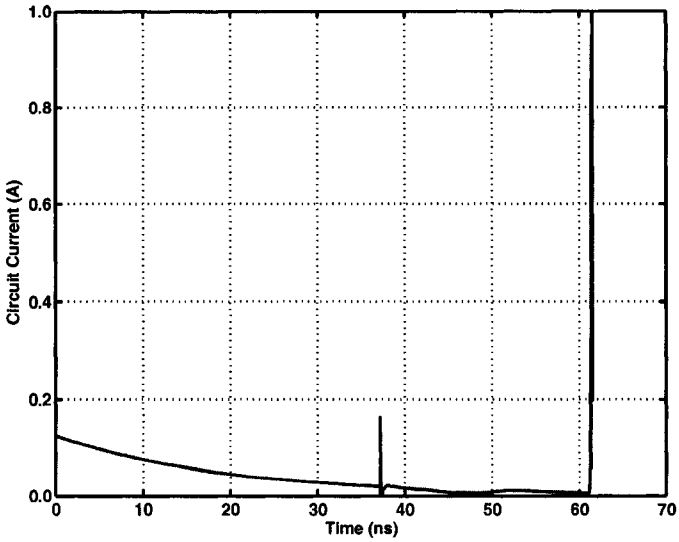

Figure 4-13. Predicted time-dependent current for the geometry of Figure 4-12.

Time dependent results for a rectangular simulation region shown in Figure 4-12 with the anode at x = 0 and the cathode on the opposite side are discussed next. The gap length was 200 μm in keeping with experiments. The longitudinal axis of symmetry corresponds to y = 0. For computational simplicity, the transverse dimension was restricted to 50 μm. Effectively then, only a small rectangular region close to the central axis was considered for these breakdown simulations. Figure 4-12 also shows a 1 μm radius micro-bubble placed off-axis near the anode side. A 40 kV exponential voltage pulse [= $V_{app}(t)$] with a 30 ns rise time was used. The time-dependent current obtained from the numerical simulation is shown in Figure 4-13. The initial displacement current is apparent, followed by a small current spike after about 37 ns, and an eventual breakdown at ~ 62 ns. The current spike is due to the localized micro-bubble "ignition". This breakdown delay time is in good agreement with actual experimental values. Snapshots of the internal voltage distribution at various times are given in Figure 4-14(a)-4-14(b). Perturbations in the potential are seen to initiate from the micro-bubble location.

Field emission at the bubble-water interface, followed by impact ionization of the gas, leads to rapid charge creation. The electric field between the micro-bubble and anode then decreases, while slow moving ions drifting towards the cathode contribute to local field enhancement downstream. A streamer is seen to develop, and the voltage distribution moves in a narrow stripe towards the cathode. Snapshots of the positive ion density at 49.76 ns and 59.73 ns are shown in Figure 4-15(a)-4-15(b), while the electric field at 57.93 ns is given in Figure 4-16. The field is seen to be highest at the tip of the advancing streamer (i.e. streamer head). Eventually, just prior to the final breakdown, strong electron emission is predicted to initiate from the cathode. Beyond this time, for a short duration, there are two streamers (not shown) that move towards each other at a rapid rate. A snapshot of the electron density just prior to breakdown is given in Figure 4-17. The sudden injection of electrons from the cathode side is evident in Figure 4-17. Such dual filamentary structures have recently been reported at Sandia National Laboratory [35]. In their experiments, an initial filament was seen to originate from the anode and move to the opposite electrode. This was followed by a secondary streamer formation and propagation from the cathode with a distinct time delay.

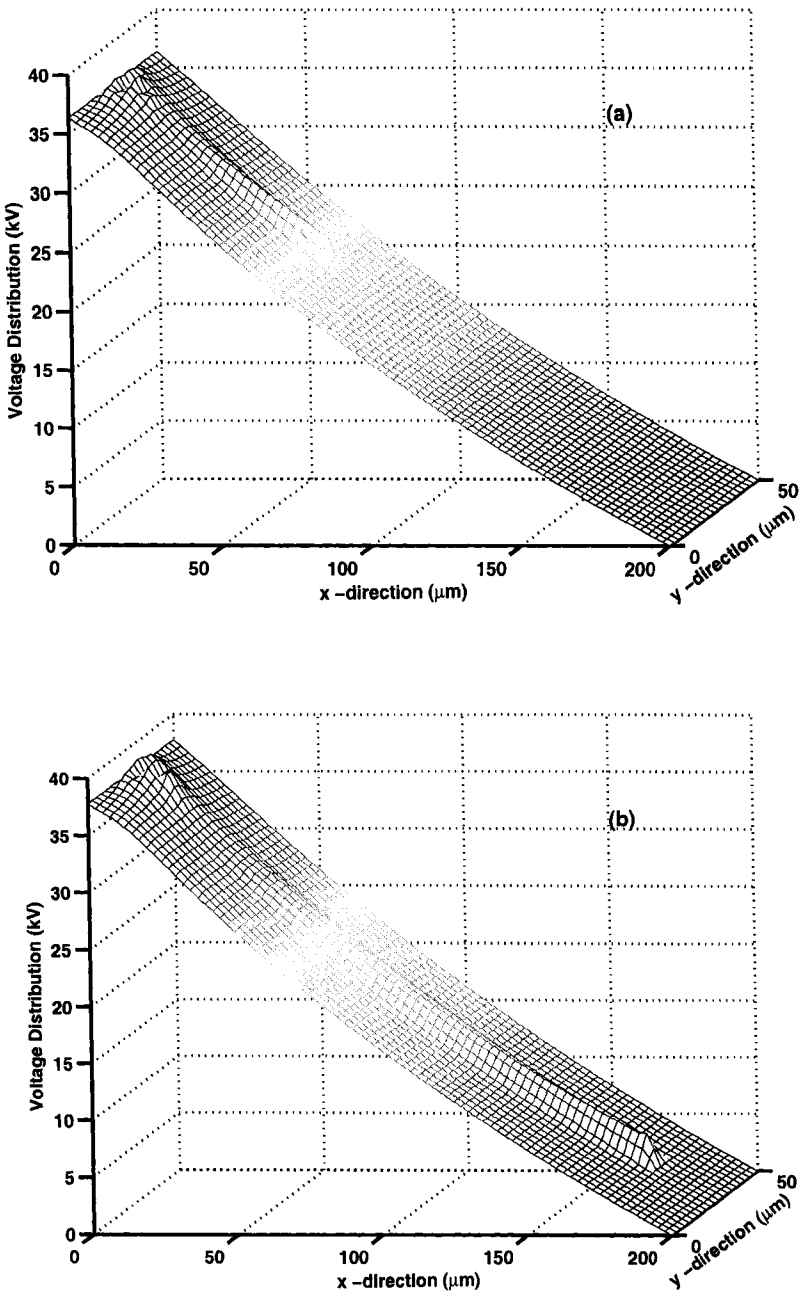

Figure 4-14. Snapshots of the internal voltage distribution at times of: (a) 49.76 ns and (b) 59.73 ns.

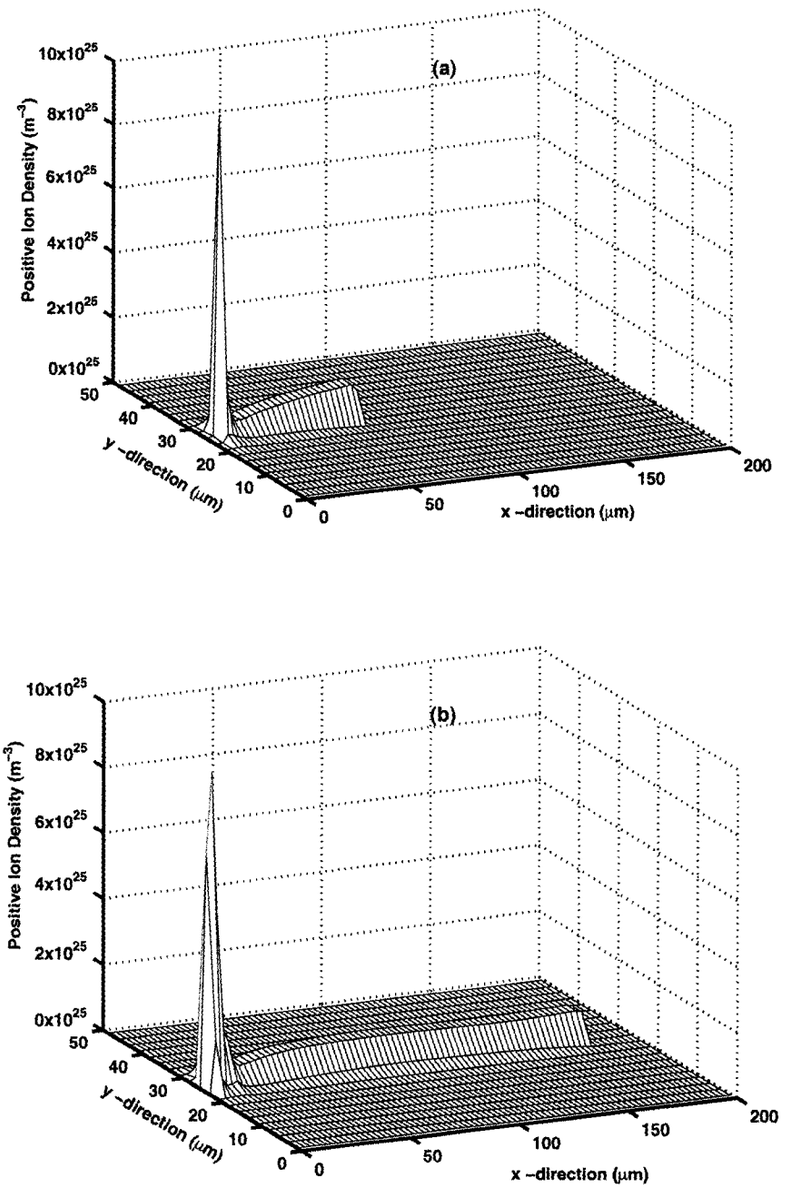

Figure 4-15. Snapshots of the positive ion density at times of: (a) 49.76 ns and (b) 59.73 ns.

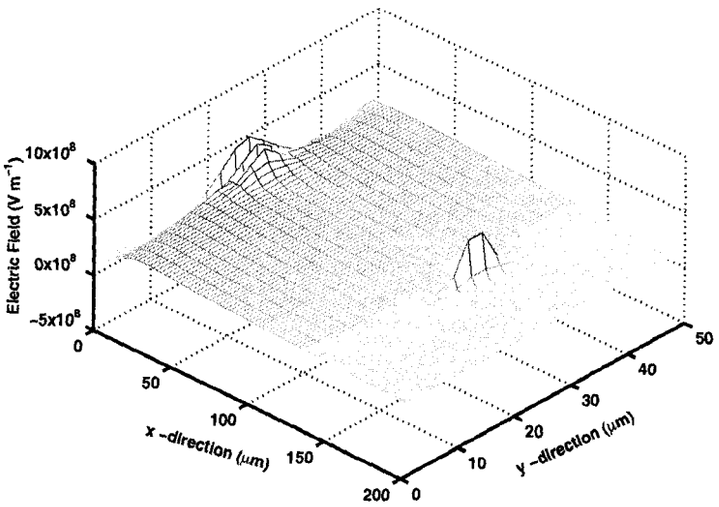

Figure 4-16. Snapshot of the simulation result for the internal electric field profile at 57.93 ns.

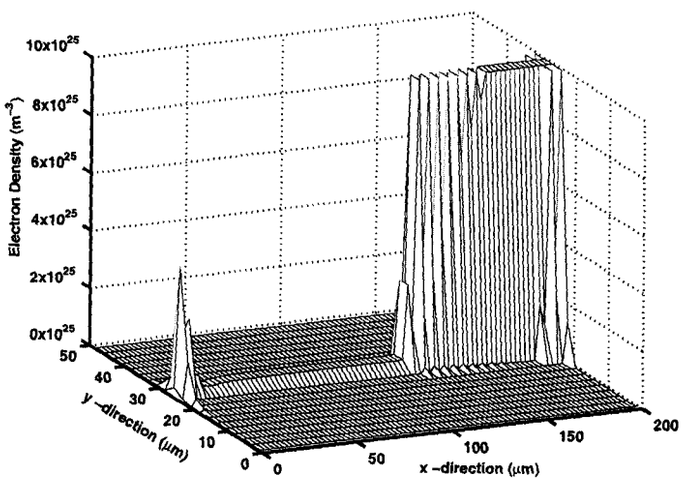

Figure 4-17. Snapshot of the electron density distribution just prior to breakdown.

4.4.2 Simulation Results Without Bubbles and With Multi-Bubbles Causing Streaming Branching

Simulations were also carried out for the same 200 μm configuration, but *without a micro-bubble.* The time-dependent current result is shown in Figure 4-18, and no breakdown is predicted. This underscores the important influence of micro-bubbles in initiating liquid breakdown.

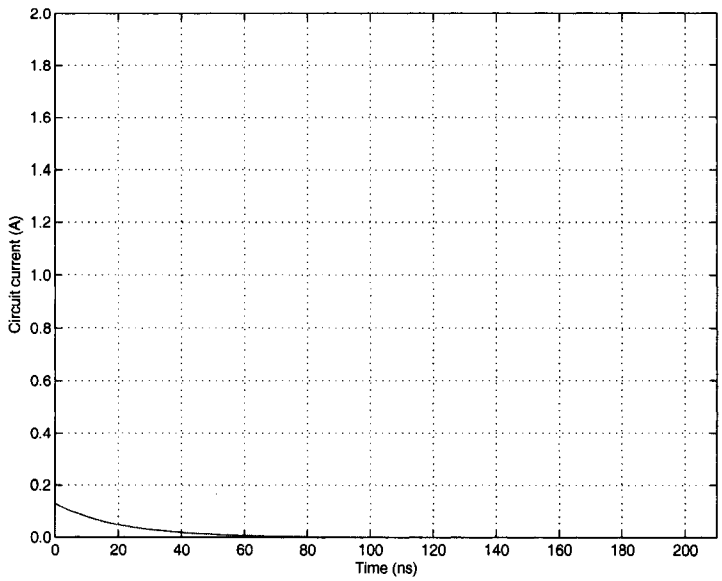

Figure 4-18. The predicted time-dependent current for the same geometric configuration of figure 10, but without a micro-bubble.

Next, the effect of multiple micro-bubbles is examined by simulating the geometry of Figure 4-19. Of the three micro-bubbles, one was close to the anode, while the other two were placed midway between the electrodes. The time dependent current predicted from our calculations is given in Figure 4-20. As compared to the single micro-bubble case of Figure 4-13, there is negligible change in the current transient. The Multiple bubbles do not significantly change the speed, since the bubbles further away from the anode experience a lower electric field, and can only be triggered *after* the primary streamer has advanced to their neighborhood. Thus, the triggering is essentially

a sequential process. This arises from streamer branching for this situation as made explicit through Figs. 4-21(a)-(c). These figures show snapshots of the positive charge distribution at the time instants of 49.75 ns, 55.75 ns and 63.26 ns, respectively. The primary streamer is associated with the micro-bubble closest to the anode and begins propagating first. As the streamer reaches the two other micro-bubbles, the local electric field is enhanced, causing both bubbles to turn on. Dual streamers then begin to propagate towards the cathode. The dual turn-on essentially discontinues the original streamer. There is an internal re-distribution of the electric field as the two micro-bubbles are ignited. The net result is a slowing of the ionization wave, and a slight delay in the overall breakdown time results in Figure 4-20. This result demonstrates that such dendritic formations must be stochastic events that depend on both the local electric field and fluctuations in material density.

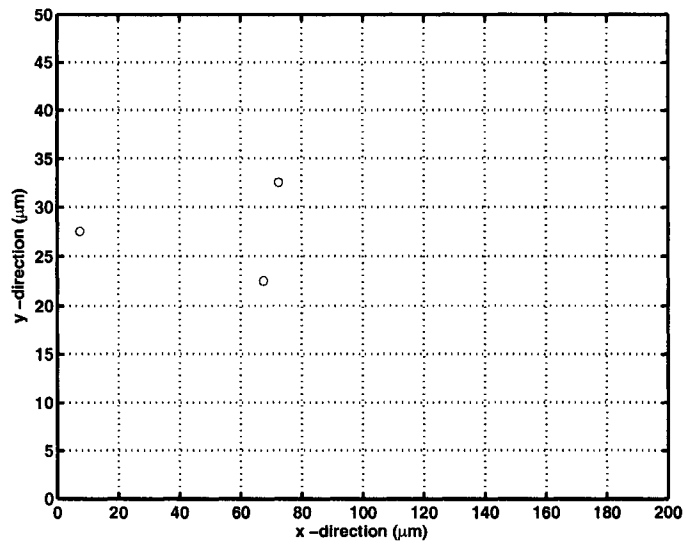

Figure 4-19. Another positive polarity geometry and micro-bubble placement for the time-dependent breakdown simulations.

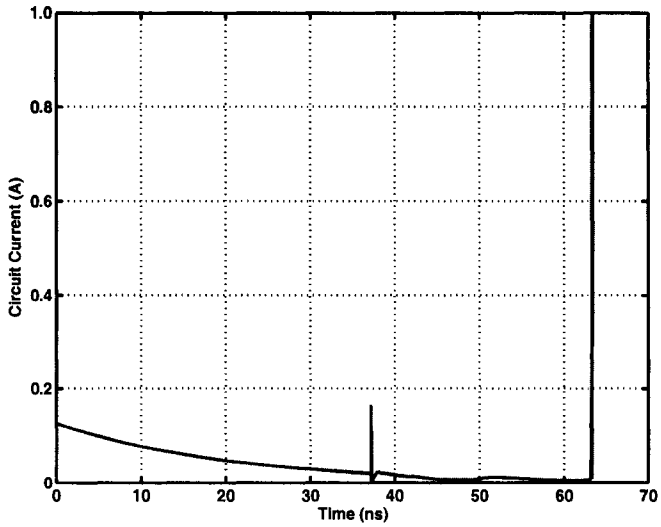

Figure 4-20. The predicted time-dependent current for the geometry of figure 4-19.

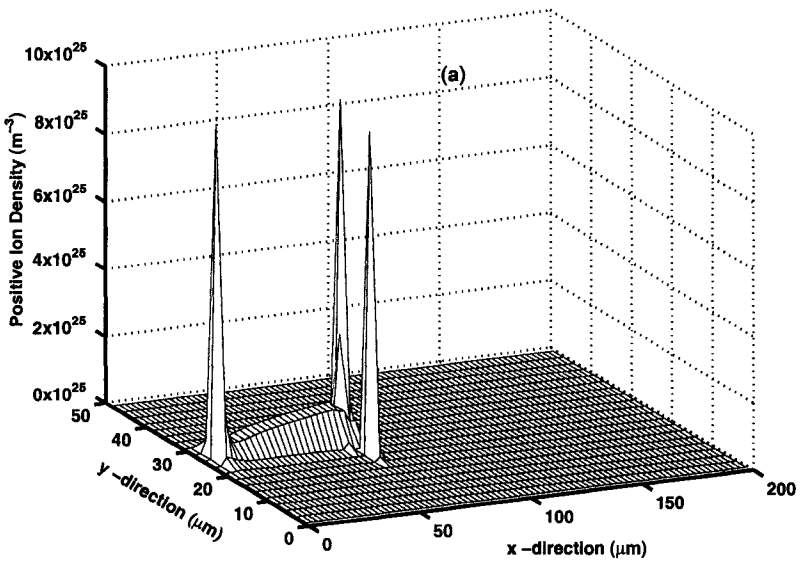

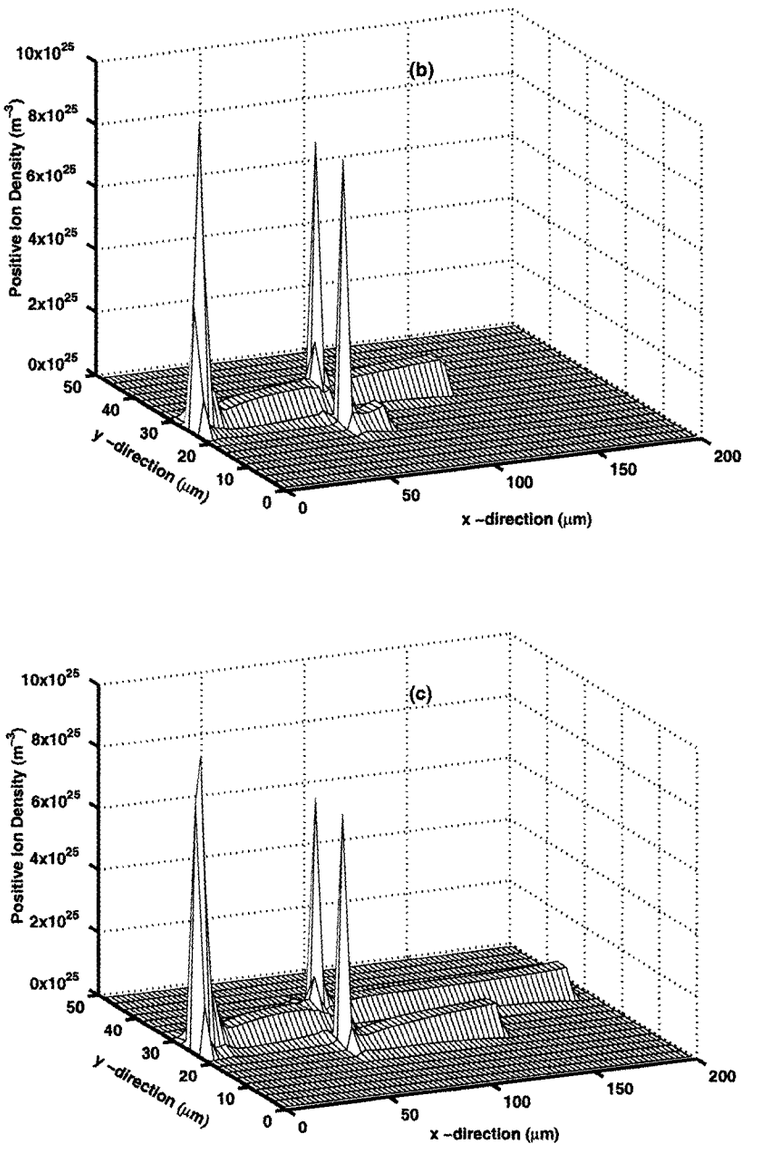

Figure 4-21. Snapshots of the positive ion density at times of: (a) 49.75 ns, (b) 55.75 ns, (c) 63.26 ns.

4.5 Simulation Results of Negative Streamer and Comparison with the Positive Streamer Case

Time dependent negative streamer simulation results showing the breakdown initiation and evolution of the electric field and charge densities are shown and discussed in this section. For clarity, we first focus on the negative polarity (i.e., the point electrode being the cathode), and subsequently compare negative polarity case with the positive polarity one.

4.5.1 Negative Polarity Case

Time dependent results for a rectangular simulation region shown in Figure 4-22 with the cathode at x = 0 and the anode on the opposite side are first discussed. The gap length was 200 μm in keeping with experiments. The longitudinal axis of symmetry corresponds to y = 0. For computational simplicity, the transverse dimension (along y-axis) was restricted to 240 μm. Effectively then, only a small rectangular region close to the central axis was considered for these breakdown simulations. Figure 4-22 also shows a 1 μm radius micro-bubble (not drawn to scale) placed off-axis near the cathode side. A 48 kV exponential voltage pulse [= $V_{app}(t)$] with a 30 ns rise time was used. The time-dependent current obtained from the numerical simulation is shown in Figure 4-23. The initial displacement current is apparent, and an eventual breakdown occurs at ~155 ns. This time to breakdown is roughly consistent with experimental observations. It may also be mentioned that the measured data indicates the breakdown time to be around 70 ns for *positive polarity*, and is be attained with a lower 40 kV pulse. In our simulations, a 40 kV pulse did not cause breakdown for the negative polarity case, and instead, the

higher 48 kV bias was found necessary. The longer breakdown delay time of ~ 155 ns for the negative polarity case is also in agreement with data.

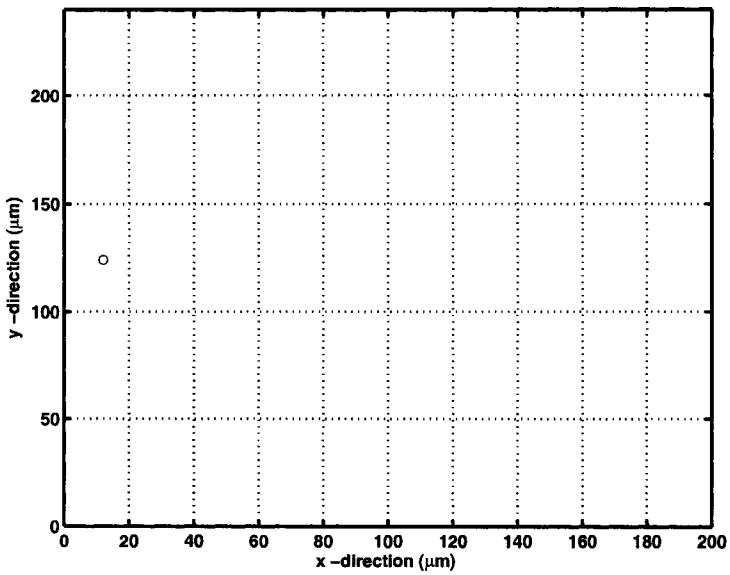

Figure 4-22. Geometry and micro-bubble placement for the time-dependent breakdown simulations

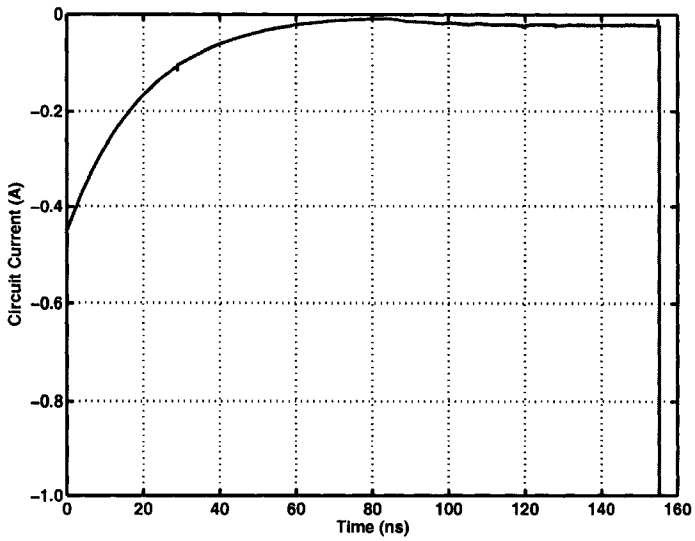

Figure 4-23. Predicted time-dependent current for the geometry of Figure 4-22.

Snapshots of the internal voltage distribution at various times are given in Figs. 4-25(a)-(c) for this 48 kV, negative-polarity case. Perturbations in the potential are seen to initiate from the micro-bubble location. Field emission at the bubble-water interface, followed by impact ionization of the gas, leads to rapid charge creation. The electric field between the micro-bubble and cathode then decreases, while the electrons drifting towards the anode contribute to local field enhancement downstream. A streamer is seen to develop, and the voltage distribution moves in a stripe towards the anode. Charge is continually created at the tip as it advances, through the field-ionization process. Snapshots of the negative ion density at 64.46 ns and 99.07 ns are shown in Figs. 4-26(a)-(b). The spatial extent of the negative charge along the transverse direction is roughly 50 μm. However, the thickness of the streamer is much smaller, being roughly 4 μm. Also, a lower applied voltage of 40 kV is seen to be sufficient to bring about breakdown for the positive polarity case. Filaments for the *anode-polarity case are much narrower by comparison*. This result is consistent with known experimental results. For example, streamers formed from the anode tip typically have more branches and a distinct "tree-like" structure spanning a conical volume, as shown in Figure 4-24(a). Cathode-tip streamers, on the other hand, are less bushy and usually have a prominently thick "root" structure as indicated in Figure 4-24 (b).

(a)

(b)

Figure 4-24. Typical streamers in liquid for a point-plane geometry. (a) A positively biased point electrode, and (b) a negatively biased point electrode. (From private communication.)

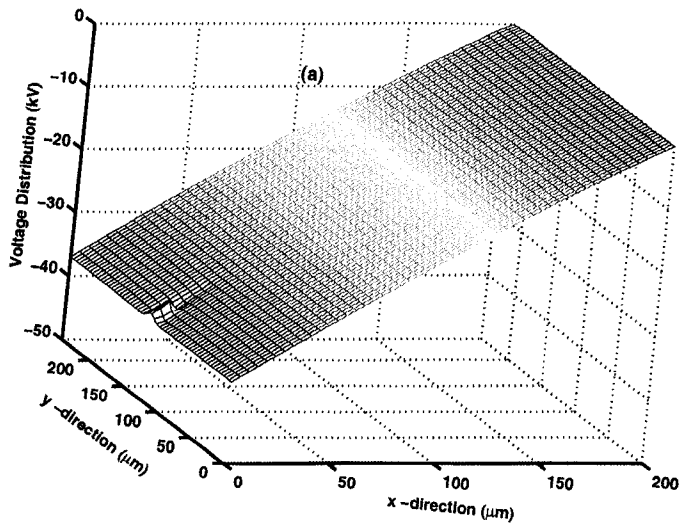

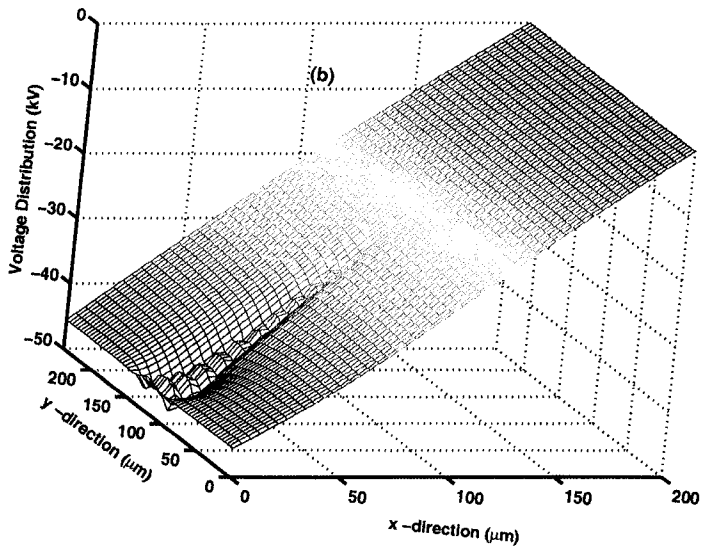

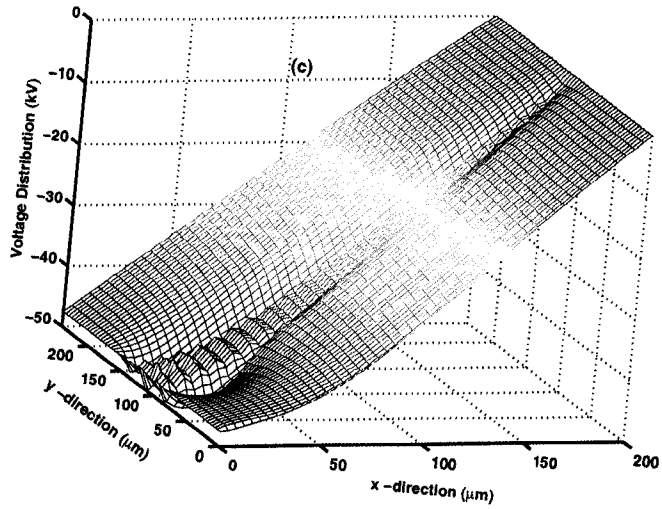

Figure 4-25. Snapshots of the internal voltage distribution at times of: (a) 34.46 ns, (b) 4.46 ns, (c) 99.07 ns respectively.

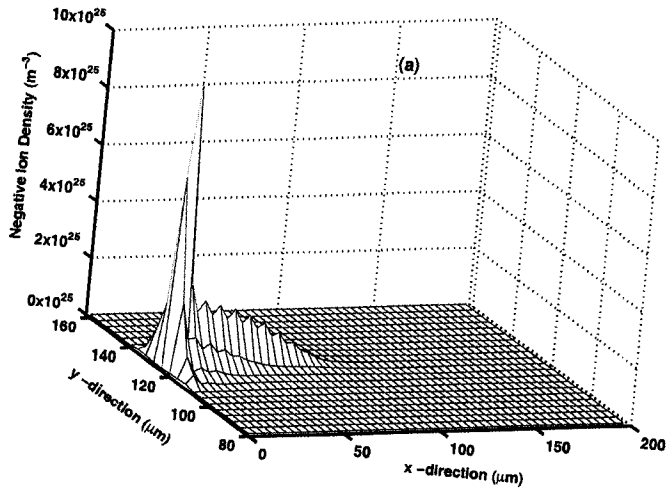

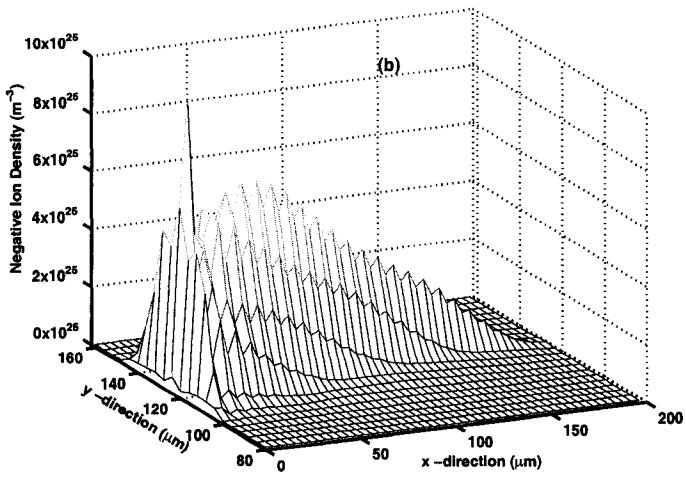

Figure 4-26. Snapshots of the negative ion distribution at times of: (a) 64.46 ns and (b) 99.07 ns

The influence of micro-bubble location and density is examined next. Figure 4-27 shows a single micro-bubble placed slightly further off-axis than the previous case of Figure 4-22. All other parameters (e.g., the overall geometry and 48 kV pulse) were otherwise unchanged. The time dependent current is shown in Figure 4-28. An increase in breakdown time to about ~ 220 ns is seen. The longer breakdown delay arises because the electric field magnitude decreases with increasing transverse distance from the central axis. Since charge generation (due to both the field-emission and impact ionization processes) has a highly non-linearly dependence on electric field, a longer time for charge creation and its build up results for micro-bubbles that are further off-axis. Next, the effect of multiple bubbles on the breakdown behavior was analyzed. Figure 4-29 shows three micro-bubbles, with the one nearest the cathode on the left side being identical in location to that of Figure 4-27. Thus in the present simulation, two more micro-bubbles were added roughly halfway between the electrodes. The time dependent current is shown in Figure 4-30, and is nearly identical to that of Figure 4-27. Thus, no appreciable

reduction in breakdown time is predicted, and the micro-bubble multiplicity does not have a big effect. This demonstrates the initial plasma ignition and growth to be an important step. Once a high-density plasma is locally initiated, it then grows quickly (as the non-linear field-dependent ionization aids this process), and propagates. Multiple bubbles do not add significantly to the speed, since each has about the same breakdown delay time associated with its internal charge formation. In fact, the micro-bubbles located further away from a sharp electrode (the cathode in this case) take longer to "ignite". The micro-bubbles closest to the electrode start the breakdown process, and as the electric-field progresses (with the streamer motion), micro-bubbles further down then get activated. Figs. 4-31(a) and 4-31(b) show snapshots of the negative ion density at 73.34 ns and 192.00 ns, respectively. An important feature of these figures is that a single broad distribution is seen. No internal branching into two or three streamers is evident. Though the two micro-bubbles, located midway between the electrodes, get "turned-on" by the electric field of the advancing streamer, the charge does not bifurcate into two separate streams. The relatively fast drift and diffusion of the moving electrons simply leads to a single, overall smeared distribution. This is in contrast to the results for the anode polarity, discussed in last section (section 4.4), which exhibits streamer branching.

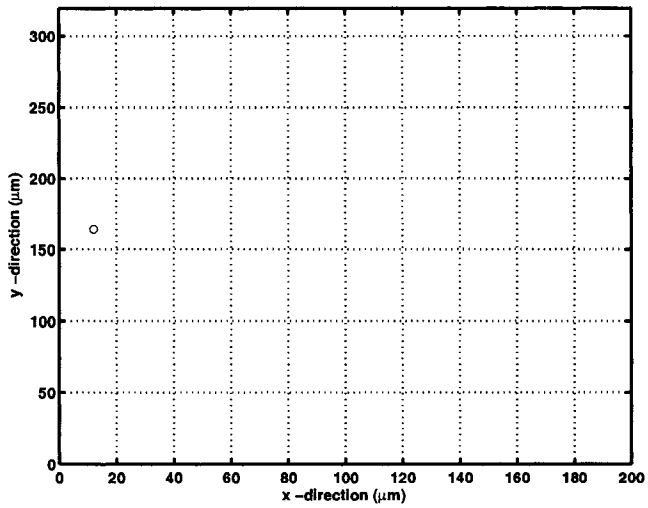

Figure 4-27. A second geometry and micro-bubble placement for the time-dependent breakdown simulations.

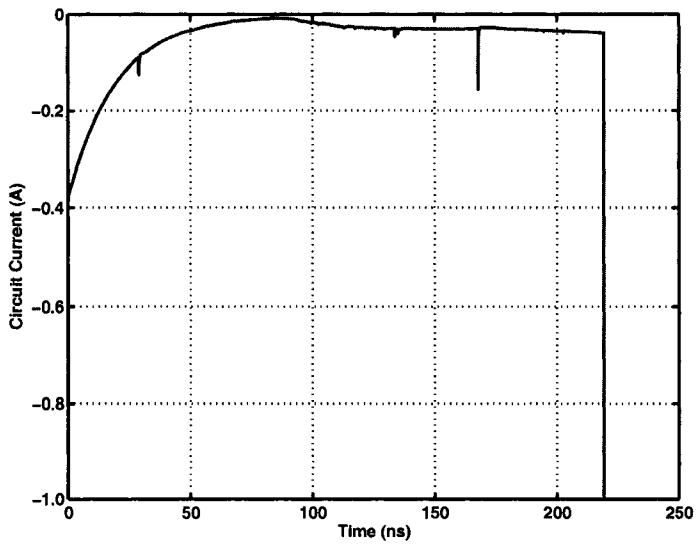

Figure 4-28. The predicted time-dependent current for the geometry of Figure 4-27.

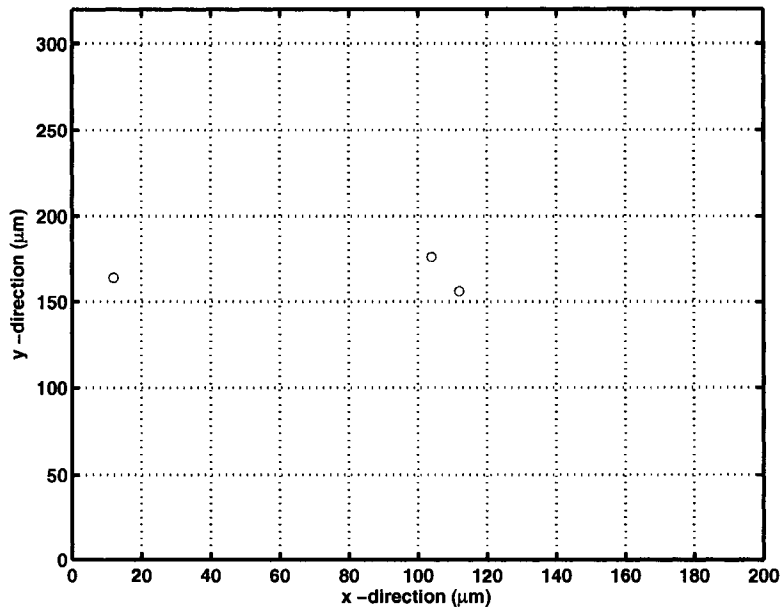

Figure 4-29. Another geometry and micro-bubble placement for the time-dependent breakdown simulations.

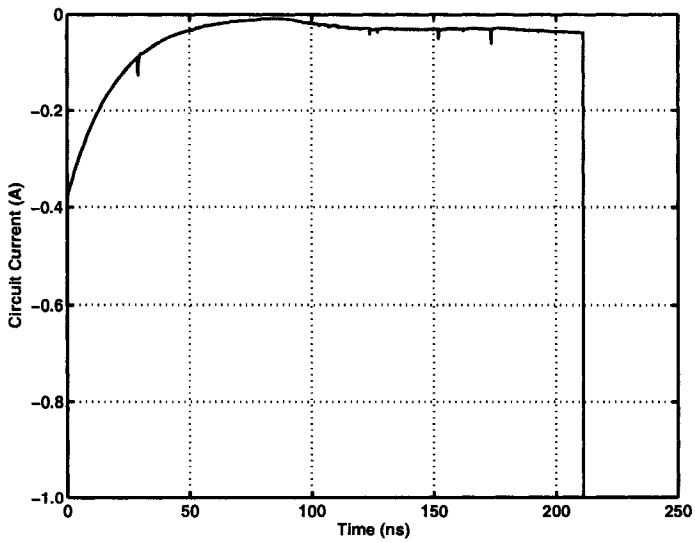

Figure 4-30. The predicted time-dependent current for the geometry of Figure 4-29.

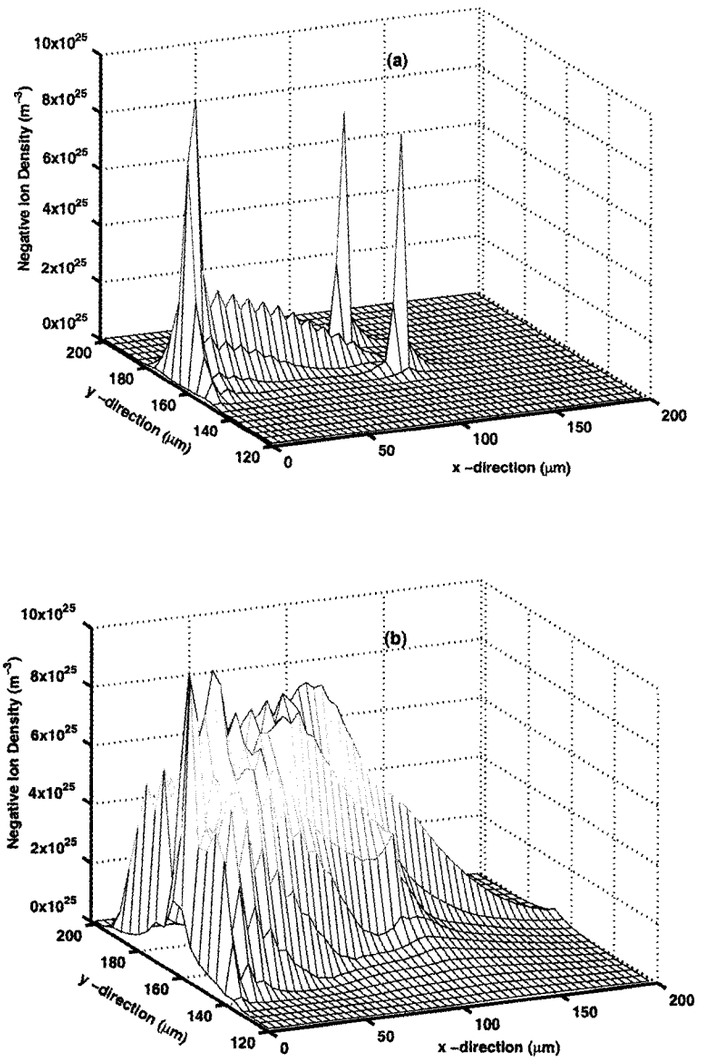

Figure 4-31. Snapshots of the negative ion density at times of: (a) 73.34 ns and (b) 192.00 ns, respectively.

4.4.2 Polarity Effect Discussion: Comparison Between Negative and Positive Streamer Cases

An important focus of this section is on the polarity effects that have been observed in asymmetric electrode geometries (as seen in Figure 4-24). An explanation has been offered for the inherent asymmetry in hold-off voltages, breakdown delay times, the streamer geometric shapes, and polarity-dependent thickness of filaments. The polarity effects were shown to arise from the large mobility difference between electrons and ions. For electrons, the higher mobility was shown to produce a greater charge smearing and diffusion upon creation at the internal micro-sources and streamer tips. This influenced the local electric field distributions. Subsequent non-linear coupling between the number density, electric field and charge generation rates collectively worked to affect the temporal dynamics and the geometric shape of ionized channels.

The simulation showed clear differences between the anode-directed and cathode-directed streamers. Electric fields necessary for generating a breakdown streamer were lower for an anode-side triggering event. For example, a 40 kV bias was sufficient for causing breakdown across a 200 μm gap with the smaller electrode biased positively (i.e., the positive polarity). However, a much larger value of 48 kV was seen to be necessary for the negative polarity. Such differences in breakdown threshold voltage have been observed experimentally. Also, the breakdown delay times for the anode-polarity were shorter (with faster propagation velocity), in agreement with recent experimental data. In addition, from the comparison of Figure 4-26 and Figure 4-15, cathode-directed streamers were shown to have lower transverse dimensions, associated with a lower spreading (due to both drift and diffusion) of the generated charge. This agreed with experiments showing anode-directed streamers to have a thicker root and larger radial

size. Lastly, the streamers emanating for the anode polarity in our simulations, exhibited branching under multiple micro-bubble conditions as shown in Figure 4-21.

4.6 Summary

It has been shown in section 4.2 that the primitive percolative model can successfully predict fractal structure in dielectric breakdown. In particular, the fractal dimension for a 2D lattice as given by the exponent of a power law, agreed with the theoretically expected value. The dependence of critical external voltage on the internal disorder was also investigated. Moreover, time-dependent results were shown in section 4.3 based on the improved percolative model. That included the streamer propagation shape and its velocity, and time-dependent circuit current.

After the successful prediction on the random patterns in the liquid electrical breakdown process, simulation results based on the accurate, time-dependent physical drift diffusion model in section 3.6 have been presented in the section 4.4 and section 4.5. Results have shown that under low-density situations (such as bubble), electron field emission followed by impact ionization would be operative and makes for the creation of internal plasma micro-sources. The time-dependent current was shown to exhibit slight fluctuations as the micro-bubbles were successfully triggered internally. Furthermore, it was shown that branching of streamers and the formation of random dendritic structures could occur in the presence of an inhomogeneous distribution of micro-bubbles. An important simulation results based the DD model was on the polarity effects that have been observed in asymmetric electrode geometries. An explanation has been offered for the inherent asymmetry in: (a) hold-off voltages, negative streamer has about 20% higher

hold-off voltage; (b) breakdown delay times, negative streamer travels slower normally; (c) the streamer geometric shapes, negative streamer has thicker root and streamer transverse and less branching. The polarity effects were shown to arise from the large mobility difference between electrons and ions. For electrons, the higher mobility was shown to produce a greater charge smearing and diffusion upon creation at the internal micro-sources and streamer tips. This influenced the local electric field distributions. Subsequent non-linear coupling between the number density, electric field and charge generation rates collectively worked to affect the temporal dynamics and the geometric shape of ionized channels.

CHAPTER V

CONCLUSIONS AND FUTURE RESEARCH

5.1 Research Summary

We have simulated the sub-microsecond electrical breakdown of liquid dielectrics using several models. These include the percolative model and a fluid, drift-diffusion approach. For concreteness, water has been used as the liquid of choice since it is popularly used in several applications. In this dissertation research, the physical processes of liquid-dielectric electrical breakdown in response to sub-microsecond pulses were systematically analyzed. These mechanisms and characteristic details for liquids are quite different from both solid and gaseous dielectric electrical breakdown.

Present analysis of the physical properties of sub-microsecond liquid-dielectric electrical breakdown helped answer the following questions and aspects.

(A) Electrical energy in the nanosecond electrical breakdown system was shown to be insufficient to vaporize the normal liquids (e.g. water in the present case). Hence, it was shown that thermally stimulated electrical breakdown would seem to be quite unlikely.

(B) A strong electrical field enhancement was shown to be possible due to collective dipole alignment effects. This is likely to occur close to the electrodes, and even at the interface between the liquid and a micro-bubble.

(C) It was demonstrated that electrons could not easily impact ionize the liquid water molecules under the electrical field strengths typically applied. The strong isotropic scattering at the lower energies would curtail the mean-free path and not allow electrons to pick up the requisite energy for impact ionization. Instead, the calculations showed that electron impact ionization inside micron-sized bubbles would facilitate electrical breakdown.

(D). The field-dependent behavior of the dielectric constant of liquid water was probed. Its value was shown to be a monotonic decreasing function of the electrical field. This trend has been borne out in experiments, and the process helps accentuate the liquid electrical breakdown.

Following the various analyses mentioned above, the physical drift-diffusion (DD), micro-bubble based model was introduced. It has been proposed that breakdown is initiated by field emission at the interface of pre-existing micro-bubbles. Impact ionization within the micro-bubble gas then contributes to plasma streamer development. Based on the drift-diffusion model, the entire breakdown process and its initiation can be adequately explained. Simulation results based on the DD model predicted many of the observed experimental details. These include the following:

(i) Under low-density conditions (such as at a micro-bubble), electron field emission followed by impact ionization would be operative and create internal plasma micro-sources.

(ii) The time-dependent current was shown to exhibit slight fluctuations as the internal micro-bubbles were successively triggered. Furthermore, it was shown that branching of streamers and the formation of random dendritic structures could occur in the presence of an inhomogeneous distribution of micro-bubbles.

(iii) An important simulation result based the DD model was on the polarity effects that have been observed in asymmetric electrode geometries. An explanation has been offered for the inherent asymmetry with regards to the following: (A) Hold-off voltages with negative streamers exhibiting about 20% higher hold-off voltage values; (B) Breakdown delay times with negative streamers traveling slower than the positive streamers; (C) The streamer geometry and shape. The negative streamers typically have a thicker root and less branching. The polarity effects were shown to arise from the large mobility difference between electrons and ions. For electrons, the higher mobility was shown to produce a greater charge smearing and diffusion upon creation at the internal micro-sources and streamer tips. This influenced the local electric field distributions. Subsequent non-linear coupling between the number density, electric field and charge generation rates collectively worked to affect the temporal dynamics and the geometric shape of ionized channels.

In addition to the physical DD model, the percolative model simulation results successfully predicted fractal structure during dielectric breakdown. In particular, the fractal dimension for a 2D lattice as given by the exponent of a power law, agreed with the theoretically expected value. The dependence of critical external voltage on the internal disorder was also investigated. Moreover, time-dependent results were obtained

based on an improved percolative model. The details included the streamer propagation shape, its velocity, and time-dependent circuit current.

5.2 Future Work

Some useful and continued research in this interesting area can be carried out. Some of the potential studies and modeling work relevant to liquid-dielectric, electrical breakdown are briefly mentioned below. None of the following aspects was addressed in this dissertation, but is very relevant and merits subsequent work.

1. Transient shockwave has been seen in experimental liquid dielectric breakdown system because of fast and localized injection of electrical energy. This injection probably arises from filamentary sites. It is important to analyze the shockwave process, its initiation and growth since shock waves are detrimental to the stability and reliability of the electrical systems. The overall practical goal would be to minimize the mechanical damage from the shockwaves. Hence, an important follow-on task would be to model and simulate the creation and propagation process of shockwaves in the liquid dielectric stressed to the high electric fields.

2. Triggering liquid dielectric electrical breakdown by laser might be an efficient way to switch the liquid dielectric system. In such a case, the liquid dielectric would act a large and efficient capacitive storage unit. Focusing a laser beam on the liquid dielectric gap could be used to initiate a discharge and switch the storage system

into a highly conductive mode. This optically initiated triggering process is very easy to implement in our present model. An additional optically generated source term dependent on time and position would be needed in the model. The polarity effect in that system could then an also be simulated by the physical drift-diffusion model, as done in this dissertation research. Aspects such as the relative benefits of bulk-water turn-on versus electrode illumination could also be probed.

3. Extending our simulation results based on the drift-diffusion model to other liquids (particularly non-polar oils) is an interesting research aspect. By implementing different physical parameter, such as dielectric constant, ionization energy, density etc, the electrical breakdown characteristics and hold-off voltage values could be obtained. Such modeling would help provide useful comparisons between various liquids and aid in their selection for a given application.

4. Extending the present drift-diffusion model to large dimensional systems is also an interesting research. Multi-grid method and parallel computing may be used in the simulation of such large sized systems. An efficient calculation of the Poisson equation with non-uniform dielectric function is very important to such large dimensional system simulations. Another challenge would be to effectively simulate the coupled non-linear carrier transport equation with all the additional computer memory requirements.

REFERENCES

1. H. Akiyama, IEEE Trans. Dielectr. Electr. Insulation **7**, 646 (2000).
2. J. Gaudet, R. J. Barker, M. Gundersen, A. Kuthi, A. Neuber, J. Dickens, W. Nunnally, E. Schamiloglu, C. Christodoulou, S. Tyo, K. H. Schoenbach, R. P. Joshi, M. Laroussi, J. Kolb, and R. Vidmar, Proc. IEEE **92**, 1144 (2004).
3. J. Talati, T. Shah, A. Memon, M. Sidhwa, S. Adil, and A. Omair, Journal of Urology **146**, 1482 (1991).
4. A. H. Olson and S. P. Sutton, The Journal of the Acoustical Society of America **94**, 2226 (1993).
5. M. Zahn, Y. Ohki, D. B. Fenneman, R. J. Gripshover, and V. Gehman, Jr., Proc. IEEE **74**, 1182 (1986).
6. M. R. Patel, M. A. Barrufet, P. T. Eubank, and D. D. DiBitonto, J. Appl. Phys. **66**, 4104 (1989).
7. I. Vitkovitsky, *High Power Switching* (Van Nostrand Reinhold Company, New York, 1987), pp. 116-137.
8. D. L. Johnson, J. P. Vandevender, T. H. Martin, IEEE Trans. Plasma Sci. **8**, 204 (1980).
9. R. P. Joshi, J. Qian and K. H. Schoenbach, J. Appl. Phys. **92**, 6245 (2002).
10. S. Xiao, J. Kolb, S. Kono, S. Katsuki, R. P. Joshi, M. Laroussi, and K. H. Schoenbach, IEEE Trans. Dielectr. Electr. Insulation **11**, 604, 2004.
11. P. K. Watson and A. H. Sharbaugh, J. Electrochem. Soc. **107**, 516 (1960).
12. N. J. Felici, J. Electrostat. **12**, 165 (1982) ; N. J. Felici, IEEE Trans. Electr. Insul. **EI-20**, 233 (1985).

13. A. Nikuradse, *Das Flηssige Dielektrikum* (Springer, Berlin, 1934), pp. 134-152.

14. F. Pontiga and A. Castellanos, IEEE Trans. Dielectr. and Electrical Insulation **3**, 792 (1996).

15. E. E. Kunhardt, Physical Review B **44**, 4235 (1991); H. M. Jones and E. E. Kunhardt, J. Appl. Phys. **77**, 795 (1995).

16. E. O. Forster, IEEE Trans. Electr. Insulation **25**, 45 (1990).

17. T. J. Lewis, IEEE Trans. on Electr. Insula. **EI-20**, 123 (1985).

18. P. Keith Watson, W. G. Chadband, M. Sadeghzadeh-Araghi, IEEE Trans. Electr. Insulation **EL-26**, 543 (1991).

19. A. Beroual, C. Marteau, and R. Tobazeon, IEEE Trans. on Electr. Insula, **23**, 955 (1988) ; T. Aka-Ngnui and A. Beroual, J. Phys. D: Appl. Phys. **34**, 794 (2001).

20. J. Qian, R. P. Joshi, K. H. Schoenbach, E. Schamiloglu, and C. Christodoulou, IEEE Trans. Plasma Sci. **30**, 1931 (2002).

21. M. Carmo Lanca, J. N. Marat-Mendes, and L. A. Dissado, IEEE Trans. Dielectr. and Electr. Insulation **8**, 838 (2001).

22. E. O. Forster, IEEE Trans. on Electrical Insulation **20**, 891 (1985).

23. R. E. Hebner, J. Phys. D: Appl.Phys. **35**, 205 (2002).

24. P E Frayssines, N Bonifaci, A Denat and O Lesaint, J.Phys. D: Appl. Phys. **35**, 369 (2002).

25. L. Niemeyer, L. Pietronero, and H. J. Wiesmann, Phys. Rev. Lett. **52**, 1033 (1984).

26. P. P. Wong and E. O. Forster, IEEE Trans. on Electrical Insulation **EI-17**, 203 (1982).

27. I. V. Lisitsyn, H. Nomiyama, S. Katsuki, and H. Akiyama, IEEE Trans. Dielectr. Electr.Insula. **6**, 351 (1999).

28. M. Szklarczyk, "Electrical Breakdown of Liquids," *Modern Aspects of Electrochemistry,* Editors: J. O'M Bockris, B. E. Conway, and R. E. White (Plenum Press, New York, 1993), Vol. **25**, pp. 253-296.

29. J. Kolb, S. Kono, S. Xiao, B. Goan, XP. Lu, C. Bickes, M. Laroussi, R.P. Joshi, K.H. Schoenbach, and E. Schamiloglu, *14th IEEE International Pulsed Power Conference, Dallas, 2003.* Digest of Technical Papers. PPC-2003, **1**, 715 (2003).

30. J. K. Bragg, A. H. Sharbaugh and R. W. Crowe, J. Appl. Phys. **25**, 382 (1954).

31. A. H. Sharbaugh, J. C. Devins and S. J. Rzad, IEEE Trans. Electr. Insulation, **3**, 249 (1978).

32. V. D. Tarasov, V. A. Balakin and 0. P. Pecherskii, Sov. Phys.-Tech. Phys., **8,** 1379 (1972)

33. J. M. Lehr, J. E. Maenchen, J. R. Woodworth, W. A. Johnson, R. S. Coats, L. K. Warne, L. P. Mix, D. L. Johnson, I. D. Smith, J. P. Corley, S. A. Drennan, K. C. Hodge, D. W. Guthrie, M. J. Navarro, and G. S. Sarkisov, *Proc. of the 13th IEEE Pulsed Power Conf.*, pp. 609-614 (2002).

34. M. Butcher, A. Neuber, H. Krompholz, and J. Dickens, *Proc. of the 14th IEEE Pulsed Power Conf.*, pp. 1029-1032 (2003).

35. J. R. Woodworth, J. Lehr, J. Elizondo-Decanini, P. A. Miller, P. Wakeland, M. Kincy, J. Garde, B. Aragon, W. Fowler, G. Mowrer, J. E. Maenchen, G. S. Sarkisov, J. Corley, K. Hodge, S. Drennan, D. Guthrie, M. Navarro, D. L.

Johnson, H. C. Ives, M. J. Slattery, and D. A. Muirhead, IEEE Trans. Plasma Science **32**, 1778 (2004).

36. J. Qian, R. P. Joshi, J. Kolb, K. H. Schoenbach, J. Dickens, A. Neuber, M. Butcher, M. Cevallos, H. Krompholz, E. Schamiloglu and J. Gaudet, "Micro-Bubble Based Model Analysis of Liquid Breakdown Initiation By a Sub-Microsecond Pulse," accepted for publication, to appear J. Appl. Phys., July 2005.

37. T. J. Gallagher, *Simple dielectric liquid: mobility, conduction and breakdown*, (Oxford University Press, Oxford, 1975).

38. A. Beroual, J. Appl. Phys. **73**, 4528 (1993).

39. S E. Derenzo, T. S. Mast, H. Zaklad, and R. A. Muller, Phys. Rev. A **9**, 2582 (1974).

40. Sakai K. Sukegawa, S. Nakamura, and H. Tagashira, IEEE Trans. Electron. Ins. **23**, 609 (1988).

41. H. M. Jones and E. E. Kunhardt, Phys. Rev. B **48**, 9382 (1993).

42. K. C. Kao and J. P. C. McMath, IEEE Trans. Electron. Ins. **5**, 64 (1970).

43. P. K. Watson, IEEE Trans. Electron. Ins. **20**, 395 (1985).

44. Z. Krasucki, Proc. R. Soc. London, Ser. A **294**, 393 (1966).

45. H.M. Jones and E. E. Kunhardt, *12th International Conference on Conduction and Breakdown in Dielectric Liquids*, Roma, Italy, 360 (1996).

46. T. S. Light and S. L. Licht, Analytical Chemistry **59**, 2327 (1987).

47. J. R. Macdonald and S. H. Liu, Surf. Science **125** 653 (1983)

48. C. Champion, Phys. Med. Biol. **48**, 2147 (2003).

49. For example, C. Jacoboni and P. Lugli, *The Monte Carlo Method for Semiconductor Device Simulation* (Wein Publishers, New York, 1989).

50. For example, C. K. Birdsall and A. B. Langdon, *Plasma Physics via Computer Simulation* (McGraw Hill, New York, 1985).

51. W. F. Schmidt, *Liquid State Electronics of Insulating Liquids* (CRC Press, Boca Raton, 1997).

52. P. Teulet, J. P. Sarrette and A. M. Gomes, J. Quantitative Spectroscopy **62**, 549 (1999).

53. A. V. Phelps, *Joint Institute for Laboratory Astrophysics Information Center Report No. 28* (University of Colorado Press, Boulder, 1985).

54. J. S. Morrill, W. M. Benesch, K. G. Widing, J. Chem. Phys. **94**, 262 (1991).

55. G. Gouy, J. Phys. (Paris) **9**, 457 (1910).

56. D. L. Chapman, Philos. Mag. **25**, 475 (1913).

57. G. M. Torrie and J. P. Valleau, J. Chem. Phys. **73**, 5807 (1980).

58. D. M. Heyes, Chem. Phys. **69**, 155 (1982).

59. S. H. Suh, L. M. Teran, H. S. White, and H. T. Davis, Chem. Phys. **142**, 203 (1990).

60. R. Guidelli, G. Aloisi, M. Carlá, and M. R. Moncelli, J.Electroanalytical Chemistry **197**, 143 (1986).

61. L. Zhang, H. T. Davis, and H. S. White, J.Chem. Phys. **98**, 5793 (1993).

62. H. J. C. Berendsen, J. R. Grigera, and T. P. Straatsma, J. Phys. Chem. **91**, 6269 (1987).

63. D. E. Smith and L. X. Dang, J. Chem. Phys. **100**, 3757 (1994).

64. S. H. Lee, J. Chem. Phys. **101**, 6964 (1994).

65. E. Spohr, Journal of Molecular Liquids **64**, 91 (1995).

66. P. G. Kusalik and I. M. Svishchev, Science **265,** 1219 (1994).

67. P. S. Crozier and R. L. Rowley, Journal of Chem. Phys., **114**, 7513 (2001).

68. Y. J. Rhee, J. W. Halley, J. Hautman, and A. Rahman, Phys. Rev. B **40**, 36 (1989).

69. D. Boda, K. Y. Chan, and D. Henderson, J. Chem. Phys. **109**, 7362 (1998).

70. M. Neuann, Chem. Phys. Letter **95**, 417 (1983).

71. J. Anderson, J. Ullo and S. Yip, Chem. Phys. Letter **152**, 447 (1988).

72. A. K. Soper, Chem. Phys. **258**, 121 (2000).

73. G. Hura, J. M. Sorenson, R. M. Glaeser, and T. Head-Gordon, J. Chem. Phys. **113**, 9140 (2000) ; J. M. Sorenson, G. Hura, R. M. Glaeser, and T. Head-Gordon, J. Chem. Phys. **113**, 9149 (2000).

74. I. Danielewicz-Ferchmin and A. R. Ferchmin, Chem. Phys. Lett. **351**, 397 (2002).

75. S. R. Broadbent and J. M. Hammersley, Proc. Camb. Phil. Soc., **53**, 629 (1957).

76. J. H. Stathis, J. Appl. Phys., **86**, 5757 (1999).

77. R. Degraeve, G. Groeseneken, R. Bellens, J. L. Ogier, M. Depas, P. J. Roussl, and H. E. Maes, IEEE Tran. Electr. Dev., **57**, 904 (1998).

78. M. Sahimi and J. D. Goddard, Phys. Rev. B, **33**, 7848 (1986).

79. C. Pennetta, L. Reggiani, and G. Trefan, IEEE Trans. Electr. Dev., **47**, 1986 (2000).

80. B. I. Shklovskii and A. L. Efros, *Electronic Properties of Doped Semiconductors*, (Springer-Verlag, Berlin, 1984).

81. W. J. Boudville and T. C. McGill, Physical Review B, **39**, 369 (1989).

82. G. Wu, S. Asai, C. Zhang, and T. Miura, and M. Sumita, J. Appl. Phys., **88**, 1480 (2000).

83. A. H. Sharbaugh and P. K. Watson, *Progress in Dielectrics*, Wiley, New York, 1982, Vol. **4**, pp.199-248.

84. R. Laenen, T. Roth, and A. Laubereau, Phys. Rev. Lett. **85**, 50 (2000).

85. N. F. Bunkin and F. V. Bunkin, Sov. Phys. JETP **74**, 271 (1992).

86. M. Arrayas, Am. J. Phys. **72**, 1283 (2004) ; M. Arrayas, U. Ebert, and W. Hundsdorfer, Phys. Rev. Lett. **88**, 174502 (2002).

87. G. Massala and O. Lesaint, J. Phys. D: Appl. Phys. **34**, 1525 (2001).

88. J. P. Boris and D. L. Book, J. Comput. Phys. **11**, 38 (1973).

89. D. L. Book, J. P. Boris and K. Hain, J. Comput. Phys. **18**, 248 (1975).

90. J. P. Boris and D. L. Book, J. Comput. Phys. **20**, 397 (1976).

91. S. T. Zalesak, J. Comput. Phys. **31**, 335 (1979).

92. J. Wu and E. E. Kunhardt, Phys. Rev. A **37**, 4396 (1988).

93. Morrow, IEEE Trans. Plasma Science **19**, 86 (1991).

94. S. K. Dhali and P. F. Williams, J. Phys. D **62**, 4696 (1987).

95. P. A. Vitello, B. M. Penetrante, and J. N. Bardsley, Phys. Rev. E **49**, 5574 (1994).

96. P. D. Lax and B. Wendroff, Comm. Pure Appl. Math **13**, 217 (1960).

97. K. W. Morton, Proc. Roy. Soc. (London) A **323**, 237 (1971).

98. L. B. Loeb, Science **148**, 1417 (1965).

99. R. G. Fowler, Adv. Electron. And Electron Phys. **41**, 1 (1976).

100. J. C. Devins, S. J. Rzad, and R. J. Schwabe, J. Appl. Phys. **52**, 4531 (1981).

101. C. Zener, Proc. Roy. Soc. **145**, 523 (1934).

102. C. J. Rothfuss, V. K. Medvedev, and E. M. Stuve, Surf. Sci. **501**, 169 (2002) ; C. J. Rothfuss, V. K. Medvedev, and E. M. Stuve, J. Electroanalytical Chem. **554-555**, 133 (2003).

103. J. P. Hernandez, Rev. Mod. Phys **63**, 675 (1991).

104. Y. Sakai, W. F. Schmidt, and A. G. Khrapak, IEEE Trans. Dielectr. Electr. Insul. **1**, 724 (1994).

105. W. Lin, Journal of Electrostatics **36**, 129 (1995).

106. For example, E. Merzbacher, *Quantum Mechanics* (John Wiley, New York, 1970).

107. R. P. Joshi, J. Qian, G. Zhao, J. Kolb, K. H. Schoenbach, J. Gaudet and E. Schamiloglu, J. Appl. Phys. 96, 5129 (2004).

108. B. Mandelbrot, *Fractals: Forms, Chance and Dimension*, (Freeman, San Francisco, 1977); B. Mandelbrot, *The Fractal Geometry of Nature*, (Freeman, San Francisco, 1982).

109. H. Takayasu, Phys. Rev. Letter **54**, 1099 (1985).

110. D. Stauffer, Phys. Reports **54**, 1 (1979).

111. D. B. Fenneman and R. J. Gripshover, IEEE Trans. Plasma Science **PS-8**, 209 (1980).

112. A. Beroual, M. Zahn, A. Badent, K. Kist, A.J. Schwabe, H. Yamashita, K. Yamazawa, M. Danikas, W.G. Chadband, and Y. Torshin, IEEE Electrical Insulation Magazine **14**, 7 (1998).

VITA

for

Jun Qian

EDUCATION

Ph. D. Electrical Engineering, Old Dominion University, Norfolk, VA
M. S. Automatic Control Engineering, University of Science & Technology of China, China
B. S. Material Engineering, Northeastern University, China

PAPERS PUBLISHED

J. Qian, R. P. Joshi, J. Kolb, K. H. Schoenbach, J. Dickens, A. Neuber, M. Butcher, M. Cevallos, H. Krompholz, E. Schamiloglu and J. Gaudet, "Micro-Bubble Based Model Analysis of Liquid Breakdown Initiation By a Sub-Microsecond Pulse". accepted for publication, to appear *J. Appl. Phys.*, July 2005.

J. Qian, R. P. Joshi, J. Kolb, and K. H. Schoenbach, J. Dickens, A. Neuber, M. Butcher, M. Cevallos, and H. Krompholz, E. Schamiloglu and J. Gaudet, "Simulation Studies of Liquid Water Breakdown By a Sub-Microsecond Pulse". *15th IEEE International Pulsed Power Conference*, Monterey, CA, June 2005.

R. P. Joshi, J. Qian, G. Zhao, J. Kolb, K. H. Schoenbach, J. Gaudet and E. Schamiloglu, "Are micro-bubbles necessary for the breakdown of liquid water subjected to a sub-microsecond pulse?" *J. Appl. Phys.*, Vol. 96, No. 9, pp. 5129-5139, 2004.

R. P. Joshi, J. Qian, and etc., "Microscopic analysis for water stressed by high electric fields in the pre-breakdown regime" *J. Appl. Phys.*, Vol. 96, No. 7, pp. 3617-3625, 2004.

R. P. Joshi, J. Qian, S. Katsuki, K.H. Schoenbach, "Electrical conduction in water revisited: role of field-enhanced dissociation and a reaction-based boundary condition", *IEEE Trans. on Electrical Insulation*, Vol. 10, No. 2, April 2003.

R. P. Joshi, Jun Qian, and K. H. Schoenbach, "Electrical network-based time-dependent model of electrical breakdown in water", *J. Appl. Phys.*, Vol. 92, No. 10, pp. 6245-6251, 2002.

Jun Qian, R. P. Joshi, K. H. Schoenbach, E. Schamiloglu, and C. Christodoulou, "Percolative model of electric breakdown in liquid dielectrics", *IEEE Trans. on Plasma Science*, Vol. 30, No. 5, pp.1931-1938, Oct. 2002.

R. P. Joshi, Jun Qian, J. Kolb and K. H. Schoenbach, "Model analysis of breakdown in high-voltage, water-based switches", *IEEE 14th Power Pulse Conference*, Dallas, TX, June 2003.